Comparative Gibbsian composite-system thermodynamics for confined and unconfined multicomponent multiphase systems

by:

Leila Zargarzadeh

A thesis submitted in partial fulfillment of the requirements for the degree of

Doctor of Philosophy
in
CHEMICAL ENGINEERING

Department of Chemical and Materials Engineering
University of Alberta

Abstract

The behavior of multiphase multicomponent systems can be well predicted by Gibbsian composite-system thermodynamics. This approach is used in this thesis to study three different systems of interest: (i) nanobubbles on a flat solid surface submerged in a liquid solution at constant temperature and liquid pressure, (ii) bubble formation, starting with a convex or a concave meniscus inside a finite cone exposed to a liquid solution at constant temperature and liquid pressure, and (iii) comparison of the polynomial equations for the osmotic virial equation and the Margules model, and their application in fitting to solid–liquid equilibrium data of different water/solute mixtures with a eutectic point.

(i) A surface nanobubble has the shape of a spherical cap with a height of tens of nanometers and an anomalously high contact angle (measured through the liquid phase). The conditions for the stability of surface nanobubbles submerged in a liquid solution at constant temperature and liquid pressure are investigated by finding the conditions for equilibrium and the appropriate free energy of the system. It is assumed that on the time scale of the experiment, the bubbles are not in diffusive contact with each other or the gas phase outside the system. The changes in the concentration of the liquid phase and the surface nanobubble as it grows are both taken into account. From this investigation it is concluded that surface nanobubbles can only be

stable if the liquid solution is initially supersaturated, and the contact angle is anomalously high.

(ii) For a bubble starting inside a cone, with a convex or a concave meniscus (depending on the contact angle and cone apex angle), from a liquid solution at constant temperature and pressure, stability analysis has been performed by finding the conditions for equilibrium and the appropriate free energy of the system. The bubble is studied over the whole growth path: inside, pinned to the corner, and outside the finite cone. The changes in the concentration of the bulk liquid phase and the gas phase are considered as the bubble grows. For a bubble starting with a convex meniscus, a stable bubble can only form after passing an energy barrier and if the initial liquid is above a certain degree of saturation (which depends on other parameters of the system). In cases where the height of the energy barrier becomes comparable to the depth of the energy well of the stable point, and if the energy barrier is sufficiently small, bubble "formation–disappearance fluctuation" occurs. For a bubble starting with a concave meniscus, there is always at least one stable equilibrium state, even when the liquid phase is pure, and there is no initial energy barrier to be overcome. In each of the cases, the stable equilibrium may form inside, pinned, or outside the cone depending on the parameters of the system. The effect of different parameters including cone apex angle, cone half mouth radius, contact angle, total number of moles, and the initial degree of saturation, on the stability of a bubble inside a cone are investigated to present a comparative complete picture of the phenomena.

(iii) The polynomial forms of the osmotic virial equation and the Margules model are compared for two-component solutions. Fitting each model to the solid–liquid equilibrium experimental data of different water/solute systems with a eutectic point shows that both models perform well in fitting the data. Fitting is done over both the ice-formation and the solute-precipitation regions. In the osmotic virial equation, the integration constant in expressing the concentration effect of the solute (that arises from the Gibbs–Duhem equation) is shown to be dependent on the osmotic viral coefficients and the relation for that is derived.

The comparative approach in this study provides a big picture for each of the systems that promotes better understating, hence an ability for future design or control, of the phenomena.

Preface

Chapter 2 of this thesis has been published, with minor modifications, as: Zargarzadeh, L.; Elliott, J. A. W. Thermodynamics of Surface Nanobubbles. *Langmuir* **2016**, *32* (43). DOI: 10.1021/acs.langmuir.6b01561. In that paper, the explanation for the anomalously high contact angle of surface nanobubbles was proposed by Dr. Elliott. The rest of the paper is the origional work by me, with Dr. Elliott contributing as a supervisory author.

Chapter 3 of this thesis and Appendices A-1, A-2, and A-3 have been submitted for publication as: Zargarzadeh, L.; Elliott, J. A. W. Bubble Formation in a Finite Cone: More Pieces to the Puzzle.

Chapter 4 of this thesis has been submitted for publication as: Zargarzadeh, L.; Elliott, J. A. W. Comparison of the Osmotic Virial Equation with the Margules Activity Model and their Application to Solid–Liquid Equilibrium. Part of Chapter 4 has been published as part of Liu, F.; Zargarzadeh, L.; Chung, H.-J.; Elliott, J. A. W. Thermodynamic Investigation of the Effect of Interface Curvature on Solid–Liquid Equilibrium and Eutectic Point of Binary Mixtures. *J. Phys. Chem. B* **2017**, *121* (40), 9452–9462. DOI: 10.1021/acs.jpcb.7b07271. In the published paper, my role was fitting the Margules model to the experimental data for the water/glycerol system, and contributing to the manuscript composition and editing.

به جهان خرّم از آنم که جهان خرّم از اوست

عاشقم بر همه عالم که همه عالم از اوست

"In the world I am blissful, as the world is blessed with God's essence

I am in love with the entire universe, as it is filled with God's presence"

Saadi

To my parents

and

in loving memory of my grandmothers,

Iran Landi and Batoul Shamshiri

Acknowledgements

I would like to express my sincere appreciation to my supervisor, Dr. Janet A. W. Elliott for her insightful discussions, valuable guidance, and support of my research and professional development. I would also like to thank the supervisory committee, Dr. John Shaw and Dr. Tony Yeung, for their valuable discussions and comments.

I would like to express my gratitude to Fatemeh Eslami, Nadia Shardt, and Monir Hosseini Anvari for their inspiring scientific discussions, sharing the literature, and above all for being great friends.

I am much indebted to all the teachers and mentors throughout my life. I am especially appreciative of Dr. Sona Raeisi, Dr. Nasir Mehranbod, Dr. Shahab Ayatollahi, and Dr. Gholamreza Karimi.

My heartfelt appreciation goes to my aunt, Zahra Neshatdoust, and my uncle, Ali Ghasemi, for their support throughout the past 2.5 years in Edmonton. Also the help from Ali Ghasemi in drawing Figures Figure 8 and Figure 9 with AutoCAD is appreciated.

I am grateful to all of my Iranian friends in Edmonton for their support. I would particularly like to thank Sabereh Rezaei, Maedeh Roodpeyma, Behzad Vafaeian, Hoda Sepehri Rad, and Majid Raghami. I am also deeply grateful to my friends, Nazanin Zarei, Afrooz Ebadat, and Marzieh Shokrollahi for their support, despite being far away.

Words fail to express my deepest gratitude to my beloved parents, Shahine Neshatdoust and Ahmad Zargarzadeh, and my dear siblings, Amin, and Maryam, for their love, constant support, and encouragement.

I gratefully acknowledge the funding from the Natural Sciences and Engineering Research Council (NSERC) of Canada, Alberta Innovates–Technology Future (AITF), and the Government of Alberta.

Leila Zargarzadeh

November 2018

Table of Contents

List of Tables

List of Figures

1. Introduction

Fundamental understanding of multiphase systems improves prediction, design, or optimization of natural systems or industrial processes in chemical, pharmaceutical, food, and many other industries. In this thesis the behavior of certain multiphase multicomponent systems at equilibrium is studied using Gibbsian composite-system thermodynamics.[1] The systems of interest presented in this study are: (i) nanobubbles on flat solid surfaces submerged in a liquid solution in Chapter 2, (ii) bubble formation inside a finite cone submerged in a liquid solution in Chapter 3, and (iii) the comparison of two models for the effect of concentration on the chemical potential of the liquid phase: the osmotic virial equation and the Margules model, and their performance in fitting to data for solid–liquid equilibrium across a flat interface, in Chapter 4.

The approach is to obtain equations for the conditions for equilibrium from the fundamental postulate stating that changes in the entropy of the system plus reservoir are zero for a system at equilibrium. For systems with highly curved interfaces and micro- or nano-scale systems, the involved interfaces must also be considered in the entropy of the composite-system to account for surface effects. In this thesis surface effects are significant and considered in the systems of Chapters 2 and 3. Some examples of the conditions for equilibrium (depending on the system) are: the well-known Young–Laplace equation defining the pressure difference across a curved interface, the Young equation that dictates the contact angle of a curved fluid–fluid interface on a solid surface, and the equality of chemical potential of a component between two phases. Next, the equations for the conditions for equilibrium are combined with equations that represent the effect of concentration on the chemical potentials, such as equations of state for components in vapor or liquid phase, or

activity models for components in the liquid phase. Rearrangement of the equilibrium equations, along with equations for the chemical potentials, leads to valuable equations for describing the behavior of the system. This approach results in the equation for equilibrium radius of the liquid–vapor interface (also called the Kelvin radius) for the case of the solid–liquid–vapor systems with curved liquid–vapor interfaces in Chapters 2 and 3, or equations describing the phase diagram (temperature versus concentration) of solid–liquid systems with flat interfaces and with a eutectic point in Chapter 4.

In Chapter 2 of this thesis, the stability of interfacial nanobubbles on hydrophobic solid surfaces submerged in liquid, at constant temperature and liquid pressure, is investigated using Gibbsian composite-system thermodynamics. Surface nanobubbles are spherical caps with a height up to tens of nanometres, and an anomalously high contact angle (measured through the liquid phase).[2] Surface nanobubbles have been proposed to play a role in interactions of hydrophobic surfaces submerged in aqueous solutions[3] and thin film rupture.[4,5] Some potential applications of surface nanobubbles are separation of fine particles by air bubble floatation,[6,7] manipulation of adsorption on hydrophobic surfaces,[8,9] drag reduction in microfluidic devices by increasing wall slip,[10,11] and as soft nanotemplates,[12,13] among other proposed applications summarized in recent review papers.[2,14–16] Gibbsian composite-system thermodynamics can contribute to understanding the conditions for stability of surface nanobubbles. Previous thermodynamic studies investigated homogenous nucleation of bubbles from bulk liquid,[17,18] pure surface bubbles[19,20] (an idealized assumption in the case of very low solute gas solubility or gas diffusion into the surrounding bulk liquid), and stability of bubbles in a hydrophilic conical solid submerged in a liquid–gas solution.[21] The present thermodynamic study investigates the stability of nanobubbles on a flat surface, considering both the solute gas and the solvent being present in each of the liquid and vapor phases, with the concentration changing as the size of the bubble changes over the range for stability analysis. The size of the equilibrium radius and nature of the equilibrium state (unstable, stable, or metastable) of surface nanobubbles are determined from two methods (available in literature[21]): the

intersection of the equilibrium radius and the geometry radius, and also by finding the extrema in the free energy curve as a function of size of the system. The results from both methods are reaffirming. We also investigated the effect of different parameters on the size and stability of the equilibrium states. Parameters include: the type of dissolved gas, the total number of moles per bubble in the system (analogous to the total number of bubbles in a system with certain number of moles), the degree of saturation, and the equilibrium contact angle.

Chapter 3 of this thesis presents an investigation of the stability of a bubble, starting with a convex or a concave meniscus, inside a finite cone exposed to a liquid solution, at constant temperature and liquid pressure, with multiphase Gibbsian composite-system thermodynamics. The stability analysis is done over the whole growth path of the bubble: inside, pinned to the corner, or outside the cone. This study has significance in designing superhydrophobic surfaces with applications in drag reduction[22,23] and nucleation sites to stimulate boiling heat transfer.[24,25] Furthermore, stable bubbles on the rough surface have a role in manipulation of adsorption on solid surfaces, reduction of biofouling,[26,27] and adhesion of blood platelets to the roughness of synthetic biomaterials,[28] among many other applications.[2] The few current thermodynamic studies of the phenomena are restricted to limited cases only. Ward *et al.*[21,29] showed that for a bubble starting with a convex meniscus in a cone exposed to a liquid solution, a stable bubble forms when the bubble gets pinned to the corner of the cone. However, they did not investigate the effect of different parameters such as cone angle, cone width, or contact angle. Some other works focus on the cases where a bubble starts with a concave meniscus inside a cone;[24,30–33] although they did not fully investigate the stability of the bubble as it gets pinned to the corner and grows outside the cone, nor did their study include a full investigation of the effects of different parameters. In this thesis, we present a full study of the phenomena, for both cases of the bubble starting with a convex or a concave meniscus inside a finite cone exposed to a liquid solution. The status of the system is investigated over the whole growth path: inside, pinned, and outside the cone. The size and nature (unstable, metastable, or stable) of the equilibrium states are determined

from two methods: the intersection of the Kelvin radius and the geometry radius, and the extrema in plots of free energy versus size of the bubble. It is tested whether the stable bubble is always pinned to the corners of the cone. The effect of cone apex angle, cone mouth radius, contact angle, total number of moles, and initial degree of saturation on the number and nature of equilibrium states are all investigated.

In Chapter 4, two models for expressing the concentration dependence of chemical potential of a component in a two-component liquid solution are compared: the general polynomial form of the osmotic virial equation and the Margules model for the liquid activity coefficients. Each of the osmotic virial equation (truncated to the first or second virial coefficient) and the Margules model is fitted to experimental data of phase equilibrium in order to empirically obtain the coefficients/parameters of the model. In this study solid–liquid equilibrium data for water/solute systems is chosen as the phase equilibrium data. Relevant equations for the phase diagram (temperature *vs.* composition) of solid–liquid equilibrium with a flat interface and the curve fitting procedure are explained in this Chapter. The osmotic virial equation (OVE) is widely used to model nonideal behavior of biological solutions, with parameters obtained by fitting to experimental equilibrium data. In the cryobiology literature, solid–liquid equilibrium data for binary aqueous solutions in equilibrium with ice have been fitted with the osmotic virial equation by Elliott and co-workers.[34–36] The coefficients obtained by Elliott and co-workers[34–36] are only accurate for the solid ice–liquid solution equilibrium region, as the fitting was based on the limited data of the ice-formation region. In this study, the fitting of the osmotic viral equation was done to binary solid–liquid equilibrium data over the entire range of composition, including both the ice-formation and the solute-precipitation regions. The results are compared with the result of fitting of Margules model, which has a similar polynomial form.

It should be noted that in Chapters 2 and 3, γ represents the surface tension, while in Chapter 4, γ_i represents the activity coefficient of component i. The symbol R represents the

universal gas constant in Chapters 2 and 4, whereas it represents the size of the radius in Chapter 3. The universal gas constant is denoted by R_U in Chapter 3.

The highlights of this research are:

1) A comparative study is conducted throughout the research. In Chapters 2 and 3, the effects of different parameters (geometry parameters, contact angle, concentration, and total number of moles) on the stability of each system are investigated. In Chapter 4, two models for the effect of concentration on chemical potential in the liquid phase are compared: the empirical Margules model versus the osmotic virial equation. Such a comparative study leads to a big picture understating of the phenomena. In the case of a bubble on a flat solid surface or inside a cone, for example, having the big picture of effects of different parameters will enable optimal design in applications or control of the phase transition.
2) Unlike many studies available in literature that consider pure fluid phases for simplifications, here we consider multicomponent multiphase systems for better representation of real cases.

2. Thermodynamics of Surface Nanobubbles

2.1. Chapter summary

In this study, we examine the thermodynamic stability of surface nanobubbles. The appropriate free energy is defined for the system of nanobubbles on a solid surface submerged in a supersaturated liquid solution at constant pressure and temperature, under conditions where an individual nanobubble is not in diffusive contact with a gas phase outside of the system or with other nanobubbles on the timescale of the experiment. The conditions under which plots of free energy versus the radius of curvature of the nanobubbles show a global minimum, which denotes the stable equilibrium state, are explored. Our investigation shows that supersaturation and an anomalously high contact angle (measured through the liquid) are required to have stable surface nanobubbles. In addition, the anomalously high contact angle of surface nanobubbles is discussed from the standpoint of a framework recently proposed by Koch, Amirfazli, and Elliott that relates advancing and receding contact angles to thermodynamic equilibrium contact angles, combined with the existence of a gas enrichment layer.

2.2. Introduction

Surface nanobubbles (also called interfacial nanobubbles) are nanoscopic gaseous domains on solid–liquid interfaces.[2] The typical shape of surface nanobubbles is a spherical cap with a height of up to tens of nanometers, a lateral diameter ranging from hundreds of nanometers to several micrometers, and an anomalously high contact angle (measured through the liquid) compared with that of macroscopic droplets.[2] For example, on highly oriented pyrolytic graphite (HOPG) with advancing/receding macroscopic contact angles of 95/65°, the

contact angle of nanobubbles formed by the solvent exchange method is reported to be in the range of 160–175°.[37,38] On mica with an advancing/receding macroscopic contact angle of 5/0°, the nanobubble contact angle is in the range of 120–150°.[37] Another example is nanobubbles with a contact angle between 150 and 170° on silicone coated with octadecyltrimethylchlorosilane (OTS), whereas the advancing/receding macroscopic contact angle is 110/100°.[38] Several other examples of nanobubble sizes and contact angles are reported in the review article by Lohse and Zhang.[2]

Surface nanobubbles are stable for days in experiments.[2] Such long-term stability is considered controversial and contradictory to the theoretical results of Ljunggren and Eriksson[39] that showed short lifetimes (between 1 and 100 μs) for single small bubbles (with radii between 10 and 100 nm) in the bulk. A similar method was first developed by Epstein and Plesset[40] for macrobubbles and is based on the combination of the diffusion equation, the Young–Laplace equation, and Henry's law. What Ljunggren and Eriksson[39] did not consider is that surface nanobubbles can have nanometer height yet micrometer radius of curvature. The anomalously high contact angle (measured through the liquid) means that the surface bubble is flattened to nanometer height. In fact the term nanometer refers to the nanoscale height of the bubble, whereas the diameter of the bubble is on the order of micrometers.[41]

Surface nanobubbles were first hypothesized by Parker *et al.*[42] in 1994 (based on stepwise features in atomic force curves between hydrophobic surfaces in aqueous solutions) to explain long-range attraction between hydrophobic surfaces. The first direct experimental evidence for surface nanobubbles was reported in 2000, from tapping mode atomic force microscopy (AFM) images by Ishida *et al.*[43] and Lou *et al.*[37] Despite initial doubts that considered the observations to be an artifact of AFM or contamination, later experimental methods, such as optical microscopy and spectroscopy, confirmed the existence and gaseous nature of surface nanobubbles.[44]

There is an emerging interest in the field of nanobubbles because of their potential applications. The existence of surface nanobubbles was proposed as a reason for some surface phenomena such as the increase in attractive interactions between hydrophobic surfaces[3] and thin liquid film rupture.[4,5] Moreover, surface nanobubbles may potentially be used for separation of fine particles by air bubble flotation,[6,7] in manipulation of adsorption on hydrophobic surfaces,[8,9] for enhancement of wall slip to achieve drag reduction in microfluidic devices,[10,11] and as soft nanotemplates for the production of hollow nanomaterials,[12,13] among other proposed applications summarized in recent review papers.[2,14–16]

Among various methods for inducing surface nanobubbles summarized by Lohse and Zhang,[2] the most commonly used protocol is the solvent exchange process (commonly alcohol–water exchange). In this method, an alcohol that is saturated (or even supersaturated) with air or a specific gas is replaced by water, which is an inferior solvent. As a result, a local transient gas supersaturation is created.[2] Until now nanobubbles could only be produced on hydrophobic surfaces. The only exception is nanobubble formation on mica which, according to Lohse and Zhang,[2] can be due to the crystalline structure of mica, ion dissociation from the surface, or unavoidable airborne adsorbents. The surface nanobubble nucleation mechanism is considered to be due to supersaturation.[45] The supersaturation is attributed to (a) lower solubility of air in water than that in the initial solvent and (b) the decrease in solubility because of the temperature increase by exothermic mixing of water and the initial solvent.[16] The necessity of supersaturation for surface nanobubble nucleation has been denied by Seddon *et al.,*[46] who criticized that "most, if not all," alcohol–water exchange experiments use unsaturated water to replace alcohol.[46] However, as discussed by Weijs *et al.*,[47] local supersaturation can exist that is not reflected in the global concentration in the bulk liquid.

Different theories have been proposed to explain the observed stability of nanobubbles and their high contact angle (measured through the liquid):

(i) Line tension: It was proposed that the anomalously high contact angle of nanobubbles can be explained by the effect of line tension,[48–50] which is related to the excess energy of the three-phase contact line. By including line tension, the contact angle becomes size dependent according to the modified Young equation. However, the theoretical values of line tension are too small (by one to two orders of magnitude) to change the contact angle of bubbles with contact lines of the size of surface nanobubbles.[2] Also, even if higher values for line tension are used, the existence of a positive line tension would decrease the contact angle (as measured through the liquid) from that of a macrobubble rather than increase the contact angle as is observed in surface nanobubble experiments.[2,51] Furthermore, trends of the nanobubble contact angle with nanobubble size are not consistent with explanation by the Young equation modified by line tension.[2,51] Therefore, line tension cannot explain the elevated contact angle of nanobubbles.[2,51]

(ii) Dynamic equilibrium theory: Brenner and Lohse[52] postulated that there was a balance between diffusive gaseous outflux and a continuous gas influx near the contact line, because the hydrophobic surface attracts gas molecules more than water. Their theory predicts the radius of the metastable bubble and the threshold of nanobubble formation as a function of gas concentration and hydrophobicity.[52] However, there is still a lack of explanation of the driving mechanism.[2]

(iii) Contamination layer: Ducker[53] suggested that there is a film of contamination at the gas–liquid interface that leads to bubble stabilization by hindering gas diffusion from the bubble, and also increases the contact angle (measured through the liquid) by decreasing the liquid–gas surface tension. Das *et al.*[54] showed theoretically that the effect of the ionic or nonionic contamination on lowering surface tension can explain the high contact angle but is not sufficient to explain the long term stability of nanobubbles. In their modeling, Das *et al.*[54] did not consider the blockage effect of the contamination. Later, Zhang *et al.*[55] provided experimental evidence against Ducker's contamination theory,[53] showing that nanobubbles

remained stable even after using various surfactants (cationic, anionic, and nonionic) to wash away potential materials adsorbed at the gas–liquid interface. Moreover, the gas–liquid interface was found to be gas permeable in experiments by German *et al.*[56] contrary to Ducker's[53] claim.

(iv) Three-phase contact line pinning: Several groups considered roughness and/or chemical heterogeneity as the cause of high contact angle.[49,57] According to Liu and Zhang,[58] heterogeneity can result in contact line pinning that is crucial for the stabilization of surface nanobubbles, along with supersaturation. Lohse and Zhang[59] demonstrated that a pinned single surface nanobubble can be stable in a supersaturated liquid solution when the pinning site is small enough. Their modeling is based on a combination of the diffusion equation, the Laplace pressure, and Henry's equation. Their theory predicts the equilibrium contact angle as a function of the size of the pinning site and the equilibrium radius of curvature. Also, their calculations show that the equilibrium radius of curvature is constant at a given supersaturation.

(v) Interfacial gas enrichment theory: Experiments of van Limbeek and Seddon[60] showed that the contact angle of nanobubbles on hydrophobic surfaces is more significantly affected by the gas type compared to the solid type, so they proposed that nanobubbles sit on top of adsorbed gas molecules.[60] The presence of an interfacial gas layer can clarify the anomalous contact angle and the source of gas influx in the dynamic equilibrium theory[52] that explains the stability of nanobubbles.[47,60] Although experiments showed no gaseous layer in the absence of nanobubbles,[56] in the presence of nanobubbles, experiments provided evidence of an interfacial gas layer.[61–63] It remains a question why the gas layer is only present when nanobubbles are present, and why it does not affect the macroscopic contact angle.[51] From a theoretical point of view, molecular dynamics simulations[47,64,65] showed reduced density near the hydrophobic surface in water because of the accumulation of dissolved gas. Later Peng *et al.*[63,66] provided proof of the existence of a dense gas layer called interfacial gas enrichment

on hydrophobic interfaces in water by force curve analysis[63] and molecular simulations.[66] According to Peng *et al.*,[66] molecular simulations can explain the long life of nanobubbles through slow diffusion of high-density gas clusters into the bulk. Peng *et al.*[66] also showed high contact angles, close to the experimentally reported nanobubble contact angle of 150° (measured through the liquid side), for cylindrical gas domains on graphite–water interfaces by two methods, finding an angle of ~141° by fitting a cylindrical shape to the simulated position of the interface and an angle of 145° by substituting interfacial tensions calculated by Monte Carlo simulations into the Young equation.

Several groups attempted to prove the stability of surface nanobubbles by molecular dynamics simulations. Molecular dynamics simulations by Weijs *et al.*[67] indicated stable surface nanobubbles in a closed, finite system supersaturated with gas. For an open system, Liu and Zhang[58] showed stable surface nanobubbles in a supersaturated system, for a timescale of 200 ns, by including controlled surface heterogeneity into the earlier molecular dynamics simulation of open systems by Weijs *et al.*[47] Current molecular dynamics simulations are limited to small length scales and short time scales (at most tens of nanometers and sub-microseconds) with the currently available computational power, whereas surface nanobubbles are experimentally stable for hours or days and may have larger sizes.[2]

The goal of this study is to contribute to the understanding of the stability of surface nanobubbles from a thermodynamic point of view. There have been only a few articles using thermodynamic stability analysis to study nanobubbles. Wasai *et al.*[17] investigated homogeneous nucleation (*i.e.*, a bubble surrounded by a bulk liquid solution). By taking into account the changes in the free energy of the parent phase, Wasai *et al.*[17] showed that the nucleation curve (free energy change versus homogeneous nucleus size) has a minimum point, which indicates the theoretical possibility of stable nano-nuclei in equilibrium with a supersaturated parent phase. Later, Colaço *et al.*[19] used a thermodynamic approach to evaluate the stability of a pure vapor bubble trapped at a solid–liquid interface for surfaces with

different roughnesses and hydrophobicities. However, there were inaccuracies in their calculations,[68,69] and their model only considered the less realistic case of a pure bubble. Recently, Yarom and Marmur[20] showed thermodynamic stability of a bubble (at a surface or in the bulk) for the case of insoluble gas in water (an idealization of very low gas solubility and very low diffusion of gas in the surrounding liquid) at constant temperature and pressure. In contrast, the study presented in this work considers the stability of surface nanobubbles in a realistic case where both the solute gas and the solvent are present in the liquid and vapor phases.

Several years before Parker *et al.*'s[42] hypothesis of nanobubbles in 1994, there were two theoretical articles by Ward *et al.*[18,21] that showed the stability of bubbles with a micro-scale radius of curvature in two cases: bubbles in the bulk of a liquid–gas solution[18] and bubbles on a hydrophilic conical solid surface submerged in a finite-volume liquid–gas solution.[21] However, the contact angle was only involved in the later article for a hydrophilic conical surface (with a contact angle of 10°). Herein, we describe the appropriate free energy (similar to that used by Ward and Levart[21]) for the system of surface nanobubbles on a solid submerged in a liquid solution at constant pressure and temperature. We assume that a single nanobubble is diffusionally isolated from other nanobubbles and the free liquid surface on the time scale of the experiments. That is, we assume that the nucleation and stability of nanobubbles are dependent on the local supersaturation of a volume of liquid surrounding an individual nanobubble. Plots of free energy versus the radius of curvature of the nanobubble reveal the number of equilibrium states and their nature—stable, metastable, or unstable—corresponding to the global minimum, local minima, and maxima or inflection points, in the free energy, respectively.[70–75]

In the following sections, the system is defined and then the thermodynamic potential (free energy) is calculated and analyzed. For the stability analysis, we take the experimentally observed high contact angle of nanobubbles as known. Following the thermodynamic stability

analysis, we discuss possible reasons for the anomalously high contact angle of surface nanobubbles.

2.3. Thermodynamic stability analysis of nanobubbles

The system of interest consists of diffusionally isolated surface nanobubbles so that we can first consider a single nanobubble on a surface submerged in a liquid–gas solution, as shown in Figure 1. The constraints on the system are the following: the pressure P^R and temperature T^R of the reservoir surrounding the system are constant; the solid phase is considered to be smooth and rigid, consisting of non-volatile non-dissolving components, and does not absorb fluids; the system is closed to mass transfer with the reservoir, and hence, the total number of moles of any component i in the system, n_i, is constant. Although systems are at least partially open in experiments, it is reasonable to consider a closed system as the height of the liquid above the bubbles is much larger than the height of surface nanobubbles. We consider that there is only one dissolved gas in the liquid. Therefore, each of the liquid phase and the vapor phase has two components, H_2O (component 1) and the gas (component 2, CO_2 or N_2 in this work). The dividing surface of the curved liquid–gas interface is placed according to the "Gibbs surface of tension"[1] approach (interfacial tension independent of curvature); thus, both components 1 and 2 can be in excess at the liquid–gas interface. The dividing surface of the solid–gas interface and the solid–liquid interface are placed according to the "Gibbs dividing surface"[1] approach for flat surfaces, that is, such that there is no excess of the solid component at these interfaces, and therefore, both components 1 and 2 can also be in excess at these interfaces.

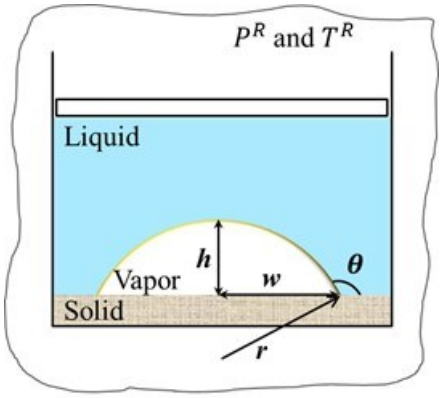

Figure 1. Schematic of a nanobubble formed on a smooth solid surface submerged in a liquid–gas solution and the definition of the geometric parameters. T^R and P^R are the temperature and pressure of the reservoir, respectively.

The independent variables of this system are the temperature, pressure, total number of moles of components 1 and 2, and size of the vapor phase. The size of each nanobubble can be expressed in terms of any two variables from the set of height (h), width (w), radius (r), and contact angle (θ), as illustrated in Figure 1. Only two of these four variables are independent because of the following geometrical relations

$$h = r(1 + \cos\theta) \tag{1}$$

$$w = r\sin\theta \tag{2}$$

Once the system is defined, thermodynamic stability analysis has three steps: [1,18,21,71–75] (I) finding equilibrium conditions, (II) determining the appropriate free energy of the system with respect to some reference state (the conditions for equilibrium, found in the previous step, are useful for further simplification of the expression of free energy), and (III) analyzing the stability of the new phase, that is, surface nanobubbles. The extrema of free energy versus size of the surface nanobubbles identify the equilibrium states that satisfy equilibrium conditions. The stable equilibrium condition is at the global minimum in free energy, which is equivalent to a maximum in the entropy of the system subject to constraints.

2.3.1. Conditions for equilibrium

When the system is at any form of equilibrium (stable, unstable, or metastable), the total entropy, S, of the system plus reservoir is an extremum; hence, the differential of the total entropy vanishes at equilibrium

$$\mathrm{d}S^{\mathrm{reservoir}} + \mathrm{d}S^{\mathrm{system}} = 0 \tag{3}$$

Substituting the constraints of the system discussed in the first paragraph of Section 2 in Equation (3) and simplifying gives the conditions for equilibrium in the system shown in Figure 1:[21]

$$T^R = T^S = T^L = T^V = T^{LV} = T^{SL} = T^{SV} = T \tag{4}$$

$$\mu_i^L = \mu_i^V = \mu_i^{LV} = \mu_i^{SL} = \mu_i^{SV} \qquad i = 1{,}2 \text{ (components in fluid phases)} \tag{5}$$

$$\gamma^{SV} - \gamma^{SL} = \gamma^{LV}\cos\theta_C \tag{6}$$

$$P^V - P^L = \frac{2\gamma^{LV}}{R_C} \tag{7}$$

$$P^L = P^R \tag{8}$$

where T is temperature, P is pressure, μ_i is the chemical potential of component i, superscripts L and V denote the liquid phase and vapor phase, and the interfaces are denoted by superscripts LV for liquid–vapor, SL for solid–liquid, and SV for solid–vapor. $\gamma^{\alpha\beta}$ is the interfacial tension of the $\alpha\beta$ interface. θ_C is the equilibrium contact angle measured through the liquid phase, and R_C is the Kelvin radius, that is, the radius of curvature of a nanobubble in equilibrium with the liquid–gas solution. Equation (6) is the Young equation, and Equation (7) is the Young–Laplace equation.

Combining the equality of chemical potentials between the liquid and vapor phases for each component i as expressed in the first equality in Equation (5) with the Young–Laplace equation, Equation (7), the radius of curvature of the nanobubble at equilibrium, that is, the

Kelvin radius, R_C, is obtained. In the expressions for the chemical potentials, we assume that the vapor phase is an ideal gas, that the liquid phase is incompressible, and that the liquid solution (gas dissolved in H_2O) is a dilute solution (hence that Henry's law is applicable). Ward and Levart[21] showed that with such assumptions the Kelvin radius is given by[21]

$$R_C = 2\gamma^{LV}/[\eta P_\infty + P^L(n_2^L/n_{2s}^L) - P^L] \tag{9}$$

where P_∞ is the saturation pressure of pure component 1, n_i^L is the number of moles of i in the liquid phase, and n_{2s}^L is the number of moles of gas dissolved in the liquid phase at P^L at the saturation limit across a flat interface. n_{2s}^L can be calculated from Henry's law for the slightly soluble gas,[21]

$$n_{2s}^L = n_1^L P^L / K_H \tag{10}$$

where K_H is Henry's law volatility constant, and at 298.15 K its value is 1.6×10^3 atm for CO_2 and 9.1×10^4 atm for N_2.[76]

The value of η is given by[21]

$$\eta = \exp\left[\frac{v_1^{0L}}{RT}(P^L - P_\infty) - \frac{n_2^L}{n_1^L}\right] \tag{11}$$

where v_1^{0L} is the molar volume of pure component 1 (water), R is the universal gas constant, and T is the temperature of the system (which is equal to the reservoir temperature from Equation (4)). η accounts for the difference in pressures of the liquid and vapor phases, as well as the effect of the dissolved solute.[21]

The Kelvin radius in Equation (9) is expressed in terms of liquid phase properties; hence, it is a thermodynamic property of the liquid phase, as mentioned by Ward *et al.*[18,21] According to Equation (7), the Laplace pressure at equilibrium is also linked to the properties of the liquid phase because equilibrium Laplace pressure is a function of the Kelvin radius.

To describe the Kelvin radius in terms of independent variables (T, P^L, n_1, n_2, and the size of the vapor phase), expressions for n_1^L and n_2^L in terms of independent variables are required. When neglecting the adsorption of components 1 and 2 at interfaces, compared to the total masses of each component, n_1 and n_2, we have[21]

$$n_1^L = n_1 - \frac{\eta P_\infty V^V}{RT} \tag{12}$$

$$n_2^L = \frac{n_2(n_1 RT - \eta P_\infty V^V)}{n_1 RT - \eta P_\infty V^V + V^V K_H} \tag{13}$$

where V^V is the volume of the vapor phase. In the case of a single nanobubble, V^V would be the volume of the nanobubble, but we can generalize our work to the case of more than one diffusionally non-interacting nanobubble by calling V^V the total volume of all nanobubbles that are present.

An iterative method is required to obtain η because η, n_1^L and n_2^L are functions of each other. However, for the conditions of our interest, the value of η given by Equation (11) is always very close to unity.[21] Substituting Equations (12) and (13) into Equation (9) and making use of Equation (10), the Kelvin radius in terms of the independent variables is given by[21]

$$R_C = \frac{2\gamma^{LV}(n_1 RT - \eta P_\infty V^V + V^V K_H)}{(\eta P_\infty - P^L) \times (n_1 RT - \eta P_\infty V^V + V^V K_H) + K_H RT n_2} \tag{14}$$

2.3.2. Free energy of the system

According to the second law of thermodynamics, the total entropy of the system plus reservoir increases for any change toward equilibrium ($\Delta S^{\text{reservoir}} + \Delta S^{\text{system}} \geq 0$) and remains constant once the equilibrium state is reached. The appropriate free energy (also called the thermodynamic potential) is obtained by combining the second law and the constraints of the system. The appropriate free energy of this system, B, is[21]

$$B = G^L + F^V + F^{LV} + F^{SL} + F^{SV} + P^L V^V \tag{15}$$

where G and F denote Gibbs and Helmholtz functions respectively. It should be noted that the appropriate free energy for this system is not any of the conventional thermodynamic potentials (such as Gibbs or Helmholtz) alone. An equivalent form of Equation (15) is[21]

$$\begin{aligned} B = {} & [\mu_1^L n_1^L + \mu_2^L n_2^L] + [-P^V V^V + \mu_1^V n_1^V + \mu_2^V n_2^V] \\ & + [\gamma^{LV} A^{LV} + \mu_1^{LV} n_1^{LV} + \mu_2^{LV} n_2^{LV}] + [\gamma^{SL} A^{SL} + \mu_1^{SL} n_1^{SL} + \mu_2^{SL} n_2^{SL}] \\ & + [\gamma^{SV} A^{SV} + \mu_1^{SV} n_1^{SV} + \mu_2^{SV} n_2^{SV}] + P^L V^V \end{aligned} \tag{16}$$

where $A^{\alpha\beta}$ is the surface area of the $\alpha\beta$ interface.

A convenient reference state is the condition where no vapor phase has formed yet. Considering the constraint of constant mass and assuming the reference state to be an equilibrium state, the free energy with respect to the reference state is given by[21]

$$\begin{aligned} B - B_0 = {} & -(P^V - P^L)V^V + (\gamma^{SV} - \gamma^{SL})A^{SV} + \gamma^{LV} A^{LV} \\ & + \sum_{i=1}^{2} \left[n_i^L (\mu_i^L - \mu_{i0}) + n_i^V (\mu_i^V - \mu_{i0}) + n_i^{SL} \left(\mu_i^{SL} - \mu_{i0}\right) \right. \\ & \left. + n_i^{SV} \left(\mu_i^{SV} - \mu_{i0}\right) + n_i^{LV} (\mu_i^{LV} - \mu_{i0}) \right] \end{aligned} \tag{17}$$

where subscript 0 refers to the reference state. The differences between intensive properties in Equation (17) were expanded around an equilibrium state to derive the free energy around the equilibrium state in terms of independent variables (T, P^L, n_1, n_2, and the size of the vapor phase)[21]

$$\begin{aligned} B - B_0 = {} & \frac{-2\gamma^{LV} V^V}{R_C} + \gamma^{LV}(A^{LV} + A^{SV}\cos\theta_C) \\ & + \frac{n_2 RT V^V (K_H - \eta P_\infty)}{n_1 RT - \eta P_\infty V^V + V^V K_H} + n_2 RT \ln\left(\frac{n_1 RT}{n_1 RT - \eta P_\infty V^V + V^V K_H}\right) \end{aligned} \tag{18}$$

For any bubble size, the change in the free energy of the parent phase (bulk phase) is not neglected in Equation (18). It should be noted that the liquid–vapor interfacial tension, γ^{LV}, changes with the solution concentration. To consider the effect of solute gas, we used the fit to

experimental data of interfacial tension versus pressure of solute gas at 298.15 K provided by Massoudi and King.[77]

$$\gamma = \gamma_0 + BP + CP^2 + DP^3 \tag{19}$$

where γ_0 is the surface tension (in N/m) of water in equilibrium with its pure vapor at 298.15 K. Coefficients *B*, *C*, and *D* are fitting parameters, which for nitrogen are given as -8.35×10^{-5} $\mathrm{N/m.atm}$, 1.94×10^{-7} $\mathrm{N/m.atm^2}$ and zero, and for carbon dioxide are given as -7.789×10^{-4} $\mathrm{N/m.atm}$, 5.43×10^{-6} $\mathrm{N/m.atm^2}$, and 4.2×10^{-8} $\mathrm{N/m.atm^3}$respectively.[77] *P* was the gas phase pressure in the experiments of Massoudi and King,[77] but here we will replace it with the partial pressure of the solute gas. From the conditions for equilibrium (Equation (5)), the partial pressure of the solute gas is found to be[21]

$$P_2^V = n_2^L P^L / n_{2s}^L \tag{20}$$

Although γ^{LV} should be explicitly independent of curvature according to Gibbs surface of tension approach, here it implicitly depends on size because the partial pressure of the solute gas changes as the bubble size changes.

The three geometric terms V^V, A^{LV}, and A^{SV} in Equation (18) can be expressed in terms of θ and r of the bubbles. Alternatively, any combination of two variables from h, w, r, and θ can be selected because h and w are related to θ and r through Equations (1) and (2). However, because θ_C is explicitly present in Equation (18), it is convenient to keep θ as one of the two independent geometric variables.

We consider the vapor phase to consist of q non-interacting surface bubbles of equal sizes. Therefore, the geometric terms in Equation (18) can be expressed as

$$V^V = q \times \frac{\pi r^3}{3}(1+\cos\theta)^2(2-\cos\theta) \tag{21}$$

$$A^{LV} = q \times 2\pi r^2(1+\cos\theta) \tag{22}$$

$$A^{SV} = q \times \pi r^2 \sin^2\theta \quad (23)$$

Substituting Equations (21) to (23) in Equation (18), the free energy can be expressed in terms of independent variables of the problem, $T(=T^R)$, $P^L(=P^R)$, n_1, n_2, q, θ_C, θ, and r. Alternatively, the number of moles of gas, n_2, can be calculated from a specified degree of saturation, f, at the initial condition before bubble formation—all molecules are in the liquid—as follows

$$n_2 = f(n_1 P^L / K_H) \quad (24)$$

where $f < 1$ for an undersaturated solution and $f > 1$ for a supersaturated solution.

For a particular system with known T, P^L, n_1, n_2 (or alternatively f), and θ_C and q nanobubbles, a plot of free energy versus size of the nanobubble (r or w or h) reveals whether stable nanobubbles can exist.

2.4. Thermodynamic stability results and discussion

2.4.1. Number and nature of equilibrium states

Regardless of the reason for the anomalously high contact angle of surface nanobubbles (our argument in the next section, pinning theory,[59] or simply experimental observations), for the rest of the free energy analysis in this study we consider the equilibrium contact angle to be known. To investigate the stability of nanobubbles, we consider an example case with 5 moles of water as the solvent at a constant temperature of 25 °C and a constant pressure of 1 atm, with a supersaturation of $f = 2.5$. The equilibrium contact angle is assumed to be 164° from measurements[45] (measured through the liquid and is higher than the macroscopic contact angle reported to be 101–112°). Figure 2 shows the free energy versus height of a nanobubble for two systems with different solutes, carbon dioxide (CO_2), and nitrogen (N_2). Nitrogen is less soluble in water than carbon dioxide. Therefore, the same amount of initial supersaturation results in more nanobubbles of a certain size for CO_2 in the case of Figure 2

where the total number of moles of the solvent and degree of initial saturation are set parameters. Experiments show nanobubbles to be stable for hours when the solute is carbon dioxide, and for days when the solute is nitrogen.[38,45] This lends support to our assumption that on the time scale of experiments the stable nanobubbles are in equilibrium with the surrounding initially supersaturated liquid. On longer time scales, the gas is removed from the liquid to the room far from the nanobubbles and gas must dissolve and diffuse through a large amount of liquid, a slow process that would be faster for a more highly soluble gas.

(a) CO_2

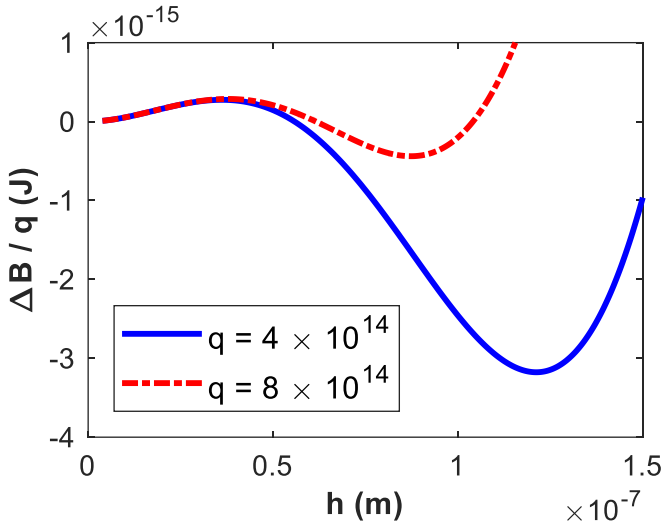

(b) N_2

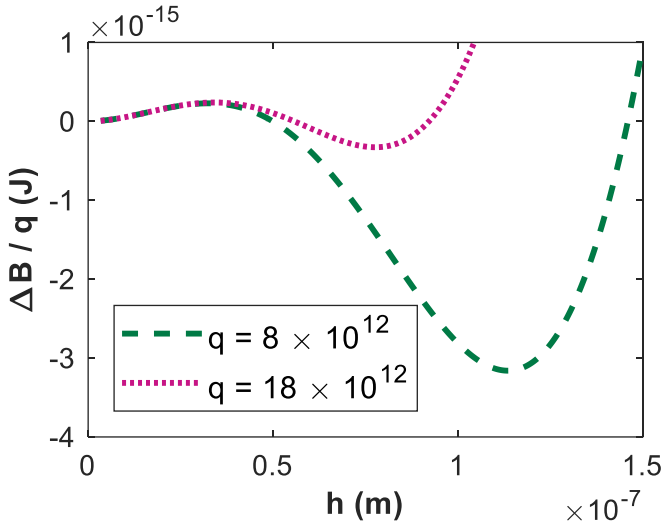

Figure 2. Free energy versus height of the nanobubble for a system at 25 °C and 1 atm, with 5 moles of solvent (water), under an initially supersaturated condition of f = 2.5. The equilibrium contact angle is assumed to be known and is 164° (measured through the liquid). Two systems with two different solutes are presented: (a) carbon dioxide and (b) nitrogen.

According to Figure 2, the free energy curve of an individual bubble in a system with q bubbles reaches a global minimum point, that is, a stable equilibrium condition, after passing a maximum (unstable) point. The maximum point is the energy barrier that must be overcome for the bubble to nucleate from the supersaturated liquid. For the number of bubbles considered in Figure 2, the height of the bubble is on the order of nanometers (between 80 and

100 nm). Figure 2 also shows that as the number of bubbles decreases, individual bubbles must overcome a smaller energy barrier to evolve to stable equilibrium. Moreover, as the number of bubbles decreases, the stable equilibrium state would have a larger bubble height and more stability. The most stable case would be one bubble with a macroscopic size. Considering q bubbles of equal size is equivalent to partitioning the liquid into regions each surrounding a single nanobubble and assuming that each region has limited gas exchange with another region on the time scale of the experiments. This treatment is a way to include the limited diffusion between neighboring bubbles on short time scales into the analysis. This approach is necessary to consider only thermodynamic consequences of local supersaturation and not to consider kinetic aspects of diffusive transport between bubbles. As the number of bubbles (q) increases, the initial barrier and the size of the critical initial nucleus increase, whereas the size and stability of the stable equilibrium point decrease. It should be noted that the q non-interacting bubbles are considered to form simultaneously, and the formation of an individual surface bubble is therefore not affected by a previously formed bubble.

While plotting Figure 2 it was assumed that the geometric contact angle θ in Equations (21) to (23) is equal to the equilibrium contact angle θ_c appearing in Equations (6) and (18). In Figure 3, the geometric contact angle was varied and the 3D plot illustrates free energy *vs.* radius *vs.* geometric contact angle. The graph has a minimum point with radius equal to equilibrium radius (*i.e.*, Kelvin radius) and the contact angle equal to the equilibrium contact angle (considered to be known in this study). This minimum point is the stable equilibrium state of the system.

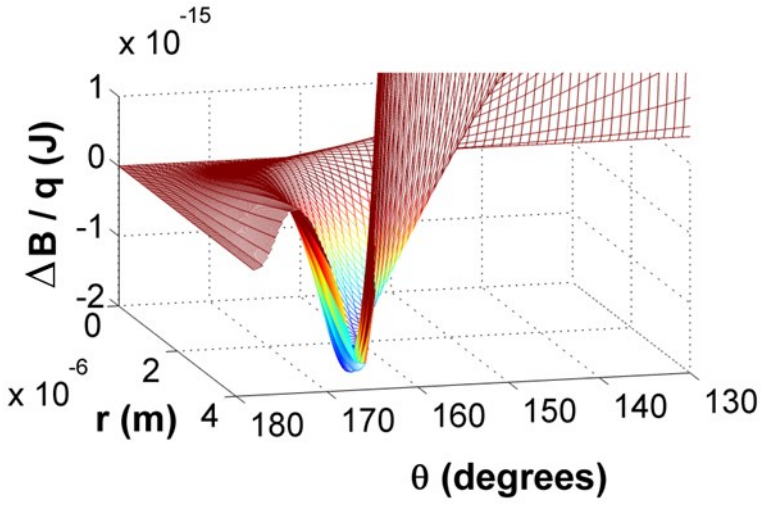

Figure 3. Free energy versus height versus geometric contact angle of the nanobubble for a system of water and carbon dioxide at 25 °C and 1 atm, with 5 moles of solvent (water), and 5×10^{14} bubbles under an initially supersaturated condition with f = 2.5. The equilibrium contact angle is assumed to be known, and is 164° (measured through the liquid).

2.4.2. Effect of degree of saturation

Figure 4 shows curves of free energy for CO_2 in a water solution, where all of the conditions are kept the same as those in Figure 2, except that the liquid is originally at an undersaturated condition (the degree of saturation f is 0.98). By increasing the number of bubbles, the size of the stable height reduces to a certain macroscopic value. Further increase of the number of bubbles results in constantly ascending curves of free energy versus size, implying that phase transition becomes unfavorable. Likewise, for saturated conditions, our results show that only bubbles with macroscopic height can be stable. Therefore, supersaturation, such as the amount shown in Figure 2, is essential for stable surface nanobubbles to exist.

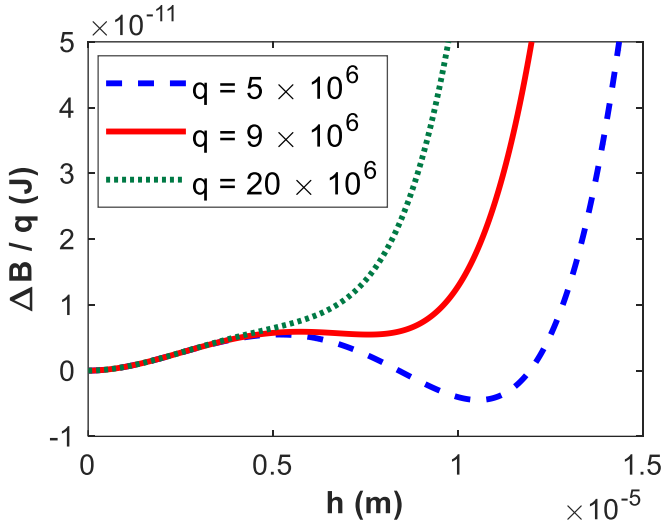

Figure 4. Free energy versus height of the nanobubble for an undersaturated solution at 25 °C and 1 atm, with an undersaturation f of 0.98, and 5 moles of solvent (water). The equilibrium contact angle is assumed to be known at 164° (measured through the liquid). The solute is carbon dioxide.

Figure 5 describes the effect of the supersaturation amount on the equilibrium states. In Figure 5(a), with the presumed number of bubbles ($q = 4\times10^{14}$), when supersaturation f is 2.6, the free energy curve has a maximum and a minimum, indicating unstable and stable equilibrium states, respectively. Nanobubbles adopt the stable equilibrium condition after passing an energy barrier. As the amount of supersaturation decreases (an example of which is f equal to 2.3 in Figure 5), the unstable radius gets larger with a higher energy barrier, and the stable equilibrium becomes smaller in size and less stable. At some threshold level of supersaturation (f = 1.99 for the conditions of Figure 5), the free energy curve forms an inflection point, which is stable against growth and unstable against dissolution. That is the most favorable state for the system is for the gas to dissolve back into the liquid and no bubble to be present. At supersaturation lower than this threshold, the free energy curve becomes monotonically increasing. This means that nanobubble formation is energetically unfavorable, and the system is out of equilibrium at any size of bubble present.

Figure 5(b) shows the intersection method[18] to understand the number and nature of equilibrium states. At equilibrium conditions, the physical (geometric) radius of the nanobubble, r, must be equal to the computed equilibrium radius (also called the Kelvin

radius), R_C. Therefore, computed R_C is plotted as a function of geometric radius r, and equilibrium states are identified at locations where the computed curve crosses the line $R_C = r$. For example, in Figure 5(b) at a supersaturation of f = 2.6, there are two locations where the curve of computed R_C crosses the line $R_C = r$ denoted by points 1 and 2 on the figure. It was noted from studying the case of constant R_C that if the computed equilibrium radius R_C is greater than the physical radius r then mass will come out of the bubble; and if the computed equilibrium radius R_C is lower than the geometric radius r, then mass will go into the bubble.[18] This behavior was generalized to the case where the computed equilibrium R_C varies with the geometric radius,[18] which is the case here. The nature of the equilibrium state (stable or unstable) is determined based on the system response to a perturbation, where a perturbation is a change in the geometric radius (r) of the system. The equilibrium state is stable to a given perturbation if the bubble moves in the opposite direction of the perturbation (returns to the unperturbed state) and is unstable to the given perturbation if the bubble moves in the same direction as the perturbation (away from the unperturbed state).[18] For example, for point 1 in Figure 5(b), if the system is perturbed to a larger geometric size (r), moving along the green dot-dashed line, R_C becomes lower than the geometric radius (the green dot-dashed curve is below the line $R_C = r$); hence, mass should go into the bubble and the bubble size increases further. As both the perturbation and the system response are in same direction (size increase), point 1 is unstable against growth. On the other hand, for point 1, if the radius is decreased because of a perturbation, R_C becomes larger than the geometric radius (the green dot-dashed curve is above the line $R_C = r$), and hence, mass will move out of the bubble, and the bubble size will decrease. Because both the perturbation and the response of the system are size reduction; point 1 is unstable against shrinkage. Point 1 in Figure 5(b) corresponds to the maximum point in the free energy curve of Figure 5(a). With similar logic, it can be seen that point 2 is stable against both growth and dissolution, corresponding to the minimum point in the free energy curve of Figure 5(a). As the amount of supersaturation decreases at some threshold supersaturation value (f = 1.99 in Figure 5), the R_C versus r curve becomes tangent

to the line $R_C = r$. This tangent intersection (point 3 in Figure 5(b)) is stable against growth yet unstable against dissolution, and corresponds to the inflection point in the free energy curve of Figure 5(a). With a further decrease in the amount of supersaturation, the curve of R_C versus r has no intersection with the $R_C = r$ line, indicating that the system is out of equilibrium at any size of the bubble and thus will correspond to monotonically increasing curves in Figure 5(a). For example, see the purple dotted curves in Figure 5 (a) and (b) corresponding to f = 1.70.

(a)

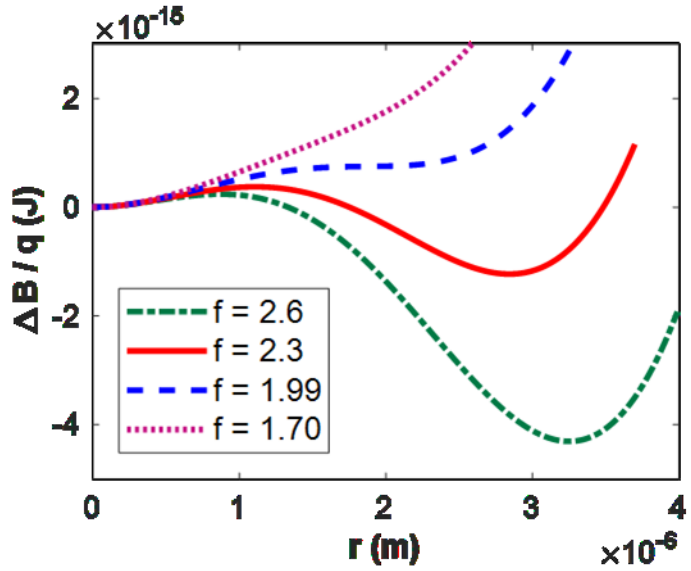

(b)

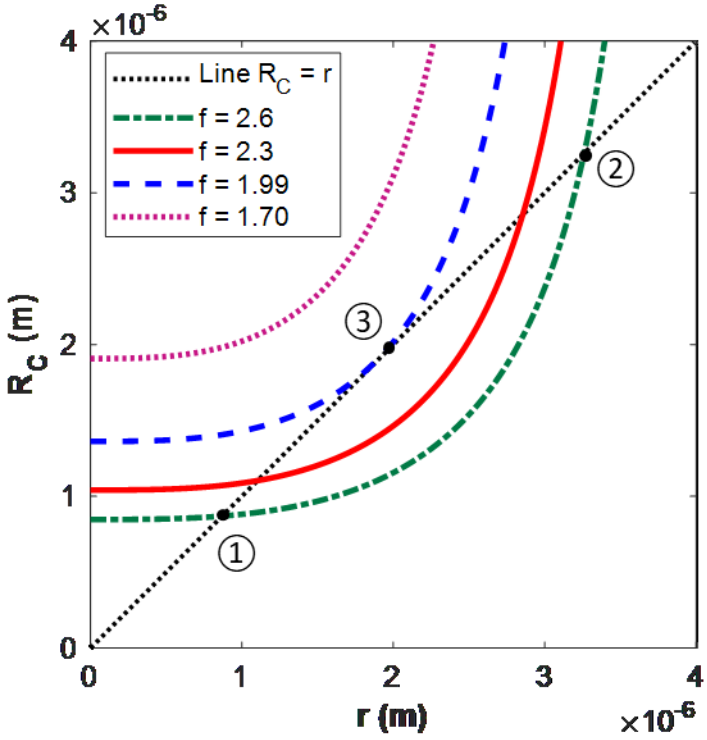

Figure 5. (a) Effect of the amount of supersaturation on equilibrium states for carbon dioxide in water solution at 25 °C and 1 atm, with 5 moles of solvent (water). It is assumed that the number of bubbles (q) is 4×10^{14} and that the equilibrium contact angle is 164° (measured through the liquid). (a) Free energy graph and (b) the intersection method, where equilibrium states are indicated by intersections of computed equilibrium radius R_C versus geometric radius r with the line $R_C = r$.

2.4.3. Effect of equilibrium contact angle

Figure 6 illustrates that nanobubbles cannot be stable if the equilibrium contact angle remains at the reported macroscopic contact angle[45] between 101 and 112° (measured through the liquid phase). A larger equilibrium contact angle results in more stable nanobubbles, as shown in Figure 6.

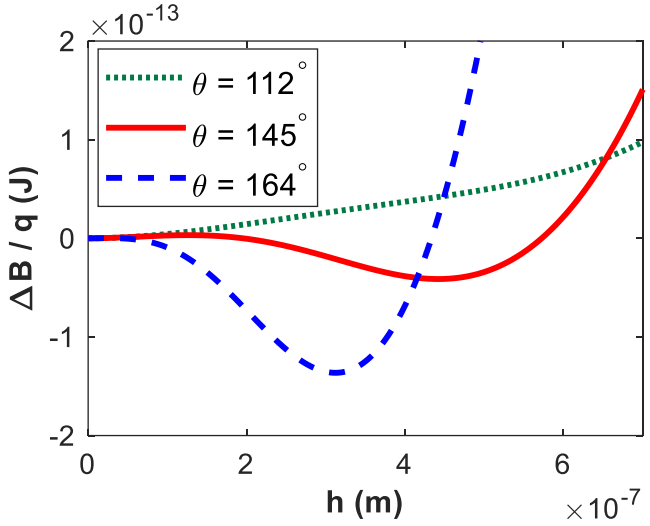

Figure 6. Free energy versus height of the nanobubble for different values of the equilibrium contact angle. The system has 5 moles of solvent (water) at 25 °C and 1 atm, initially supersaturated with $f = 3$, with the number of nanobubbles being $q = 5\times10^{13}$. The solute is carbon dioxide.

2.5. Explanation for the anomalously high contact angle of surface nanobubbles using a combination of the Koch–Amirfazli–Elliott[78] framework and existence of the gas enrichment layer

It is generally accepted that pure water cannot have a contact angle greater than approximately 120° on a homogeneous smooth rigid surface.[79] To have larger contact angles requires (*i*) adsorption at interfaces, (*ii*) a rough or heterogeneous solid, or (*iii*) contact line pinning; previous theoretical discussion of the anomalously high contact angle for surface nanobubbles each involves one of these mechanisms. To explain the high contact angle of nanobubbles, here we will discuss the implications of the existence of a gas enrichment layer at the solid surface combined with a recent framework proposed by Koch, Amirfazli, and

Elliott[78] which incorporates resistance to contact line motion into the understanding of contact angles. There is independent support for both the contact angle framework of Koch, Amirfazli, and Elliott,[78–80] and the gas enrichment layer. However, the validity of this section does not depend on the experiments for the gas enrichment layer as we have not used any experimental value from gas enrichment layer supporting experiments. Rather, herein we theoretically investigated the consequence of the assumption of the existence of a gas enrichment layer. It should also be noted that the ideal homogeneous surface assumed in sections 1 to 3 can describe either a bare surface or a surface with an adsorbed gas layer. In the derivation of the conditions for equilibrium in section 1, the choice of the "Gibbs dividing surface" approach for the solid surface meant that both components 1 and 2 can be in excess at the solid surface. The existence of an adsorbed gas enrichment layer would mean a surface excess of component 2. The effect of the adsorbed gas layer would have been captured by the experimental contact angle.

There is experimental evidence[61–63] for the existence of a gas enrichment layer at the solid surface under the conditions of formation of surface nanobubbles (*i.e.*, after the solvent exchange and with the supersaturation). This gas enrichment layer would not be present when the contact angle of water at the same hydrophobic surface is measured in the usual way with a macroscopic phase, that is, without the solvent exchange and resulting supersaturation.

In a series of papers,[78–80] Koch, Amirfazli and Elliott proposed a theoretical framework connecting experimentally accessible advancing and receding contact angles to thermodynamic equilibrium contact angles (the Young contact angle in the case of smooth solid surfaces and the Cassie–Baxter and Wenzel contact angles in the case of rough solid surfaces). In this framework it is supposed that when the contact line is moving across the solid, an additional surface force opposing the contact line motion is added into the equilibrium force balance that yields the contact angle. The magnitude of the introduced surface force (a two-dimensional force per unit length with the same units as interfacial

tension) is obtained empirically by comparing the force balance to measured contact angles. It is important to understand that a surface force determined in this way would empirically account for all phenomena that cause advancing and receding contact angles to be different from thermodynamic equilibrium contact angles. A surface force determined in this way could represent an actual frictional or pinning force, but could alternatively be a way to account for effects left out of thermodynamics such as disjoining forces arising from molecular interactions between interfaces, non-equilibrium redistribution effects in the case of surfactants, and local geometric constraints on the contact angle in the case of rough surfaces. This framework is very useful since it gives theoretical validity to the experimentally confirmed practice of cosine averaging of measured advancing and receding contact angles to estimate the Young contact angle for smooth surfaces and explains why cosine averaging should never be used for rough surfaces.[78] As well, the framework is able to provide an explanation for a wide variety of seemingly inexplicable experimental results for contact angles on rough hydrophobic,[78] wetting,[80] and oleophobic[79] surfaces. The framework also allows one to gain additional insight into contact angle phenomena by comparing the magnitude of the extra surface forces between different experimental circumstances.[79]

Let us consider the effect that the gas enrichment layer and the Koch–Amirfazli–Elliott framework would have for surface nanobubbles. According to the hypothesis of the interfacial gas layer[47,60] the surface nanobubble sits on a gas enrichment layer (denoted by *E*) as shown in Figure 7. When the nanobubble is first formed, the bubble nucleates and grows to its stable size according to the initial local supersaturation; thus, the contact angle would be a receding contact angle (noting that the contact angle is measured through the liquid) and the force opposing the contact line motion, F_R, would be as shown in Figure 7 (a). At long experimental times, as the dissolution of the bubble becomes appreciable and the nanobubble is shrinking, the contact angle will eventually become an advancing contact angle and the force opposing the contact line motion will be as shown in Figure 7 (b).

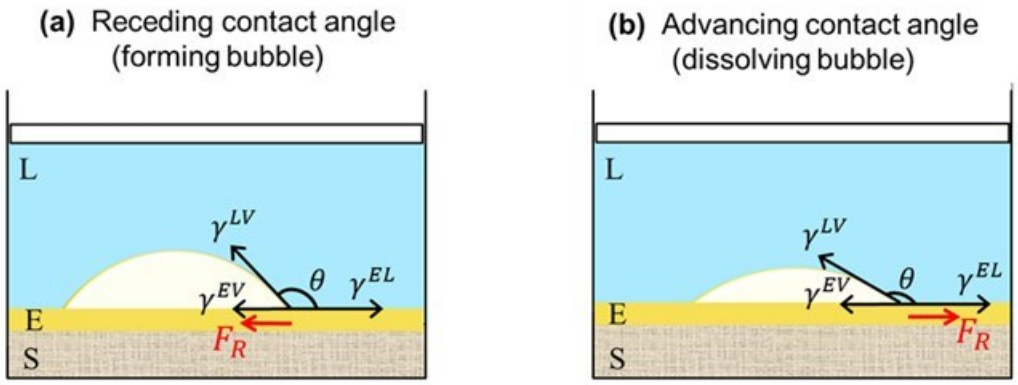

Figure 7. Surface nanobubble sitting on the gas enrichment layer, according to the interfacial gas layer hypothesis.[47,60] γ^{EV}, γ^{EL}, and γ^{LV} are the interfacial tensions of the gas enrichment layer with the vapor in the bubble, the gas enrichment layer with the liquid solution, and the liquid solution with the vapor in the bubble, respectively. F_R is the resistance force opposite to the direction of contact line motion in the case of (a) receding contact angle (growing bubble) and (b) advancing contact angle (shrinking bubble).

The receding contact angle, θ_{Rec}, and the advancing contact angle, θ_{Adv}, are given by[78]

$$\cos\theta_{Rec} = \frac{\gamma^{EV} - \gamma^{EL} + F_R}{\gamma^{LV}} \tag{25}$$

$$\cos\theta_{Adv} = \frac{\gamma^{EV} - \gamma^{EL} - F_R}{\gamma^{LV}} \tag{26}$$

where we have assumed that the force opposing contact line motion in the receding and advancing cases is equal and opposite as is appropriate for smooth surfaces.[78] γ^{EV} is the interfacial tension of the gas enrichment layer with the vapor phase inside of the nanobubble, and γ^{EL} is the interfacial tension of the gas enrichment layer with the liquid.

Assuming that the gas enrichment layer consists of the same gas type as the bubble, we take γ^{EV} to be zero, and assuming the enrichment layer–liquid interface to be flat, we take γ^{EL} to be γ^{LV} for a macroscopic size (which is almost equal to γ^{LV} of pure water, *i.e.*, 71.9 mN/m). We take γ^{LV} of the surface nanobubble to be 70.7 mN/m, that is the value of interfacial tension at the stable equilibrium point (minimum point) for CO_2 solution for the condition of

Figure 2 with 8.5×10^{14} bubbles. Substituting these values and the observed (receding) contact angle of surface nanobubbles of 164° in Equation (25) yields a value for F_R of 3.94 mN/m.

Thus, the existence of a gas enrichment layer combined with the Koch–Amirfazli–Elliott framework with a surface force of 3.94 mN/m resisting contact line motion can explain the anomalously high contact angle of surface nanobubbles. Next, we compare the magnitude of this surface force to that of other known forces to see whether this magnitude of surface force is reasonable. First, we note that the obtained surface force is very small, more than one order of magnitude smaller than the liquid–vapor interfacial tension and more than one order of magnitude smaller than the values of F_R found for water on rough surfaces.[78] Next, we can obtain the value for F_R in the case of macroscopic contact angle measurements on the same hydrophobic surface as was used in the nanobubble experiments (but without the conditions of solvent exchange, water supersaturation, and therefore a gas enrichment layer being present). For any smooth surface, an equation analogous to Equation (26) can be subtracted from an equation analogous to Equation (25) to yield[78]

$$F_R = \gamma^{LV}(\cos\theta_{Rec} - \cos\theta_{Adv})/2 \tag{27}$$

Substituting the values of the reported macroscopic contact angles (101 and 112° from measurements for receding and advancing contact angles, respectively[45]) and the macroscopic interfacial tension of 71.9 mN/m for γ^{LV}, the resistance force for a macroscopic bubble is found to be 6.61 mN/m. The value for F_R on the gas enrichment layer in the case of nanobubbles is approximately a factor of 2 smaller than that for the hydrophobic surface. This is reasonable because it implies that the gas enrichment layer reduces the interactions of the liquid and interfaces with the solid that contribute to the surface force F_R.

Finally, we consider what this nanobubble theory (role of the gas enrichment layer and the Koch–Amirfazli–Elliott framework) would say about the behavior of surface nanobubbles as they shrink and disappear at long experimental times. In the case of shrinking nanobubbles,

Equation (26) would apply. Substituting F_R = 3.94 mN/m in Equation (26), we see that this small force is more than enough to balance the interfacial tensions in the advancing contact line case (shrinking nanobubble) and that therefore the advancing contact angle would be 180°. Thus, as in other experiments in which a receding contact angle changes to an advancing contact angle or vice versa, we expect the bubble shrinkage to occur first by changing the contact angle without changing the contact footprint of the bubble and only when the advancing contact angle of 180° is reached for the contact footprint to reduce. In other words, as the nanobubble is shrinking, the contact line would appear pinned initially. In 2013, an important series of experiments were performed to see if contact lines were pinned.[41] The authors felt that the results indicated that the contact lines are pinned both when nanobubbles are growing and when nanobubbles are shrinking.[41] However, upon looking at the data presented, it is clear that the interpretation is complicated. First, we note that different behavior is seen for different sizes of nanobubbles. Ostwald ripening processes are evident in that during shrinking experiments, smaller nanobubbles shrank more quickly than larger nanobubbles; nanobubbles with initial heights below 50 nm (widths below 420 nm) dissolved completely within the time of the experiment. For nanobubbles that were reasonably large (initial heights larger than 50 nm and widths larger than 420 nm) their widths shrunk little (although they did shrink some) during bubble dissolution, which might be interpreted as pinning. Interestingly the calculated radii of curvature of larger nanobubbles (initial heights larger than 50 nm and widths larger than 420 nm) all went through a maximum during the bubble shrinkage experiment, indicative of more complex stick–slip behavior rather than the simple pinned or unpinned interpretation. The bubble growth experiments were with flatter bubbles—bubbles had probably been shrinking prior to the start of the experiment—and their contact lines appeared pinned as one might expect if bubbles were in the process of switching from shrinking to growing. There was not as much variation between bubbles, or as much change in the bubble size during the experiments, for the bubble growth experiments as

compared to the bubble dissolution experiments. Also only two time points were measured, so no comments can be made about complicated Ostwald ripening or stick–slip processes.

The explanation presented here for the anomalously high contact angle of surface nanobubbles is satisfactory in several respects: (i) it explains the observed contact angle that is known to be unobtainable for a pure liquid on a smooth surface, (ii) it uses only concepts that have independent support (gas enrichment layer and Koch–Amirfazli–Elliott framework), (iii) the required resistance forces are very small upon comparison with other surface forces, as expected, (iv) it is in agreement with the experimentally observed constant contact footprint (pinning) of nanobubbles during shrinkage at long experimental times,[41] and (v) it is consistent with the experimental observation that although the observed contact angle of surface nanobubbles is dependent on gas type, it is independent of the type of hydrophobic solid.[60] The argument presented here for the anomalously high contact angle of surface nanobubbles lends support to the existence of the gas enrichment layer; however, the explanation presented here also raises some questions that cannot be answered at this time. This explanation depends on the existence of the interfacial gas layer. Although there is some experimental support[61–63] and some simulation support[47,64–66] for the existence of this gas enrichment layer, its existence is not universally accepted, with alternate interpretations of experimental results put forward.[2,51] As well as requiring the existence of the gas layer, the explanation presented here also requires that the gas enrichment layer forms first before the growth of nanobubbles and that nanobubbles grow on top of it. This could be possible if the formation of the interfacial gas layer is by individual molecule adsorption rather than by nucleation; nucleation of the nanobubble requires a sizeable fluctuation and thus will require time to occur. In our thermodynamic stability analysis, we did not describe adsorption at the solid interface; rather we took the equilibrium contact angle that would result from such adsorption as a known value obtained from experiments. Ward *et al.*[81,82] have had success applying their zeta isotherm to understand the effect on the contact angle of adsorption of molecules of a wetting fluid at a solid surface;[81,82] however, the zeta isotherm has not yet been

applied in a two-fluid-component case. Finally, it is not clear how the interfacial gas layer is different from the gas inside of the surface nanobubble or how the gas enrichment layer interacts with the gas inside of the surface nanobubble such that the nanobubble could have an interface and a contact line with the gas enrichment layer and have a resistance to motion across the gas enrichment layer. Such an understanding of the actual molecular arrangement and properties of the gas enrichment layer requires information from outside of thermodynamics and will require more experimental investigation.

2.6. Chapter Conclusions

In the present study, we investigated the stability of surface nanobubbles (surface bubbles with nanometric height) in a two-component liquid solution, at constant temperature and constant bulk pressure. The free energy of such a system is denoted by B, presented in Equation (15), which is a combination of Gibbs free energy of the liquid phase, Helmholtz free energy of the vapor phase and interfaces, and another extra term. In our calculations we considered the solubility of the gas in water (solvent), as well as the dependence of the bulk phase concentration on the size of the surface bubbles. The key point in the investigation is to consider the changes in the properties of the bulk phase as the bubble grows further. Such changes should not be ignored especially after passing the critical size of the maximum point (which is the energy barrier for nucleation).

As the number of surface bubbles decreases through Ostwald ripening or collision and coalescence, the system will have more stable surface bubbles with a larger size. This behavior is similar to the case of bulk bubbles explained by Wasai *et al.*[17] Ostwald ripening is slow for a small amount of dissolved gas and the chance of collision and coalescence becomes very low if the surface bubbles are far from one another.

Our thermodynamic modeling of surface nanobubbles shows that surface nanobubbles can be stable only in supersaturated solutions and with an anomalously high contact angle

(measured through the liquid phase). When a liquid solution is undersaturated or saturated, only bubbles with macroscopic height can be stable.

A possible explanation for the anomalously high contact angle (measured through the liquid phase) is offered through a combination of the existence of a gas enrichment layer with the contact angle framework proposed by Koch, Amirfazli, and Elliott.[78] The gas enrichment layer alters the solid–fluid interfacial tensions. In the Koch–Amirfazli–Elliott framework,[78] a force resisting contact line motion is added, as shown in Equations (25) and (26). This resistance force would empirically account for factors such as pinning that cause advancing and receding contact angles to be different from the equilibrium contact angle. As explained earlier, the value of the resistance force is reasonably low compared to the interfacial tensions and other known resistance forces.

The thermodynamic approach presented here can shed light not only on nanobubbles but also on nanodroplets. Nanodroplets have been the focus of interest in recent years.[2,83] In previous work, our group investigated the rich behavior predicted by a thermodynamic stability study of homogeneous nanodroplets.[75] Lohse and Zhang[2] in their review paper reported similarities between surface nanobubbles and surface nanodroplets in terms of production methods and stability. Our previous thermodynamic studies[72,73] showed that the formation and stability of bubbles and drops in pure fluids could be understood to be analogous for different scenarios of new fluid phase formation inside solid gaps with different geometries. The big-picture understanding provided by multicomponent, multiphase thermodynamics adds to the rapidly developing experimental and theoretical investigations already in the literature on the topic of surface nanobubbles.

3. Bubble formation in a finite cone: More pieces to the puzzle

3.1. Chapter summary

We investigate the stability of bubble formation, starting with a convex or a concave meniscus, from a liquid solution inside a finite cone at constant temperature and constant liquid pressure (above the saturation pressure of the pure solvent). The number and nature of equilibrium states are determined with Gibbsian composite-system thermodynamics, both from the intersection of the equilibrium Kelvin radius with the geometry radius, and from the extrema in the plot of free energy of the system versus size of the new phase. Bubble stability is studied along the whole growth path, as the bubble grows inside, gets pinned, and grows further outside the finite cone. The changes in the concentration of the liquid bulk phase and the vapor phase during the growth of the bubble are carefully incorporated in the equations. For a bubble starting with a convex meniscus, a stable bubble may only form from a liquid with an initial degree of saturation above a certain value, depending on the system specifications. For a bubble starting with a convex meniscus, the bubble may experience "formation–disappearance fluctuation" when the energy barrier is sufficiently small and of comparable size to the energy well of the stable point. For a bubble starting with a concave meniscus, there is always a stable equilibrium, that may be with a concave meniscus inside or pinned, or with a convex meniscus pinned or outside the cone, depending on system specifications. The effect of various parameters including: cone apex angle, cone half mouth radius, contact angle, total number of moles, and initial degree of saturation, on the stability of the bubble are also investigated. Stability of bubble formation from a liquid solution inside a confined geometry such as a finite cone is of interest in areas such as restoring underwater superhydrophobicity, and adhesion of particles to the roughness of synthetic materials.

3.2. Introduction

Formation of a stable vapor phase on a rough solid surface submerged in a liquid solution has a significant role in many applications. Superhydrophobic surfaces that practically remain dry in submerged condition are valuable for several applications such as drag reduction,[22,23] and nucleation sites to promote nucleate boiling heat transfer[24,25] that can lead to higher heat transfer coefficients compared to film boiling. The presence of stable bubbles on the rough surface also influences the adhesion of particles to the surface, having application in areas such as separation of water contaminants, manipulation of adsorption on solid surfaces, reduction of biofouling,[26,27] and adhesion of blood platelets to the roughness of synthetic biomaterials,[28] among many others.[2] Theoretical study of the stability of bubble formation in the roughness is essential for optimal design in any of the applications.

Several thermodynamic studies of vapor phase trapped in the solid roughness submerged in a liquid solution predicted that submicroscopic roughness spacing is required to sustain vapor.[24,30–32] Jones *et al.*[33] conducted a thermodynamic study on conical roughness, as a roughness geometry for which the wetted state is unfavorable and the wet-to-dry transition can be induced spontaneously. In comparing conical versus cylindrical roughness, they mentioned that spontaneous dewetting does not happen in cylindrical pores because they have a base area that must be dewetted to initiate the wet-to-dry transition.[33] (A similar point was made by Zargarzadeh and Elliott in comparing nucleation of a pure fluid in an infinite cone to nucleation in the gap between solids.[17]) The above mentioned thermodynamic studies[24,30–33] only focus on cases where the solid material was such that vapor formed with a concave meniscus out of the liquid phase inside the pit. However, they[24,30–33] did not extend their investigation to whether it is favorable for the vapor to grow outside the pit.[24,30–33] Nor did they[24,30–33] investigate the cases where the solid material is such that vapor formation starts with a convex meniscus. There were other thermodynamic studies that showed stable bubble formation starting with a convex meniscus inside a conical pore at constant volume and temperature[29] or at constant pressure and temperature.[21] However, those works[21,29] did not

fully discuss the effect of geometric parameters, contact angle, or the initial number of components in the system.

The purpose of this research is a comparative study of thermodynamic stability of vapor formation starting inside a finite conical pore exposed to a liquid solution of water and a dissolved gas (solute). The analysis is presented for two different cases where vapor starts with either a concave or convex meniscus, depending on the solid material and geometric shape. We investigate the energy of the system as the vapor starts inside the cone, gets pinned to the corners of the finite cone, and grows out of the cone, to find the most stable equilibrium configuration of the system. The same analysis method as in the article by Ward and Levart[21] and our previous study of interfacial nanobubbles[84] is applied to the cases of the present study, combined with appropriate geometry equations. For each case in this study, we investigate the effects of the geometric parameters, contact angle, total numbers of moles, and the initial degree of saturation of the liquid solution. We have previously conducted similar comparative studies for different geometries, including a conical pore of infinite height, for the case of pure (single-component) vapor formation out of a bulk liquid phase, or liquid formation out of a pure bulk vapor phase.[72,73] In the present research both the vapor phase and the bulk liquid phase are considered to be a binary mixture of water and the solute gas (nitrogen). We carefully considered the concentration change in both liquid and vapor phases as a result of changes in the size of the bubble and the liquid–vapor interface radius of curvature. The current research will extend our previous big-picture understanding for confined pure phase transitions[72,73] to impure, multicomponent (binary in the present work) phase transitions inside microscopic confinement, for the real situation of a nucleated gas phase starting inside a finite conical pit in a solid surface.

3.3. System definition and governing equations

3.3.1. System definition

The system of interest is a bubble in the conical roughness of a solid submerged in a liquid solution, at constant temperature and liquid pressure, denoted by a movable piston in Figure 8, and closed to mass transfer with the surrounding thermal reservoir.

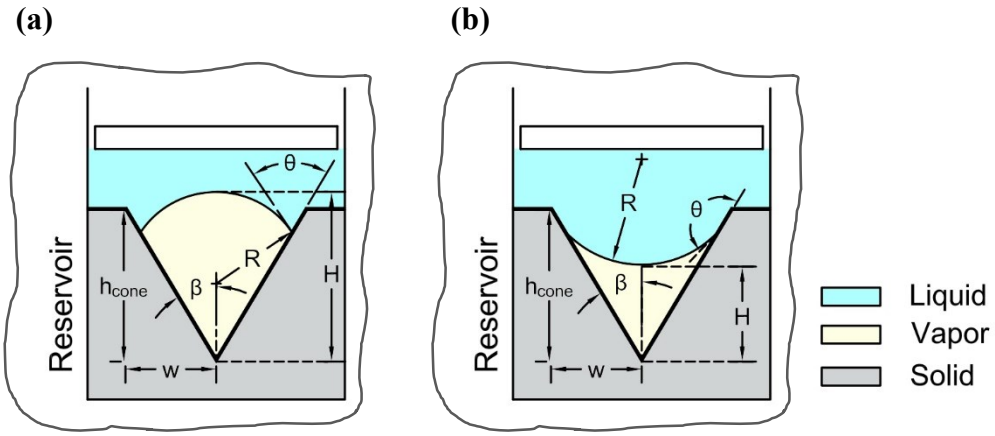

Figure 8. Schematic of the system in which a bubble forms in the conical roughness of a solid surface submerged in a liquid solution at constant temperature and liquid pressure, and closed to mass transfer. Based on the solid material, the bubble may start forming inside with a) a convex or b) a concave meniscus. β is half of the cone apex angle, w is the mouth radius of the conical pit, and h_{cone} is the height of the cone from the apex to the corner. H is the vertical distance from the apex to the center of the liquid–vapor interface, R is the radius of curvature of the liquid–vapor interface, and θ is the contact angle of the interface with the solid, measured through the liquid phase.

The roughness is in the shape of a finite conical pit, with limited cone opening width w and half cone apex angle of β. Although in reality systems are at least partially open (for example liquid is exposed to some air on top), the system can reasonably be considered closed because the height of the liquid above the roughness is much larger than the roughness and bubble size. With the assumption of a closed system, the total numbers of moles of any component in the system (n_i) are constant. We consider the liquid phase and the vapor phase to be a binary solution of water (H_2O), component 1, and a dissolved gas such as nitrogen (N_2), component 2. The solid is assumed to be nonvolatile, nondissolving and rigid; therefore knowing the equilibrium contact angle, θ, between the liquid–vapor interface and the solid,

along with the geometry parameters of the solid, fully specifies the solid in our study. Under the given constraints, the independent variables of the system that must be specified are therefore T, P^L, n_1 and n_2, w, β, and θ, where T is the temperature of the system and P^L is the pressure of the liquid phase. Instead of n_1 and n_2 (which are the total numbers of moles of component i, and are equal to the numbers of moles of component i in the initial liquid phase), one may define either of n_1 or n_2 and f_{init}, the initial degree of saturation in the liquid phase at the initial condition (before bubble formation).

Depending on the solid material and cone apex angle, a bubble may form with a convex or concave meniscus while inside the cone. The conventional method categorizes the surface as hydrophilic when $\theta < 90°$ or hydrophobic when $\theta > 90°$. For the liquid–vapor interface in geometries such as a cone, it is more helpful to define the concave-to-convex transition contact angle, θ_t, as introduced in our previous work.[72,73,85] For the case of vapor formation out of a liquid phase, the concave-to-convex transition contact angle is:[72,73,85]

$$\theta_t = \beta + 90° \tag{28}$$

where β is half of the cone apex angle, and the contact angle is measured through the liquid phase (denser phase according to convention). If the cone apex angle (2β) is fixed, then the meniscus shape inside the cone is determined by the contact angle that is imposed by the solid material:

$$\begin{cases} \theta < \beta + 90° & \rightarrow \text{ bubble with a convex meniscus inside cone} \\ \theta > \beta + 90° & \rightarrow \text{ bubble with a concave meniscus inside cone} \end{cases} \tag{29}$$

In the case where the solid material and the contact angle are fixed (hence θ is known), the set of cone apex angles (2β) that result in concave or convex meniscus should match the following criteria:

$$\begin{cases} \beta > \theta - 90° & \rightarrow \text{ bubble with a convex meniscus inside cone} \\ \beta < \theta - 90° & \rightarrow \text{ bubble with a concave meniscus inside cone} \end{cases} \tag{30}$$

Based on geometry relations and the definition of the concave-to-convex transition contact angle, we agree with Jones *et al.*[33] that the critical cone angle, $2\beta_C$, for initiation of dewetting is $2\theta - 180°$, and that spontaneous dewetting with a concave meniscus may begin only if $\beta < \theta - 90°$. Yet, we disagree with their assertion that hydrophilic conical pores with $\theta < 90°$ will never dewet for a nonzero cone angle, and to support our disagreement we refer to the case investigated by Ward *et al.*[21] where a bubble formed with contact angle of $10°$ and a convex meniscus in a cone with apex angle of $90°$ ($\beta = 45°$). Bubble formation starting with a convex meniscus is possible from a geometric point of view; however, to determine whether the bubble can be in any equilibrium condition (unstable, metastable or stable), further analysis of free energy and equilibrium radius is required. Thermodynamic stability analysis consists of three steps:[21,84] (*i*) finding the conditions for equilibrium, (*ii*) defining the appropriate free energy (thermodynamic potential) of the system with respect to some reference point, and (*iii*) analysis of the stability of the system for different potential sizes of the new phase. In the following sections we discuss the required equations and steps for thermodynamic stability analysis.

3.3.2. Conditions for equilibrium

When a composite system evolves to equilibrium, the extensive parameters take on values that extremize the entropy (S) of the system and reservoir subject to the constraints of the system. The system of interest here is composed of subsystems that include three phases: solid, liquid, and vapor, and three interfaces: solid–vapor, solid–liquid and liquid–vapor. Therefore at equilibrium:[21,86]

$$\mathrm{d}S^R + \mathrm{d}S^S + \mathrm{d}S^L + \mathrm{d}S^V + \mathrm{d}S^{SL} + \mathrm{d}S^{SV} + \mathrm{d}S^{LV} = 0 \qquad (31)$$

where superscripts denote the phase or the interface: R for the reservoir, S for the solid phase, L for the liquid phase, V for the vapor phase, SV for the solid–vapor interface, SL for the solid–liquid interface, and LV for the liquid–vapor interface. The entropy terms in Equation

(31) must be replaced by the differential form of the Euler equation.[1,86] The differential form of the Euler relation for any bulk phase is:[1,86]

$$\mathrm{d}S^b = \frac{1}{T^b}\,\mathrm{d}U^b - \frac{P^b}{T^b}\mathrm{d}V^b + \frac{1}{T^b}\sum_i \mu_i^b\,\mathrm{d}n_i^b \tag{32}$$

where superscript b denotes any arbitrary bulk phase, U is the internal energy, V is the volume of the phase, and μ_i is the chemical potential of component i, and the sum is over all components present in that phase.

The differential form of the Euler relation for an interface is:[1,86]

$$\mathrm{d}S^{ab} = \frac{1}{T^{ab}}\mathrm{d}U^{ab} + \frac{\gamma^{ab}}{T^{ab}}\mathrm{d}A^{ab} + \frac{1}{T^{ab}}\sum_i \mu_i^{ab}\,\mathrm{d}n_i^{ab} \tag{33}$$

where superscript ab denotes interface ab, γ is the surface tension, and A is the surface area of the interface ab.

The next step is to impose the constraints of the system, based on the definition of the system in the previous section, on Equations (32) and (33) substituted into Equation (31).

The system can exchange energy with the reservoir, and the system and reservoir together are isolated, hence:

$$\mathrm{d}U^R + \mathrm{d}U^S + \mathrm{d}U^L + \mathrm{d}U^V + \mathrm{d}U^{SL} + \mathrm{d}U^{SV} + \mathrm{d}U^{LV} = 0 \tag{34}$$

The system can exchange volume with the reservoir to maintain constant liquid phase pressure as shown by a movable piston in Figure 8. Also, the solid is considered to be rigid and incompressible ($\mathrm{d}V^S = 0$). Therefore, for volume exchange we have:

$$\mathrm{d}V^R + \mathrm{d}V^L + \mathrm{d}V^V = 0 \tag{35}$$

We assume, according to the "Gibbs diving surface" approach for flat surfaces,[1] that the solid–liquid and solid–vapor interfaces are located such that there is no excess of the

component of the solid phase at each of the interfaces. Therefore, only components 1 and 2 are present at the solid–liquid and solid–vapor interfaces. For the curved liquid–vapor interface, both components 1 and 2 can be in excess in the interface, because the interface is located such that the surface tension is independent of the curvature, according to the "Gibbs surface of tension" approximation.[1] The system is closed to mass transfer with the reservoir, and for mole exchange we have:

$$\mathrm{d}n_i^L + \mathrm{d}n_i^V + \mathrm{d}n_i^{SL} + \mathrm{d}n_i^{SV} + \mathrm{d}n_i^{LV} = 0 \quad i = 1{,}2 \text{ (components in fluid phases)} \tag{36}$$

$$\mathrm{d}n_j^S = 0 \quad j = \text{component of the solid phase} \tag{37}$$

$$\mathrm{d}n_k^R = 0 \quad k = \text{any component in the reservoir} \tag{38}$$

When Equations (32) and (33), along with constraints (34) to (38), and appropriate geometry equations for volume of the new phase and relevant surface areas, are substituted into Equation (31), like terms collected and the resulting equation required to be true for any arbitrary variation about equilibrium, the conditions for equilibrium are found to be:[21,84]

$$T^R = T^S = T^L = T^V = T^{SL} = T^{SV} = T^{LV} = T \tag{39}$$

$$\mu_i^L = \mu_i^V = \mu_i^{SL} = \mu_i^{SV} = \mu_i^{LV} \quad i = 1{,}2 \text{ (components in fluid phases)} \tag{40}$$

$$\gamma^{SV} - \gamma^{SL} = \gamma^{LV}\cos\theta_C \tag{41}$$

$$P^V - P^L = \frac{2\gamma^{LV}}{R_C} \tag{42}$$

$$P^L = P^R \tag{43}$$

θ_C is the equilibrium contact angle of the fluid interface with the solid phase measured through the liquid phase, and R_c is the inverse of the mean curvature of the liquid–vapor interface at equilibrium, called the Kelvin radius (note that mean curvature, κ, is defined as $\kappa = \frac{1}{2}\left(\frac{1}{R_1} + \frac{1}{R_2}\right)$ where R_1 and R_2 are principal radii of curvature). Conditions for equilibrium consist of thermal equilibrium (Equation (39)), chemical equilibrium (Equation (40)) and

mechanical equilibrium (Equations (41) to (43)). Equation (41) is the well-known Young equation and Equation (42) is the famous Young–Laplace equation. To obtain Equations (41) and (42), volume and areas in Equations (32) and (33) were expressed in terms of radius and contact angle.

In cases where the interface is part of a spherical cap, such as this case of an interface inside a conical pit, the two principal radii of curvature are equal. Therefore, at equilibrium the radius of curvature is equal to the Kelvin radius. According to the sign choice in the expression of the pressure difference in Equation(42), radius has a positive sign if the center of the radius is in the vapor phase and the meniscus is convex, and radius has a negative sign if the center is in the liquid phase and the meniscus is concave.

Equality of the chemical potentials of component i between liquid and vapor phases (according to Equation (40)) gives further information for the partial pressure of each of component 1 and 2 in the vapor phase. For the chemical potential of component i in the liquid phase, it is assumed that the liquid is incompressible and component 2 dissolved in water forms a dilute solution and therefore Henry's law is applicable.[21] For the expression of chemical potential of component i in the vapor phase it is assumed that the vapor forms an ideal gas.[21] These assumptions combined with Equation (40) give:[21]

$$P_1^V = P_{1,\infty} \exp\left[\frac{v_1^{0L}}{R_U T}\left(P^L - P_{1,\infty}\right) - \frac{n_2^L}{n_1^L}\right] \tag{44}$$

$$P_2^V = P^L \, n_2^L / n_{2s}^L \tag{45}$$

where P_i^V is the partial pressure of component i in the vapor phase, v_1^{0L} and $P_{1,\infty}$ are the specific volume and saturation pressure of pure component 1, respectively, R_U is the universal gas constant, n_i^L is the number of moles of component i in the liquid phase, and n_{2s}^L is the number of moles of component 2 (solute) in the liquid phase at the saturation limit across a flat interface and is obtained from Henry's law:[21]

$$n_{2s}^{L} = n_1^L P^L / K_H \tag{46}$$

with K_H denoting the Henry's law constant.

The vapor phase pressure is the summation of the partial pressures of component 1 and 2. By combining Equations (44) to (46), with Equation (42), the Kelvin radius is obtained as:[21]

$$R_C = \frac{2\gamma^{LV}}{\eta P_{1,\infty} + P^L(n_2^L/n_{2s}^L) - P^L} \tag{47}$$

where η is the coefficient of $P_{1,\infty}$ in Equation (44) for calculation of partial pressure of component 1 in vapor (P_1^V) that corrects the vapor pressure of component 1 for the effect of dissolved solute (component 2) and the pressure difference of the liquid and vapor phases:[21]

$$\eta = \exp\left[\frac{v_1^{0L}}{R_U T}\left(P^L - P_{1,\infty}\right) - \frac{n_2^L}{n_1^L}\right] \tag{48}$$

For n_i^L, we assume that the adsorption of component i at the interfaces is negligible compared to the total mass of i, and that the number of moles of i in the vapor phase is calculated from the ideal gas law. Therefore:[21]

$$n_1^L = n_1 - \frac{P_1^V V^V}{R_U T} \tag{49}$$

$$n_2^L = n_2 - \frac{P_2^V V^V}{R_U T} \tag{50}$$

where V^V is the volume of the vapor phase.

Substituting Equation (44) in Equation (49) and Equations (45) and (46) in Equation (50) to calculate $\frac{n_2^L}{n_1^L}$, and combining with Equation (48) for η we have:

$$\eta = \exp\left[\frac{v_1^{0L}}{R_U T}\left(P^L - P_{1,\infty}\right) - \frac{n_2 R_U T}{n_1 R_U T + V^V\left(K_H - \eta P_{1,\infty}\right)}\right] \tag{51}$$

For an arbitrary size that a bubble can take, V^V is calculated and Equation (51) must be solved to determine the value of η. For the conditions we considered, η is close to unity.

The Kelvin radius can be expressed in terms of the independent variables of the system (T, P^L, n_1, n_2, w, β, θ, and R, where w, β, θ, and R apprear in V^V) by substituting Equation (44) in Equation (49) and Equations (45) and (46) in Equation (50) for $n_1^L$and n_2^L, that are then replaced in Equation (47) yielding:[21,84]

$$R_C = \frac{2\gamma^{LV}\left(n_1 R_U T - \eta P_{1,\infty} V^V + V^V K_H\right)}{\left(\eta P_{1,\infty} - P^L\right)\left(n_1 R_U T - \eta P_{1,\infty} V^V + V^V K_H\right) + K_H n_2 R_U T} \tag{52}$$

For the case of pure vapor and liquid phases, Equation (52) simplifies to the Kelvin equation for the pure case, as also derived in our previous article:[72,73]

$$R_C = \frac{2\gamma^{LV}}{P_{1,\infty}\exp\left(\frac{v_1^{0L}}{R_U T}\left(P^L - P_{1,\infty}\right)\right) - P^L} \tag{53}$$

It should be noted that the sign convention is different from our previous work,[72,73] as we defined the pressure difference $P^V - P^L$ to correspond to a positive radius of curvature here.[72,73] As can be seen from Equation (53), for the case of pure phases, the size and concavity (sign) of the Kelvin radius is determined once the temperature and pressure of the reservoir are fixed, as also discussed in our previous paper.[73] (For pure vapor phase formation with a convex meniscus, there was a sign error in Equation (31) of one of our papers.[72] For the correct form refer to Equation (5) of our other paper.[73]) Here where phases are not pure, the Kelvin radius depends also on the initial values of n_1 and n_2,the limit of solubility of component 2 in the solvent, expressed by K_H, and the geometry of the system determining the volume of the vapor phase V^V.

3.3.3. Free energy of the system

Free energy, also called thermodynamic potential, of the system can be calculated from the second law of thermodynamics, where entropy of the system and reservoir must increase for any spontaneous changes toward equilibrium ($\Delta S_{\text{reservoir}} + \Delta S_{\text{system}} \geq 0$), and remains constant at equilibrium. With the constraints of the system combined with the second law, the free energy of this system is found to be:[21]

$$B = G^L + F^V + F^{LV} + F^{SL} + F^{SV} + P^L V^V \tag{54}$$

which is a combination of Gibbs free energy, G, of the liquid phase, Helmholtz free energy, F, of the vapor phase and the interfaces, and a $P^L V^V$ term. Energy can be evaluated with respect to a reference state. A convenient reference choice (B_0) is the state where no bubble has formed yet. The equation to calculate free energy with respect to the reference state is therefore:[21]

$$\begin{aligned} B - B_0 = {} & \frac{-2\gamma^{LV} V^V}{R_C} + \gamma^{LV}(A^{LV} + A^{SV}\cos\theta) \\ & + \frac{n_2 R_U T V^V (K_H - \eta P_\infty)}{n_1 R_U T - \eta P_\infty V^V + V^V K_H} + n_2 R_U T \ln\left(\frac{n_1 R_U T}{n_1 R_U T - \eta P_\infty V^V + V^V K_H}\right) \end{aligned} \tag{55}$$

The first term in Equation (55) is the Laplace contribution to the free energy, and is denoted in this work by $\Delta B_{\text{Laplace}}$, the second term is the surface contribution and is denoted by $\Delta B_{\text{Surface}}$, and the sum of the last two terms is the contribution of the chemical potential changes, and is denoted by $\Delta B_{\text{Chemical potential}}$. Later on in our plots, the contributions of each term in the total free energy will be discussed. Comparing the contribution of each term in the free energy can yield physical insight into the controlling phenomena.[71]

With the expression of volume and interfacial areas, the free energy $B - B_0$ (also called ΔB) in Equation (55) and the equilibrium (Kelvin) radius, R_C in Equation (52) can both be expressed in terms of T, P^L, n_1 and n_2, w, β, θ_C, θ, and R over the range of R. Either of n_1 or n_2 can be replaced by setting the initial degree of saturation, f_{init}, of the solution before any

vapor formation. The initial degree of saturation is the ratio of the number moles of solute in the liquid phase to the number of moles of solute that would saturate the liquid phase with a flat interface. At the initial condition with no vapor formation yet, the total number of moles of component i in the system is equal to the total number of moles of component i in the liquid phase, $n_i = n_i^L$. The initial degree of saturation of the initial liquid phase is therefore:

$$f_{\text{init}} = \frac{n_2 K_H}{n_1 P^L} \tag{56}$$

3.3.4. Geometry equations for a bubble in a finite cone

The equations for volume and areas vary based on the concavity of the bubble inside the cone. Figure 9 demonstrates the possible configurations when contact angle and cone apex angle are such that the bubble starts with a convex meniscus OR a concave meniscus inside the cone.

Bubble starting with a convex meniscus ($\theta < \beta + 90°$) in a finite cone

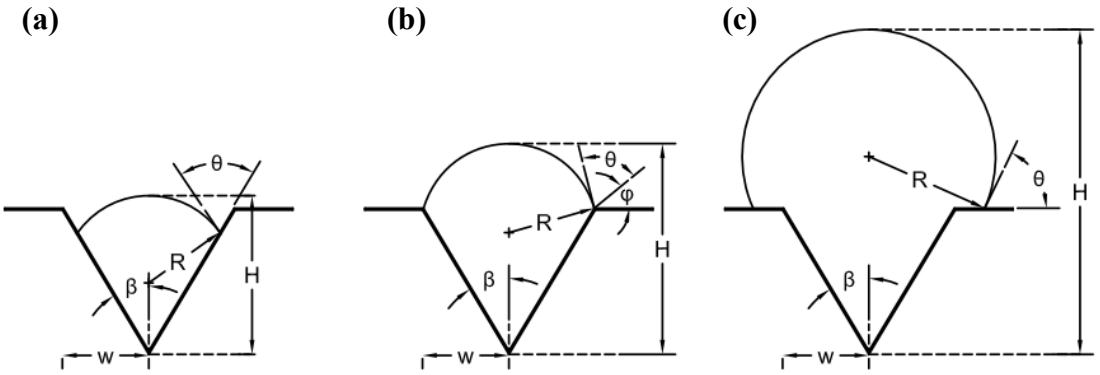

Bubble starting with a concave meniscus ($\theta > \beta + 90°$) in a finite cone

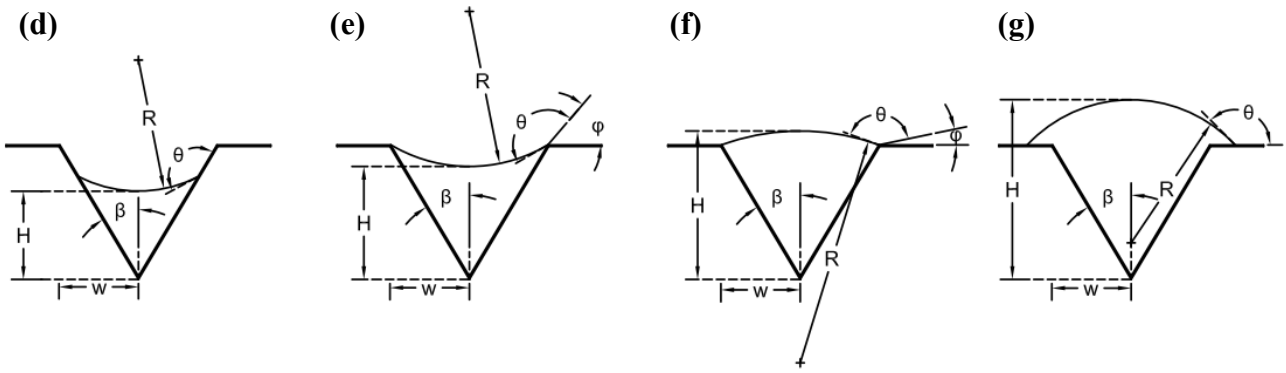

Figure 9. Vapor in a finite cone starting with a convex meniscus (a, b, c) OR starting with a concave meniscus (d, e, f, g). φ is the angle that describes the rotation of the interface while it is pinned. For a bubble starting with a convex meniscus, as the bubble grows it may take one of these configurations: (a) inside the cone with a convex meniscus, (b) pinned to the corner of the cone with a convex meniscus, or (c) out of the cone with a convex meniscus. For a bubble starting with a concave meniscus, as the bubble grows it may take one of these configurations (d) inside the cone with a concave meniscus, (e) pinned to the corner of the cone with a concave meniscus, (f) pinned to the corner of the cone with a convex meniscus, or (g) out of the cone with a convex meniscus.

Equations for the case of vapor with a convex meniscus are presented in the article by Ward and Levart,[21] and are summarized in Table 1 .

Table 1. Geometry relations for a bubble inside a finite cone starting with a convex meniscus, $\theta < \beta + 90°$

(a) Inside the cone with a convex meniscus, R has a positive sign $R \leq \frac{w}{\cos(\theta-\beta)}$	
$H = R\left[\frac{\cos(\theta-\beta)}{\tan\beta} + 1 - \sin(\theta-\beta)\right]$	(57)
$V^V = \frac{\pi}{3}R^3\left[\frac{\cos^3(\theta-\beta)}{\tan\beta} + 2 - 3\sin(\theta-\beta) + \sin^3(\theta-\beta)\right]$	(58)
$A^{LV} = 2\pi R^2[1-\sin(\theta-\beta)]$	(59)
$A^{SV} = \frac{\pi R^2\cos^2(\theta-\beta)}{\sin\beta}$	(60)
(b) Pinned to the corner with a convex meniscus, R has a positive sign $\frac{\pi}{2} - \beta \geq \varphi \geq 0$	
$\lvert R\rvert = \frac{w}{\sin(\theta+\varphi)}$	(61)
$H = \frac{w}{\tan\beta} + R[1+\cos(\theta+\varphi)]$	(62)
$V^V = \frac{\pi}{3}\left\{\frac{w^3}{\tan\beta} + R^3[2+3\cos(\theta+\varphi) - \cos^3(\theta+\varphi)]\right\}$	(63)
$A^{LV} = 2\pi R^2[1+\cos(\theta+\varphi)]$	(64)
$A^{SV} = \frac{\pi w^2}{\sin\beta}$	(65)
(c) Out of the cone with a convex meniscus, R has a positive sign $R \geq \frac{w}{\sin\theta}$	
$H = \frac{w}{\tan\beta} + R[1+\cos\theta]$	(66)
$V^V = \frac{\pi}{3}\left[\frac{w^3}{\tan\beta} + R^3(2+3\cos\theta - \cos^3\theta)\right]$	(67)
$A^{LV} = 2\pi R^2[1+\cos\theta]$	(68)
$A^{SV} = \pi\left[\frac{w^2}{\sin\beta} + R^2\sin^2\theta - w^2\right]$	(69)

For a bubble starting with a convex meniscus, the pinning starts when $\varphi = \frac{\pi}{2} - \beta$, and ends when φ is zero, while the radius always has the same positive sign (as the interface remain convex). The liquid–vapor interface radius of curvature changes in the range of $R_{\text{pin, start}}$ and $R_{\text{pin, end}}$ where according to Equation (61), we have:

$$R_{\text{pin, start}} = \frac{w}{\sin\left(\theta + \frac{\pi}{2} - \beta\right)} \tag{70}$$

$$R_{\text{pin, end}} = \frac{w}{\sin(\theta)} \tag{71}$$

The two values of $R_{\text{pin, start}}$ and $R_{\text{pin, end}}$ become equal when $\theta = \frac{\pi}{4} + \frac{\beta}{2}$. Therefore depending on the values of θ and β, the radius of curvature of the liquid–vapor interface may increase or decrease during pinning as the rotation angle φ changes from $\frac{\pi}{2} - \beta$ to 0. It is the most convenient to define the pinning range by letting the rotation angle φ change from $\frac{\pi}{2} - \beta$ to 0, and then calculate radius as a function of the rotation angle. (Figure A-1 in the appendix shows changes of the radius of curvature when the interface is pinned as the rotation angle changes for various contact angles in the case of a bubble starting with a convex meniscus).

It should be noted that in the case of a bubble starting with a convex meniscus, there are some cases where H (the vertical distance from the apex to the center of the liquid–vapor interface) is greater than h_{cone}, yet the bubble is still considered inside because the vertical height of contact of the bubble with the solid from the cone apex, h, is still less than h_{cone}.

The geometry equations for the case of a bubble starting with a concave meniscus are presented in Table 2.

Table 2. Geometry relations for a bubble inside a finite cone starting with a concave meniscus, $\theta > \beta + 90°$

(d) Inside the cone with a concave meniscus, R has a negative sign $\lvert R\rvert \leq \frac{-w}{\cos(\theta-\beta)}$	
$H = R\left[\frac{\cos(\theta-\beta)}{\tan\beta} + 1 - \sin(\theta-\beta)\right]$	(57)
$V^V = \frac{\pi}{3}R^3\left[\frac{\cos^3(\theta-\beta)}{\tan\beta} + 2 - 3\sin(\theta-\beta) + \sin^3(\theta-\beta)\right]$	(58)
$A^{LV} = 2\pi R^2[1-\sin(\theta-\beta)]$	(59)
$A^{SV} = \frac{\pi R^2\cos^2(\theta-\beta)}{\sin\beta}$	(60)
Pinned to the corner with a (e) concave meniscus, R has a negative sign, $\frac{\pi}{2} - \beta \geq \varphi \geq \pi - \theta$ OR (f) convex meniscus, R has a positive sign, $\pi - \theta \geq \varphi \geq 0$	
$\lvert R\rvert = \frac{w}{\sin(\theta+\varphi)}$	(61)
$H = \frac{w}{\tan\beta} + R[1+\cos(\theta+\varphi)]$	(62)
$V^V = \frac{\pi}{3}\left\{\frac{w^3}{\tan\beta} + R^3[2+3\cos(\theta+\varphi) - \cos^3(\theta+\varphi)]\right\}$	(63)
$A^{LV} = 2\pi R^2[1+\cos(\theta+\varphi)]$	(64)
$A^{SV} = \frac{\pi w^2}{\sin\beta}$	(65)
(g) Out of the cone with a convex meniscus, R has a positive sign, $R \geq \frac{w}{\sin\theta}$	
$H = \frac{w}{\tan\beta} + R[1+\cos\theta]$	(66)
$V^V = \frac{\pi}{3}\left[\frac{w^3}{\tan\beta} + R^3(2+3\cos\theta - \cos^3\theta)\right]$	(67)
$A^{LV} = 2\pi R^2[1+\cos\theta]$	(68)
$A^{SV} = \pi\left[\frac{w^2}{\sin\beta} + R^2\sin^2\theta - w^2\right]$	(69)

As presented in Table 2, for a bubble starting with a concave meniscus in the cone, the pinning starts when the bubble touches the corners of the cone, and the rotation angle is $\frac{\pi}{2} - \beta$. Further growth happens as the rotation angle decreases, and the absolute radius of curvature of the liquid–vapor interface increases toward infinity for a flat interface (note that in the case of a concave meniscus, radius has a negative sign according to our definition in this work). At a rotation angle of $\pi - \theta$, the meniscus becomes flat and the radius becomes infinity. The concavity switch happens at the rotation angle of $\pi - \theta$, and further bubble growth happens as the rotation angle decreases to zero, while the absolute radius of curvature decreases. When modeling the system in Matlab, it is not possible to give the exact rotation angle of $\pi - \theta$ and physically reach the infinite radius. Therefore, for a bubble starting with a concave meniscus, the bubble is considered to pin with a concave meniscus when rotation angle is in range of $\frac{\pi}{2} - \beta \geq \varphi \geq \pi - \theta - \varepsilon$, and to switch its concavity and pin with a convex meniscus when the rotation angle is in the range of $\pi - \theta + \varepsilon \geq \varphi \geq 0$. In cases where the bubble at equilibrium is pinned with a rotation angle close to $\pi - \theta$ (where the meniscus concavity switches from concave to convex), ε must be adequately small to allow including large absolute values of radius (compared to the cone mouth radius) that result in the equilibrium state. Correct selection of ε is especially important for cases where the cone mouth radius is much smaller than the range for the Kelvin radius, as presented in Appendix A-2.

According to Table 1 and Table 2, the vapor volume and surface areas are expressed in terms of contact angle, θ, size of the bubble, R, and the cone geometric parameters, that is half of the cone angle, β, and cone opening width, w.

3.3.5. Step by step stability analysis

The steps for thermodynamic stability analysis are as follows:

i) Specify the independent variables: T, P^L, n_1 and n_2 (or n_i and f_{init}), w, β, and θ (equal to θ_C).

ii) Find physical properties, $P_{1,\infty}$, v_1^{0L}, K_H , and γ^{LV} of the specified system from handbooks.

iii) Consider the range for geometry radius of curvature of the interface, R.

iv) Calculate V^V, A^{SV}, and A^{LV} for each R.

v) Calculate η from Equation (51) for each R.

vi) Calculate R_C from Equation (52) for each R.

vii) Find equilibrium states from the intersection of the R_C versus R curve with the R versus R line. At equilibrium, the geometry radius must be equal to the equilibrium (Kelvin) radius. Alternatively, the equilibrium radius can be found from the intersection of the curve of R_C versus H (or versus V^V) with the curve of R versus H (or versus V^V). Plotting R_C and R versus H or V^V is particularly more convenient compared to plotting versus R, in cases where the radius of a pinned bubble decreases and increases again, while the bubble grows constantly (such as the case described in Appendix A-3) or where the sign of radius changes, as a result of a change in concavity of the interface (for cases where the bubble starts with a concave meniscus inside the cone, gets pinned to the corner with a concave meniscus, switches the concavity to convex while it is pinned, and grows out of the cone with a convex meniscus). It should be noted that in all such cases, H and V^V are constantly increasing over the growth range.

viii) Calculate free energy from Equation (55) over the range of sizes of the bubble.

ix) Plot free energy of the system versus size of the bubble (R or H or V^V). The extremum points in the plot correspond to the equilibrium states: a maximum in the free energy corresponds to an unstable equilibrium state, a local minimum in the free energy corresponds to a metastable equilibrium state, and a global minimum in the free energy corresponds to a stable equilibrium state. It should be noted that a minimum in free energy corresponds to a maximum in entropy of the system subject to its constraints. The size of the bubble at the equilibrium state from this method should match the results from step (*vii*).

3.4. Results and discussion

In this section we present the results for the number and nature of equilibrium states, as well as the size of the vapor phase at the equilibrium states, for two cases of (1) vapor starting with a convex meniscus or (2) vapor starting with a concave meniscus inside a finite cone submerged in a liquid solution at constant temperature and liquid pressure. We discuss the effects of cone apex angle, cone width or height, contact angle, total numbers of moles, and initial degree of saturation on stability in each case. For the system of interest in this study, temperature is set at 25 ℃ and the liquid pressure at 1 atm. Fluid phases are considered to be made of water and nitrogen. At a temperature of 25 ℃, the saturation pressure of pure water, $P_{1,\infty}$, is 3.17× 10^3 Pa, and the specific volume of pure water, v_1^{0L}, is 18.07 cm^3/mol. The liquid–vapor surface tension, γ^{LV}, is considered to have the same value as the liquid–vapor surface tension of pure water, 72.06 mN/m, assuming negligible concentration effect on the liquid–vapor surface tension for the concentration range in this problem.[87] The Henry's law constant K_H, for describing the saturation limit across a flat interface for the water/nitrogen system is 9.1×10^4 atm.[76]

3.4.1. Binary bubble starting with a convex meniscus in a finite cone

For vapor starting with a convex meniscus, we chose the same values as Ward and Levart[21] for the independent variables of the system. We considered one conical pit, hence one bubble, and the numbers of moles of the solvent (water) and the solute (nitrogen) are set to the same per-bubble values as were used by Ward and Levart,[21] that is 2.5×10^{19} molecules (4.15×10^{-5} moles) of water and 3×10^{14} molecules (4.98×10^{-10} moles) of nitrogen.[21] The initial liquid is therefore slightly supersaturated, with an initial degree of saturation of 1.089 according to Equation (56). The mouth radius, w, of the cone is 50 μm, and the half cone apex angle, β, is 45°. The contact angle, θ, is considered to be 10°. The equilibrium states are analyzed both with the method of intersection of the Kelvin radius with the geometry radius, and from the free energy diagram, as shown in Figure 10.

(a)

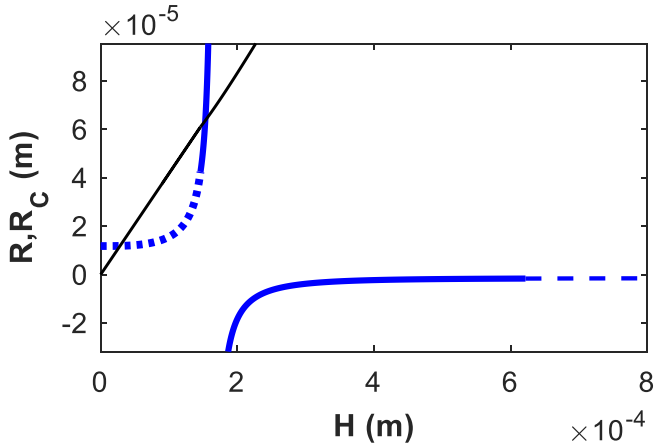
×10^-5
8
6
4
2
0
-2
R,R_C (m)
0
2
4
6
8
H (m)
×10^-4

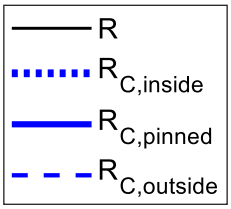
R
R_C,inside
R_C,pinned
R_C,outside

(b)

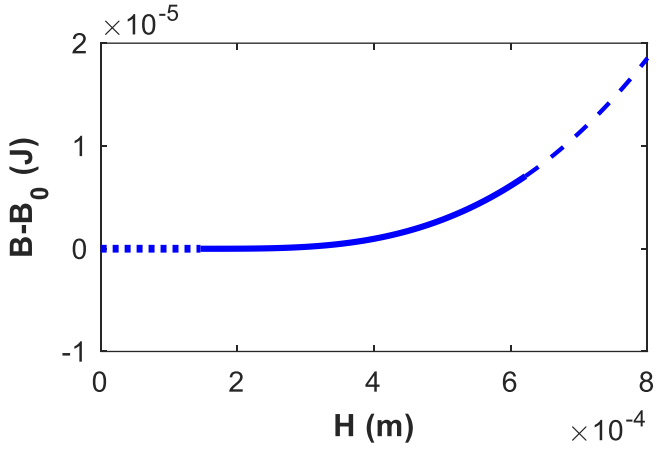
×10^-5
2
1
0
-1
B-B_0 (J)
0
2
4
6
8
H (m)
×10^-4

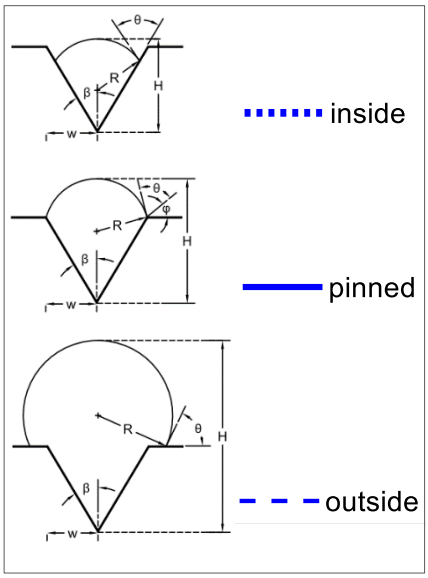
θ
R
H
β
w
inside
φ
pinned
outside

(c)

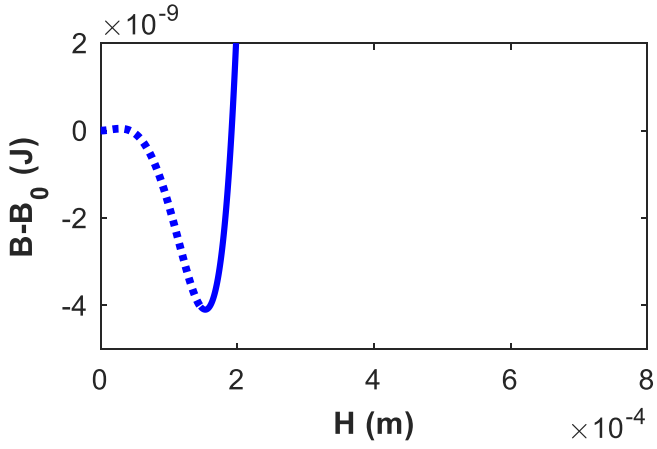
×10^-9
2
0
-2
-4
B-B_0 (J)
0
2
4
6
8
H (m)
×10^-4

Figure 10. Equilibrium states of a bubble starting with a convex meniscus in a finite cone submerged in a liquid solution, (a) intersection of the Kelvin radius with the geometry radius versus height of the center of the liquid–vapor interface, (b) free energy versus height of the center of the liquid–vapor interface, (c) magnification of the energy axis for free energy versus height of the center of the liquid–vapor interface, to show the maximum and minimum point. The system is set to be at 25 ℃ and a liquid pressure of 1 atm, with the liquid initially containing 2.5×10^{19} molecules (4.15×10^{-5} moles) of water and 3×10^{14} molecules (4.98×10^{-10} moles) of nitrogen (initial degree of saturation of 1.089). The cone mouth radius, w, is 50 μm, and the half cone apex angle, β, is 45°. The contact angle, θ, is considered to be 10°. The status of the bubble (inside or pinned to the corner, or outside the cone) is shown with different line types.

Figure 10 shows that for this system of interest, the system has two equilibrium states: The system passes an unstable equilibrium state (energy barrier), then moves to the stable equilibrium and stays there. The unstable equilibrium occurs while the bubble is still inside the cone with a convex meniscus. The stable equilibrium is formed with the bubble pinned to the corner of the cone with a convex meniscus. In Figure 10 (a) the negative values of the Kelvin radius result from the pressure in the vapor becoming lower than the pressure in the liquid as the size of the bubble increases. With the convention of the pressure difference being defined as $P^V - P^L$, only a positive radius can result in the convex meniscus (to satisfy the set value for contact angle). Therefore such negative values of Kelvin radius have no physical meaning, which is also indicated by there being no intersection with the geometry radius (line R versus H). Figure 10 (b) shows the free energy of the system over the entire growth path. Figure 10 (c) zooms in on smaller values of free energy to reveal the maximum and minimum points of the graph. Our results are in agreement with the results of Ward and Levart,[21] where the liquid–gas interface height was found to be 2.8×10^{-5} m at the unstable equilibrium state, and 1.5×10^{-4} m at the stable equilibrium state. For the condition of interest of this system, the value of η from Equation (51) is always very close to 1 as mentioned before. For this problem, the mean value of η is 1.0007, with average deviation of 3.69×10^{-6} from the mean value. Contributions of specific terms, $\Delta B_{\text{Laplace}}$, $\Delta B_{\text{Surface}}$, and $\Delta B_{\text{Chemical potential}}$ to the free energy with respect to the reference point are presented in Figure 11, according to Equation (55).

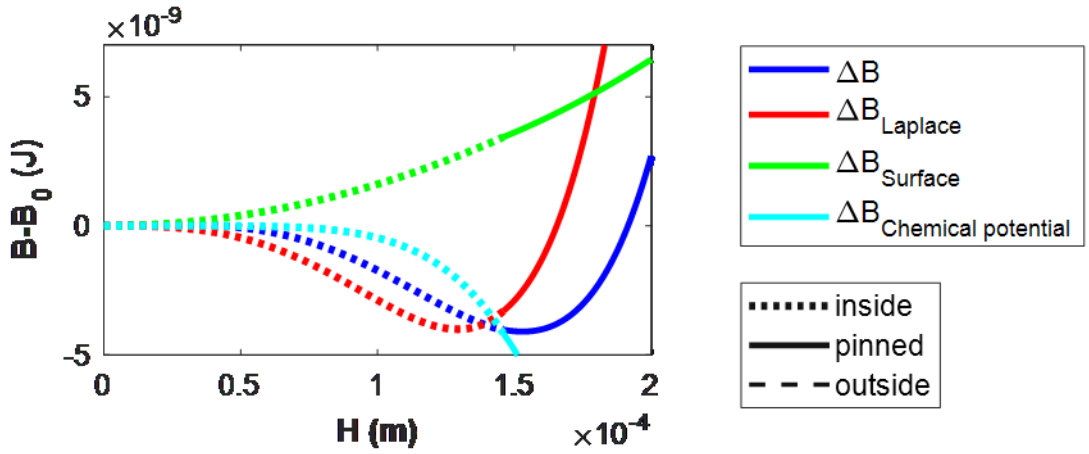

Figure 11. Contributions of the Laplace term, $\Delta B_{Laplace}$, the surface term, $\Delta B_{Surface}$, and the chemical potential term, $\Delta B_{Chemical\ potential}$, to the free energy, ΔB, of a bubble starting with a convex meniscus in a finite cone submerged in a liquid solution. The system is set to be at 25 ℃ and a liquid pressure of 1 atm, with the liquid initially containing 4.15×10^{-5} moles of water and 4.98×10^{-10} moles of nitrogen (initial degree of saturation of 1.089). The cone mouth radius, w, is 50 μm, and the half cone apex angle, β, is 45°. The contact angle, θ, is considered to be 10°. The status of the bubble (inside, pinned to the corner, or outside the cone) is shown with different line types.

As can be seen in Figure 11, the total free energy ΔB has the same trend as the Laplace term, $\Delta B_{\text{Laplace}}$. The Laplace term has a dominant effect because the size of the stable bubble is on the order of hundreds of micrometers. The changes in the surface term $\Delta B_{\text{Surface}}$ and chemical potential term $\Delta B_{\text{Chemical potential}}$ behave in opposite manners. It should however be noted that the Kelvin radius that appears in the Laplace equation accounts for the changes in the concentration of the solution as a result of changes in size of the bubble, according to Equation (52).

For this case the stable equilibrium happens for a bubble pinned to the corner of the cone (as was found in the paper by Ward and Levart[21]). However, this is not always the case, and the stable equilibrium may form inside, pinned, or outside the cone. There are cases where the amount of energy required to pass the energy barrier for bubble formation (from point 0 to the maximum point) becomes comparable to the depth of the energy well of the stable state, as presented in Figure 12.

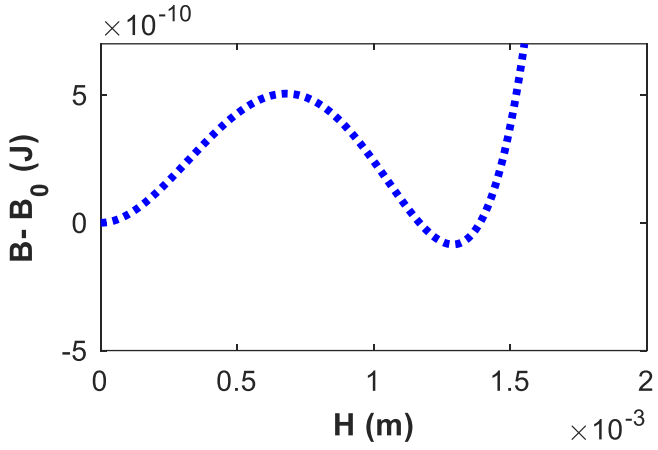

Figure 12. Special case where the height of the energy barrier is comparable to the depth of the energy well for a bubble starting with a convex meniscus in a finite cone submerged in a liquid solution. The system is set to be at 25 ℃ and a liquid pressure of 1 atm, with the liquid initially containing 4.15×10^{-5} moles of water and 4.98×10^{-10} moles of nitrogen (initial degree of saturation of 1.089). The cone mouth radius, w, is 50 μm. The cone half apex angle β is 1° and the contact angle, θ, is 25°.

When the height of the energy barrier becomes comparable to the depth of the energy well such as in Figure 12, and if the energy barrier is sufficiently small, the system may fluctuate between bubble formation and disappearance, with the density inside the cone switching between the density of the bulk liquid, and that of a vapor. We call this condition bubble "formation–disappearance fluctuation". Although for the specifications of Figure 12 this condition happens from an initially supersaturated liquid, it can happen from an initially undersaturated liquid, depending on other parameters of the system.

Next we investigated the effect of different parameters on the equilibrium states, in the following sections.

3.4.1.1. Effect of cone apex angle 2β for a bubble starting with a convex meniscus

Figure 13 shows the effect of cone apex angle on the stability of the bubble starting with a convex meniscus inside a finite cone, while the cone mouth radius, w, was kept constant.

(a) $\theta = 40°$

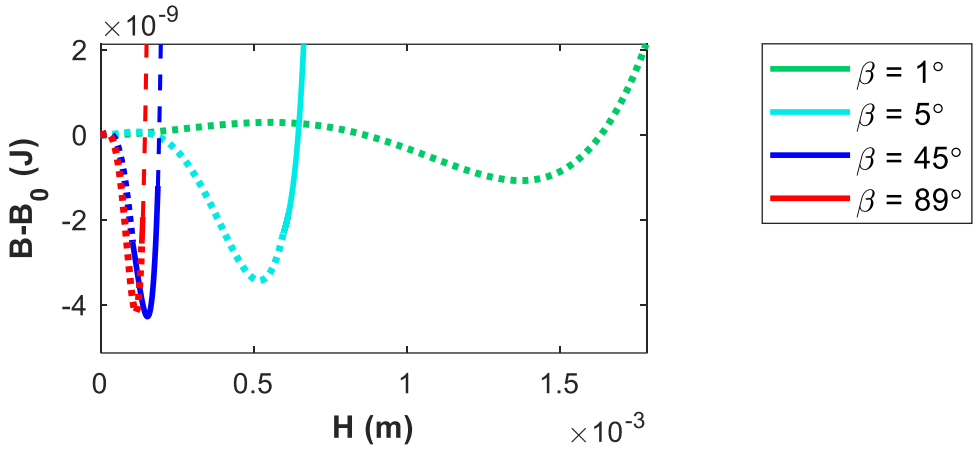

(b) $\theta = 60°$

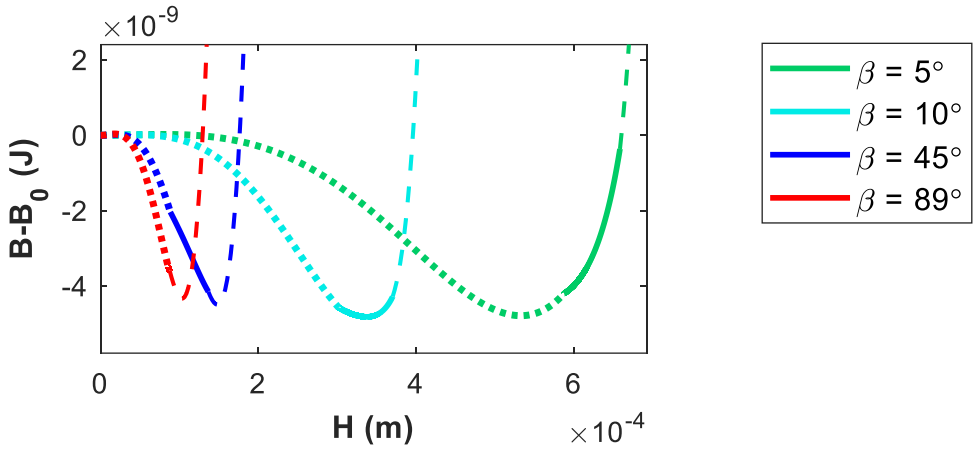

(c) $\theta = 100°$

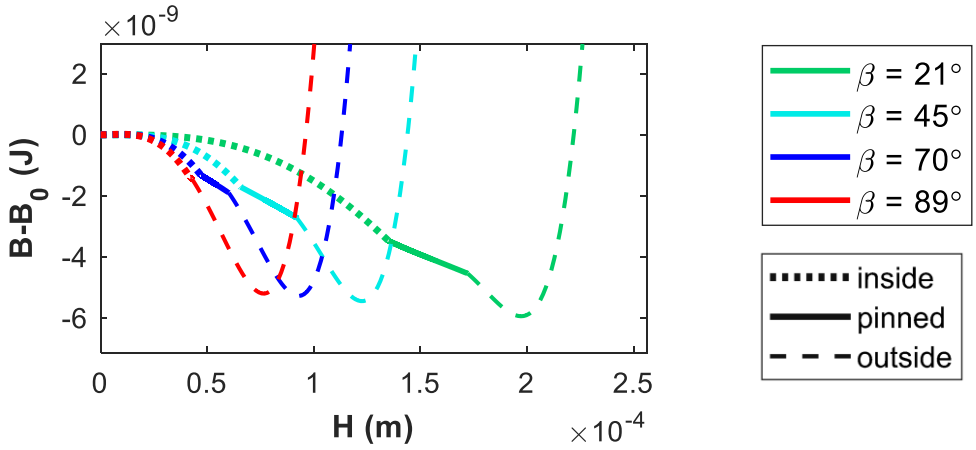

Figure 13. Effect of half cone apex angle, β, on equilibrium states of a bubble starting with a convex meniscus in a finite cone submerged in a liquid solution. The system is set to be at 25 ℃ and a liquid pressure of 1 atm, with the liquid initially containing 4.15×10^{-5} moles of water and 4.98×10^{-10} moles of nitrogen (initial degree of saturation of 1.089). The cone mouth radius, w, is 50 μm. Different trends in behavior are seen for (a) smaller values of contact angle, θ, (b) medium values of contact angle, and (c) larger values of contact angle. The status of the bubble (inside, pinned to the corner, or outside the cone) is shown with different line types.

When the cone apex angle increases, the heights of the liquid–vapor interface at the stable equilibrium point always decrease. With the cone mouth radius, w, kept constant, any increase in the cone apex angle is equivalent to a decrease in the cone height h_{cone} or cone volume. In Figure 13 with w equal to 5×10^{-5} m, the cone height changes from 2.9×10^{-3} m to 8.7×10^{-7} m as the half cone apex angle changes from 1° to 89°. The cone gets similar to the flat plate when the cone half apex angle gets close to 90°. It should be noted that there are cases where H (the vertical distance from the apex to the center of the liquid–vapor interface) is greater than h_{cone}, but the bubble is still defined as being inside the cone, as the contact point of the liquid–vapor interface with the solid is inside the cone ($h < h_{\text{cone}}$). For the meniscus to be convex, β can only change in the range that satisfies Equation (30). When $\theta \leq \frac{\pi}{2}$, any value of β automatically satisfies Equation (30), but for cases where $\theta > \frac{\pi}{2}$, a convex meniscus is possible only with certain values of β.

For cases with smaller contact angle, case (a) in Figure 13, the stable bubble forms inside the cone for smaller cone apex angle, forms pinned to the corner at intermediate cone apex angle, and further increase in the cone apex angle results in the stable bubble forming inside the cone again. For intermediate contact angles, case (b) in Figure 13, as the cone apex angle increases, the stable point shifts from being inside the cone, to being pinned, to forming outside the cone. For larger values of contact angle, case (c) in Figure 13, the stable bubble forms when the bubble is outside the cone.

In contrast to the height of the stable bubble, the trends in changes of stability, radius of curvature of the liquid–vapor interface, and volume of the stable bubble as a result of changes

in the cone half apex angle are not always monotonic, and are different based on other set values for the system such as the contact angle.

When the stable bubble is formed outside the cone, any increase in the cone half apex angle creates less stability for the stable bubble. (This was tested for contact angles of 100°, 120°, 140°, 160°, and 178° with the cone apex angle changing, while keeping the mouth radius of the cone constant. For these contact angles, over the range of β, the stable point always formed outside the cone. Also for contact angles of 60°, 80°, and 90° and over β ranges, the stable bubble was not always outside; however for values of β for which the stable bubble is outside, the same behavior is observed.) This trend for free energy is only obsrved for the stable bubble forming outside the cone. For the stable bubble that forms pinned or inside the cone, as the cone half apex angle increases, no genereal trend in the free energy was observed.

3.4.1.2. Effect of cone mouth radius w for a bubble starting with a convex meniscus

The effect of changes in cone mouth radius, w, on the stability of the bubble starting with a convex meniscus inside a finite cone is shown in Figure 14. Any increase in the cone mouth radius, is equivalent to increase in the cone height (h_{cone}), because the cone apex angle is considered to remain unchanged.

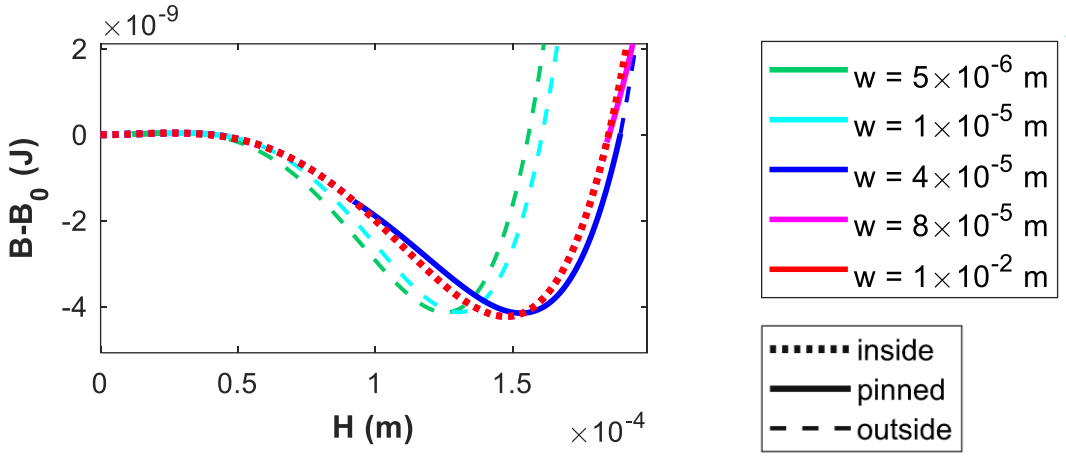

Figure 14. Effect of cone mouth radius, w, on equilibrium states of a bubble starting with a convex meniscus in a finite cone submerged in a liquid solution. The system is set to be at 25 ℃ and a liquid pressure of 1 atm, with the liquid initially containing 4.15×10^{-5} moles of water and 4.98×10^{-10} moles of nitrogen (initial degree of saturation of 1.089). The cone half apex angle, β, is 45°, and the contact angle, θ, is considered to be 30°. The status of the bubble (inside, pinned to the corner, or outside the cone) is shown with different line types.

Figure 14 shows that for larger values of the cone mouth radius (while the cone apex angle is kept constant, *i.e.*, changing conical pit size while keeping the cone aspect ratio constant), the stable equilibrium forms inside the cone. When the cone mouth radius gets smaller, the stable bubble forms pinned to the corner of the cone with less stability, and as the cone mouth radius gets further smaller, the stable bubble forms outside the cone and the stability is decreased. Note that for the last two highest values of cone mouth radius in Figure 14, where the bubble is formed inside the cone, the graphs overlap and the height and energy level of the stable point remain almost the same.

An infinite cone is the extreme case that happens as the cone mouth radius (as well as cone height) becomes infinitely large, while the cone apex angle is fixed at the defined value. For an infinite cone, bubble formation would be inside the cone (if the bubble forms), and the free energy and the values of the equilibrium states are almost the same as other cases where the bubble is formed inside the cone, presented in Figure 14.

3.4.1.3. Effect of contact angle θ for a bubble starting with a convex meniscus

The effect of contact angle on the equilibrium states is shown in Figure 15.

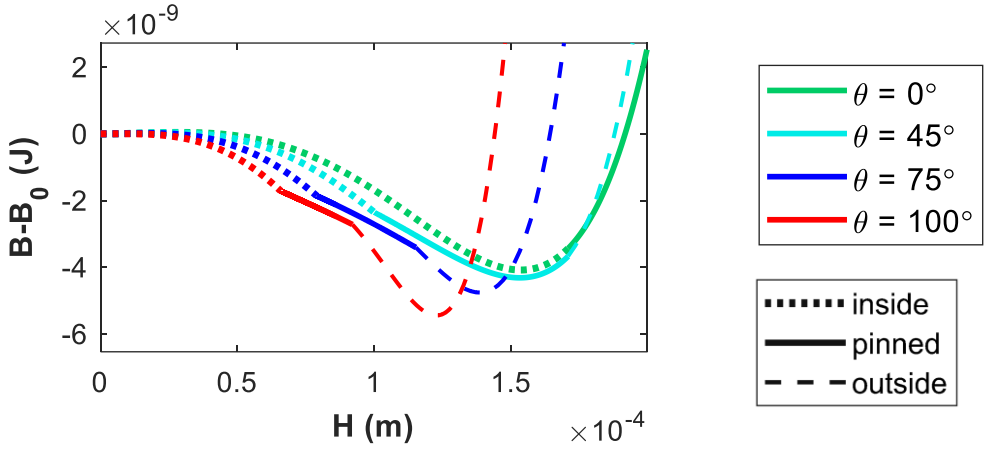

Figure 15. Effect of contact angle, θ, on equilibrium states of a bubble starting with a convex meniscus in a finite cone submerged in a liquid solution. The system is set to be at 25 ℃ and a liquid pressure of 1 atm, with the liquid initially containing 4.15×10^{-5} moles of water and 4.98×10^{-10} moles of nitrogen (initial degree of saturation of 1.089). The cone half apex angle, β, is 45°, and the cone mouth radius, w, is 50 μm. The status of the bubble (inside, pinned to the corner, or outside the cone) is shown with different line types.

As the contact angle increases (get closer the transition contact angle, θ_t), the stable equilibrium becomes more stable, with lower free energy level. In Figure 15, as the contact angle changes from 0° to 100°, the stable equilibrium becomes more stable, even though the stable equilibrium forms outside the cone for higher values of contact angle. For a smaller contact angle, the stable equilibrium forms inside the cone. As the contact angle increases, depending on the values of cone apex angle and mouth radius, the stable bubble may form pinned to the corner and finally outside the cone. Note that θ can only change in the range that is described by Equation (29), to maintain a convex meniscus.

3.4.1.4. Effect of total numbers of moles, with constant initial degree of saturation, for a bubble starting with a convex meniscus

The effect of the total numbers of moles of component 1 and 2 on the stability of the system is presented in Figure 16, while n_1 and n_2 are changed such that the initial degree of saturation (according to Equation (56)) remains the same.

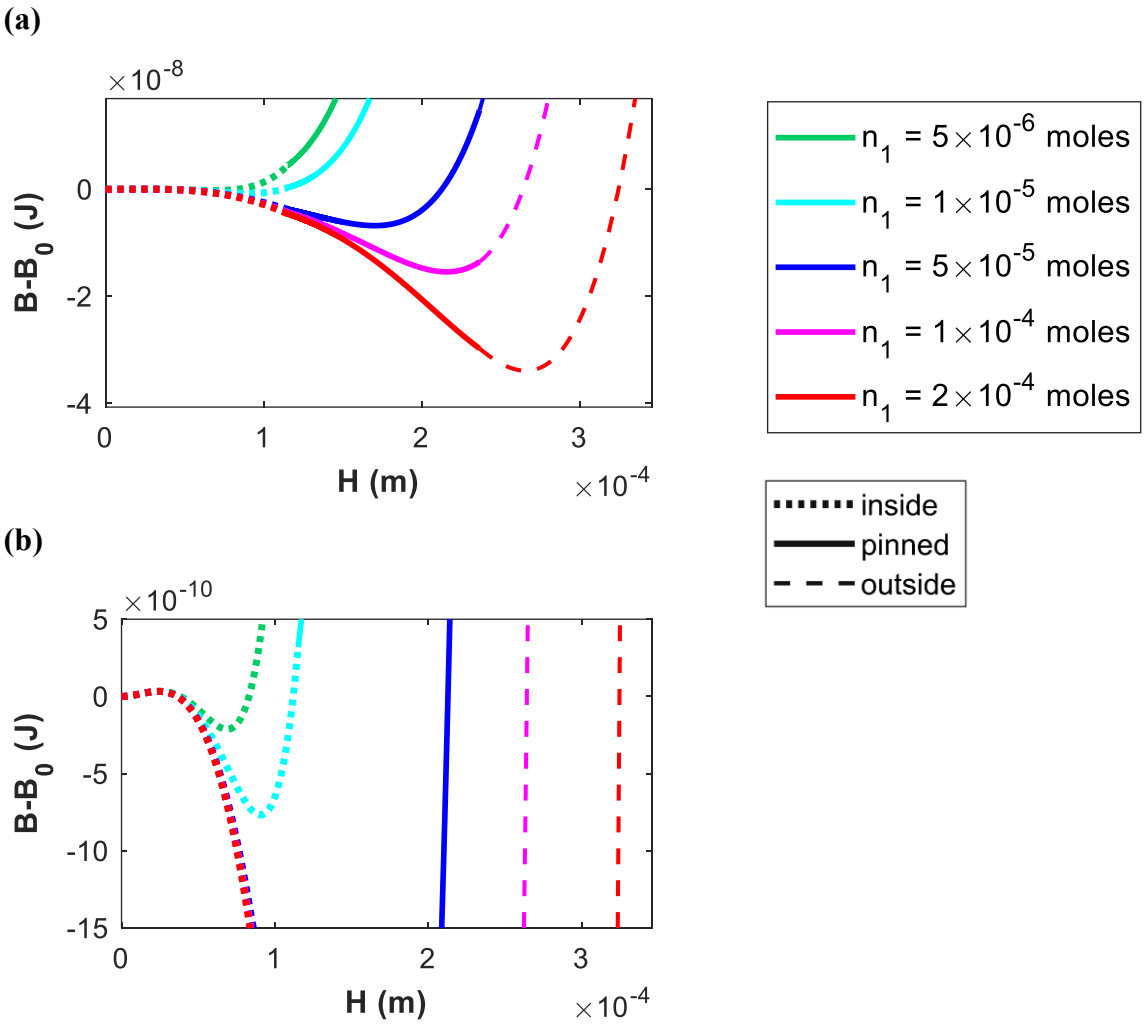

Figure 16. (a) Effect of total numbers of moles, n_1 and n_2, on the stability of a bubble starting with a convex meniscus in a finite cone submerged in a liquid solution while the initial degree of saturation remains the same (1.1) for each set of n_1 and n_2. The system is set to be at 25 ℃ and a liquid pressure of 1 atm. The cone mouth radius, w, is 50 μm, and the half cone apex angle, β, is 45°. The contact angle, θ, is considered to be 30°, (b) magnification to show the minimum points for the smaller values of n_1 and n_2. The status of the bubble (inside, pinned to the corner, or outside the cone) is shown with different line types.

As the number of moles of component 1 is increased, and number of moles of component 2 is also increased such that the initial degree of saturation remains constant (1.1 in this case), the stable point forms with a larger height and more stability (the minimum point has a larger negative energy level compared to the reference state), according to Figure 16. In Figure 16, as n_1 changes from 5×10^{-6} to 2×10^{-4} moles, n_2 changes from 6.06×10^{-11} to 2.42×10^{-9} moles, to maintain constant initial degree of saturation of 1.1 according to Equation (56). The system is initially supersaturated, and for any values of n_1 and n_2, the

system forms a stable equilibrium that corresponds to a minimum point. Figure 16 (b) zooms in on the smaller scale of energy values to show the stable equilibrium states for $n_1 = 5 \times 10^{-6}$ moles and $n_1 = 1 \times 10^{-5}$moles. Increasing the total number of moles of components, while keeping the initial degree of saturation constant, also causes the stable bubble to switch from forming inside, to forming pinned, and ultimately forming outside the cone, as larger amounts of components create a larger bubble before sufficiently depleting the solute gas in the liquid to arrive at the stable state.

In our previous paper on surface nanobubbles,[84] as well as for the bubble in a cone investigated by Ward and Levart[21], it was considered that there were multiple bubbles of the same size in the system. Hence for each bubble, the total number of moles of each component must be divided by the assumed number of bubbles (q). In this study, we chose a simpler approach and considered only one bubble, and the corresponding total numbers of moles for that single bubble. Comparing the two approaches, increasing the total number of moles of each component at constant degree of saturation in this study, is analogous to decreasing the number of bubbles (while keeping the total number of moles of each component for q bubbles the same) in the previous papers[21,84] (where higher stability and larger height of the bubble at stable equilibrium were found as the number of surface bubbles decreases).

3.4.1.5. Effect of initial degree of saturation for a bubble starting with a convex meniscus

Figure 17 shows the effect of initial degree of saturation, f_{init}, on the stability of a bubble starting with a convex meniscus in a finite cone submerged in a liquid solution, while keeping the total number of moles of component 1 (solvent) constant.

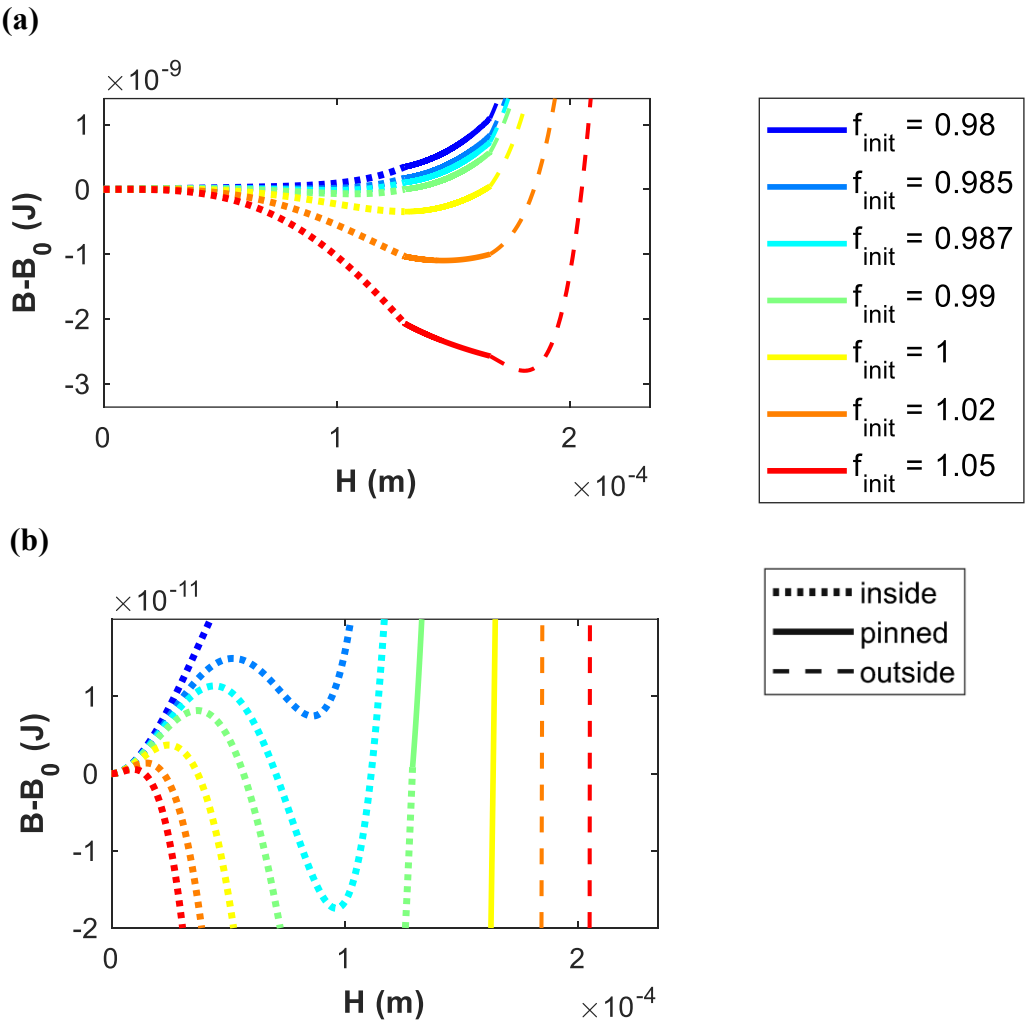

Figure 17. (a) Effect of initial degree of saturation, f_{init}, on the stability of a bubble starting with a convex meniscus in a finite cone submerged in a liquid solution at 25 °C and a liquid pressure of 1 atm, while total number of moles of component 1, n_1, is constant (5×10^{-5} moles). The cone mouth radius, w, is 50 μm, and the half cone apex angle, β, is 22°. The contact angle, θ, is considered to be 100°, (b) magnification to show the minimum points for the smaller values of f_{init}. The status of the bubble (inside, pinned to the corner, or outside the cone) is shown with different line types.

Figure 17 shows that bubble formation inside the cone is unfavorable for smaller values of initial degree of saturation. As the initial degree of saturation increases, stable bubble formation inside the cone becomes possible. With further increase in the initial degree of saturation, a more stable bubble with larger height forms, the stable bubble gets pinned to the corners of the cone, and ultimately forms outside of the cone.

In Figure 17, for a certain initial degree of saturation (f_{init}) below saturation level, the height of the energy barrier for bubble formation becomes comparable to the depth of the

energy well of the stable state. At this critical value of initial degree of saturation, and when the energy barrier is sufficiently small, the "formation–disappearance fluctuation" happens as discussed in section 3.4.1 and presented in Figure 12 (in Figure 12, the system is initially supersaturated with other sets of parameters that results in "formation–disappearance fluctuation").

For the case in Figure 17, where the contact angle is $100°$ and the half cone apex angle is $22°$, with the cone mouth radius, w, of 50 μm, a stable bubble can form even with an initial degree of saturation that is below the saturation level. It should be noted that forming a stable bubble from an initially undersaturated liquid solution is not always possible. For example when the half cone apex angle, β, is 22°, and the contact angle, θ, is 30°, (keeping the same cone mouth radius, w, of 50 μm, and the same 5×10^{-5} initial number of moles of component 1) a stable bubble can only form out of a liquid solution that is initially supersaturated to an adequate level of supersaturation. Also for intermediate values of contact angle, such as θ of 120° with large cone apex angle β of 88°, again a bubble can only form out of a liquid solution that is initially supersaturated to an adequate level of supersaturation. Therefore whether the stable bubble can form from an initially undersaturated liquid solution, depends on geometry parameters and the contact angle, as well as the initial total number of moles, n_1 and n_2 (for example with θ of 120° and β of 88°, and w of 50 μm, a stable bubble can form outside of the cone from an undersaturated liquid with $f_{\text{init}} = 0.99$ if n_1 is 7×10^{-4} moles.)

In Figure 17, the total number of moles of component 1 is constant (5×10^{-5} moles), and the total number of moles of component 2 changes from 5.40×10^{-10} to 5.78×10^{-10} moles (according to Equation (56)), as the initial degree of saturation, f_{init}, changes from 0.98 to 1.05. If instead, the total number of moles of component 2 is constant, and the initial degree of saturation, f_{init}, increases (hence the total number of moles of component 1 decreases), our

investigations confirm the same pattern of behavior for the effect of the initial degree of saturation, f_{init}, on the stability of the system.

3.4.2. Binary bubble starting with a concave meniscus in a finite cone

In this section we investigate the cases where the solid is such that the vapor bubble makes a concave meniscus as it starts to form inside the cone. Let's consider the system with parameters similar to Ward and Levart[21], only with a different contact angle of $160°$ such that a bubble forms with a concave meniscus inside the cone (θ should be in the range that the bubble starts with a concave meniscus according to Equation (29)). The temperature is set at 25 ℃ and the pressure at 1 atm, with 2.5×10^{19} molecules (4.15×10^{-5} moles) of water and 3×10^{14} molecules (4.98×10^{-10} moles) of nitrogen (the initial degree of saturation of the liquid is therefore 1.089 according to Equation (56)). The mouth radius, w, of the cone is 50 μm, and the half cone apex angle, β, is 45°. Figure 18 shows the equilibrium states both with the method of intersection of the Kelvin radius with the geometry radius, and from the free energy diagram.

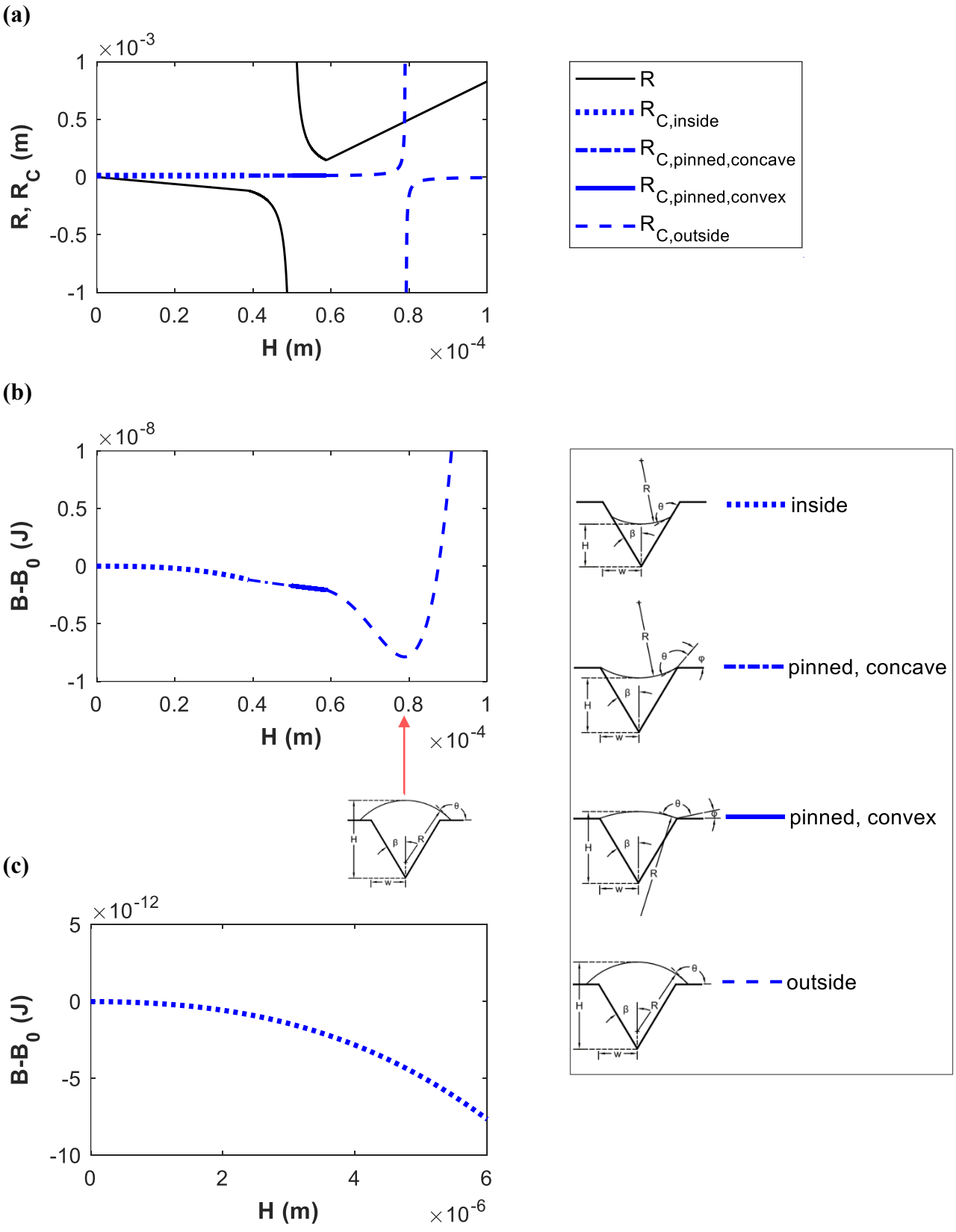
(a)
×10^-3
1
0.5
0
-0.5
-1
R, R_C (m)
0
0.2
0.4
0.6
0.8
1
H (m)
×10^-4
R
R_C,inside
R_C,pinned,concave
R_C,pinned,convex
R_C,outside
(b)
×10^-8
1
0.5
0
-0.5
-1
B-B_0 (J)
0
0.2
0.4
0.6
0.8
1
H (m)
×10^-4
inside
pinned, concave
pinned, convex
outside
(c)
×10^-12
5
0
-5
-10
B-B_0 (J)
0
2
4
6
H (m)
×10^-6

Figure 18. Equilibrium states of a bubble starting with a concave meniscus in a finite cone submerged in a liquid solution, (a) intersection of the Kelvin radius with the geometry radius versus height of the center of the liquid–vapor interface, (b) free energy versus height of the center of the liquid–vapor interface, (c) magnification of the energy axis for free energy versus height of the center of the liquid–vapor interface. The system is set to be at 25 ℃ and a liquid pressure of 1 atm, with the liquid initially containing 2.5×10^{19} molecules (4.15×10^{-5} moles) of water and 3×10^{14} molecules (4.98×10^{-10} moles) of nitrogen (initial degree of saturation of 1.089). The cone mouth radius, w, is 50 μm, and the half cone apex angle, β, is 45°. The contact angle, θ, is considered to be 160°. The status of the bubble (inside, or pinned with a concave meniscus or pinned with a convex meniscus to the corner, or outside the cone) is shown with different line types.

As presented in Figure 18 (a), for the bubble starting with a concave meniscus, the geometry radius (solid black line) starts from zero, and grows to a larger negative value, until it gets pinned, and grows further with a concave meniscus toward infinity (with negative number to show concave meniscus), until the meniscus becomes flat. The bubble then further grows by changing the meniscus to convex (positive sign), while still pinned to the corners. The geometry radius decreases until the meniscus makes a contact angle of θ with the outer solid. Then further growth of the bubble happens outside the cone as the radius increases.

Figure 18 shows that this system has only one equilibrium state, which is stable (one intersection in Figure 18 (a), and only one extremum in Figure 18 (b), which is a minimum point). The system of Figure 18 does not have any unstable equilibrium (as shown in the close-up of the smaller range in Figure 18 (c)), hence when the bubble starts with a concave meniscus, no initial energy barrier needs to be overcome to reach the stable equilibrium. The stable equilibrium state for this case occurs after the bubble grows out of the cone, and the meniscus has changed from concave to convex. Changes in the concavity from concave to convex happen to maintain the same contact angle with the outside of the finite cone. The value of η from Equation (51) is always very close to 1 similar to the previous case of a bubble starting with a convex meniscus. Here, the mean value of η is 1.0007, with average deviation of 2.11×10^{-6} from the mean value.

Next, we applied our method to the system with parameters selected in research by Jones *et al.*,[33] that is pore diameter of 759 nm ($w = 3.795 \times 10^{-7}$ m), cone angle of 30° ($\beta = 15°$), and contact angle of $120°$. We considered 3.24×10^{-19} moles of water and an initial

degree of saturation of 1.089 (the same initial degree of saturation as considered by Ward and Levart[21]). With these values of water and the initial degree of saturation, there are 3.89×10^{-24} moles of nitrogen in the system. Figure 19 shows the total free energy for such a system, along with the contribution of specific terms, $\Delta B_{\text{Laplace}}$, $\Delta B_{\text{Surface}}$, and $\Delta B_{\text{Chemical potential}}$ to the free energy with respect to the reference point according to Equation (55).

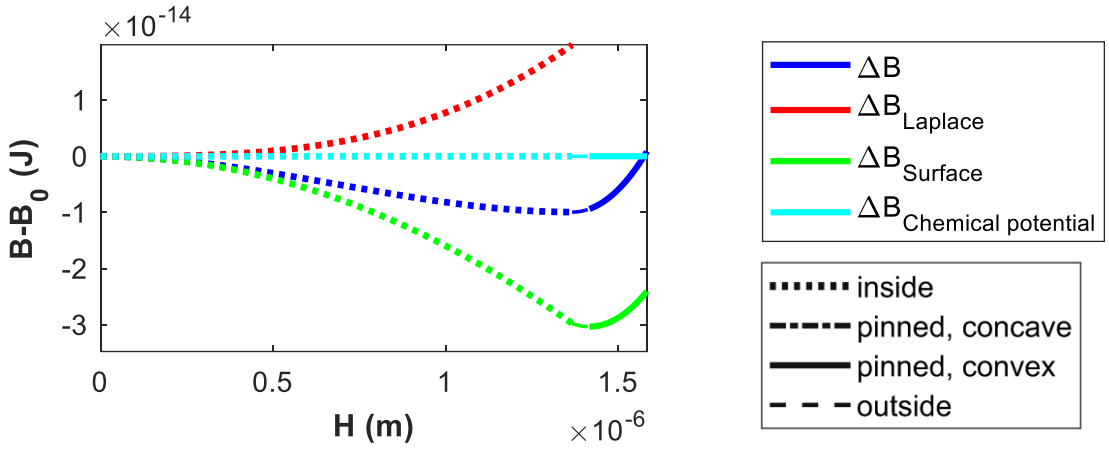

Figure 19. Contributions of the Laplace term, $\Delta B_{\text{Laplace}}$, the surface term, $\Delta B_{\text{Surface}}$, and the chemical potential term, $\Delta B_{\text{Chemical potential}}$, to the free energy, ΔB, of a bubble starting with a concave meniscus in a finite cone submerged in a liquid solution. The system is set to be at 25 ℃ and a liquid pressure of 1 atm, with the liquid initially containing 3.24×10^{-19} moles of water and initial degree of saturation of 1.089 (3.89×10^{-24} moles of nitrogen). The cone mouth radius, w, is 3.795×10^{-7} m, and the half cone apex angle, β, is 15°. The contact angle, θ, is considered to be 120°. The status of the bubble (inside, or pinned with a concave meniscus or pinned with a convex meniscus to the corner, or outside the cone) is shown with different line types.

For the case of Figure 19, the stable bubble forms at the threshold where pinning starts from inside the cone with a concave meniscus. An adequate number of moles are available in the system to form the stable equilibrium. As shown in Figure 19, the surface term, $\Delta B_{\text{Surface}}$ has a dominant effect on the total free energy ΔB. Due to the smaller size of the system at the stable equilibrium (on the order of micrometers here, compared to hundreds of micrometers in Figure 11) the surface effect is a dominant term.

Besides the systems discussed above that have one equilibrium state, there are some systems with three equilibrium states. Figure 20 demonstrates an example of such a system where the bubble that starts with a concave meniscus, forms a metastable equilibrium (local

minimum in free energy versus size) while the bubble is pinned with a convex meniscus, and evolves to a stable bubble outside the cone, after passing a maximum point (unstable equilibrium).

(a)

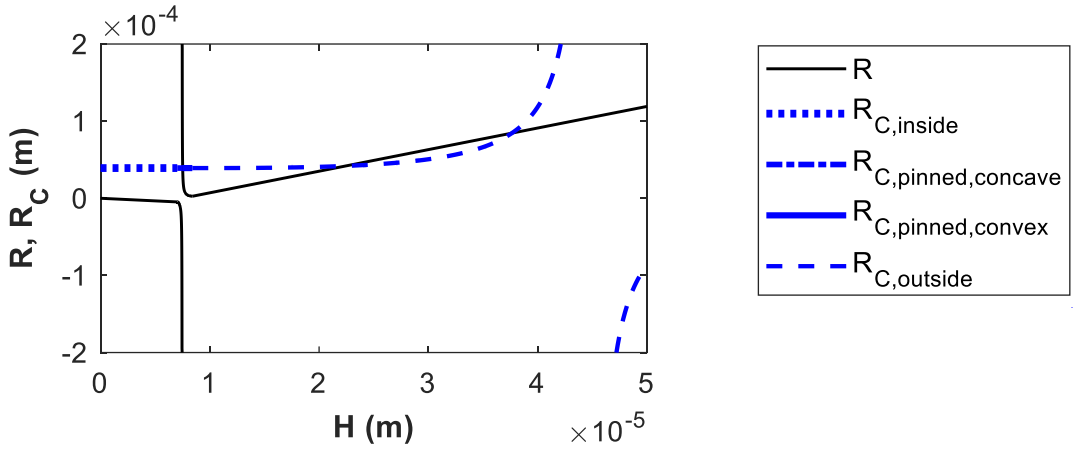
×10^-4
2
1
0
-1
-2
R, R_C (m)
0
1
2
3
4
5
H (m)
×10^-5
R
R_C,inside
R_C,pinned,concave
R_C,pinned,convex
R_C,outside

(b)

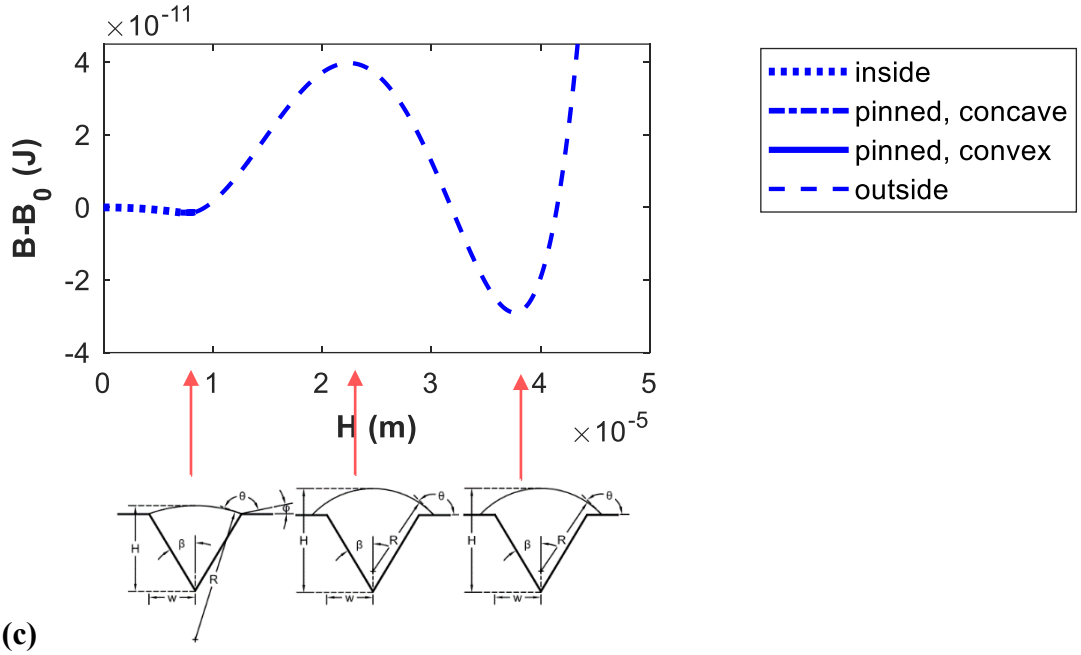
×10^-11
4
2
0
-2
-4
B-B_0 (J)
0
1
2
3
4
5
H (m)
×10^-5
inside
pinned, concave
pinned, convex
outside

(c)

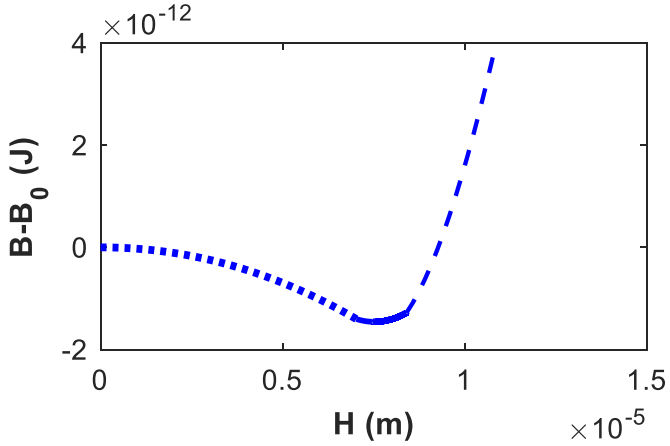
×10^-12
4
2
0
-2
B-B_0 (J)
0
0.5
1
1.5
H (m)
×10^-5

Figure 20. System with a local and a global minimum in the free energy of a bubble starting with a concave meniscus in a finite cone submerged in a liquid solution, (a) intersection of the Kelvin radius with the geometry radius versus height of the center of the liquid–vapor interface, (b) free energy versus height of the center of the liquid–vapor interface, (c) magnification of the local minimum in free energy versus height of the center of the liquid–vapor interface. The system is set to be at 25 ℃ and a liquid pressure of 1 atm, with the liquid initially containing 4×10^{-5} moles of water and initial degree of saturation of 1.005 (hence 4.43×10^{-10} moles of nitrogen). The cone mouth radius, w, is 2×10^{-6} m, and the half cone apex angle, β, is 15°. The contact angle, θ, is considered to be 130°. The status of the bubble (inside, or pinned with a concave meniscus or pinned with a convex meniscus to the corner, or outside the cone) is shown with different line types.

Figure 20 (a) and (b) shows the three equilibrium states in the system. The system forms a metastable equilibrium while it is pinned to the corner of the cone with a convex meniscus (more visible in the magnified graph of Figure 20 (c)). The bubble then passes through an energy barrier (unstable equilibrium) to form the stable equilibrium state outside the cone.

The question may arise: for a system with a bubble starting with a concave meniscus, if the equilibrium state happens while the bubble is pinned to the corner with a convex meniscus, will this equilibrium state always be metastable? For a system with the specifications of Figure 20, except with a larger cone mouth radius, w, of 3×10^{-5} m (approximately one order of magnitude larger), the stable equilibrium (global minimum) forms when the bubble is pinned with a convex meniscus, and the system has only one equilibrium point. This is because for a cone with larger mouth radius, w, the volume of the cone (vapor that can be in the cone) increases as well.

In the next sections, we investigate the effect of various parameters on the formation of a stable bubble, as well as whether it is formed inside, or pinned, or outside the cone.

3.4.2.1. Effect of cone apex angle 2β for a bubble starting with a concave meniscus

Figure 21 shows the effect of cone apex angle on the stability of a bubble starting with a concave meniscus inside a cone.

(a) $\theta = 100°$

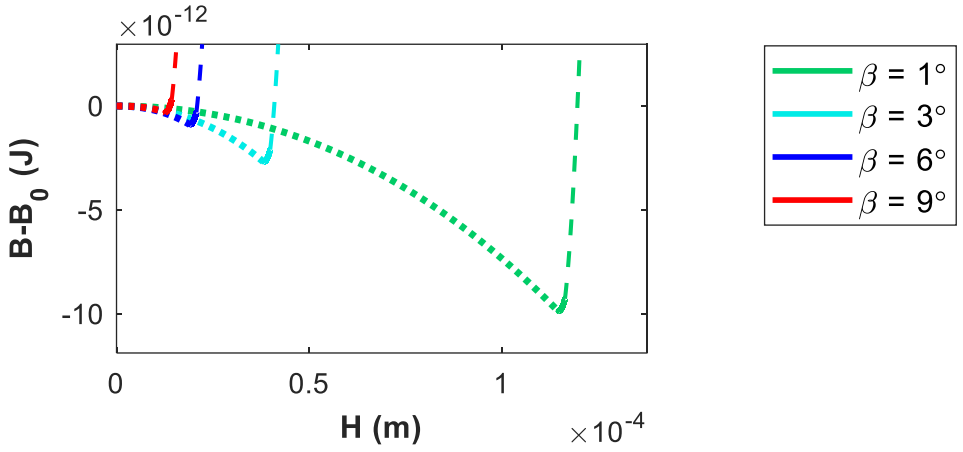

(b) $\theta = 140°$

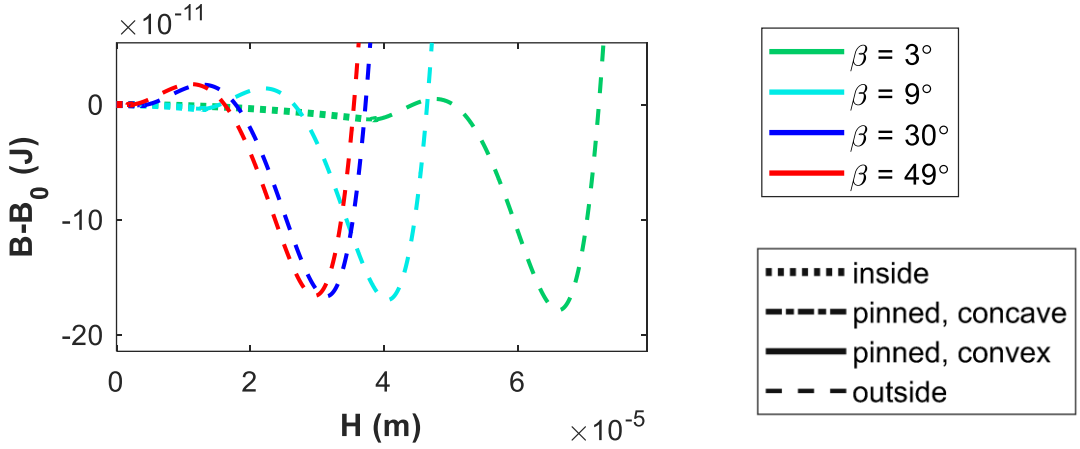

Figure 21. Effect of half cone apex angle, β, on equilibrium states of a bubble starting with a concave meniscus in a finite cone submerged in a liquid solution. The system is set to be at 25 ℃ and a liquid pressure of 1 atm, with the liquid initially containing 4×10^{-5} moles of water and the initial degree of saturation of 1.005 (that is 4.43×10^{-10} moles of nitrogen). The cone mouth radius, w, is 2 μm. (a) contact angle θ of 100°, and (b) contact angle θ of 140°. The status of the bubble (inside, pinned with a concave or pinned with a convex meniscus to the corner, or outside the cone) is shown with different line types.

As the cone apex angle increases, while keeping the cone mouth radius constant, the height of the cone decreases. With a cone mouth radius of 2 μm, the cone height decreases from 1.14×10^{-4} m to 1.74×10^{-6} m, when the cone half apex angle changes from 1° to 49°. As presented in Figure 21, increasing the cone apex angle results in a stable equilibrium with smaller height, and less stability, both in case (a) where the system has one equilibrium state, and in case (b) where the system has three equilibrium states and evolves to a global stable minimum after passing an energy barrier moving from the metastable equilibrium state.

3.4.2.2. Effect of cone mouth radius w for a bubble starting with a concave meniscus

The effect of cone mouth radius on the stability of a bubble starting with a concave meniscus is shown in Figure 22. Increasing cone mouth radius is equivalent to the effect of increasing the cone height since the cone apex angle is kept constant.

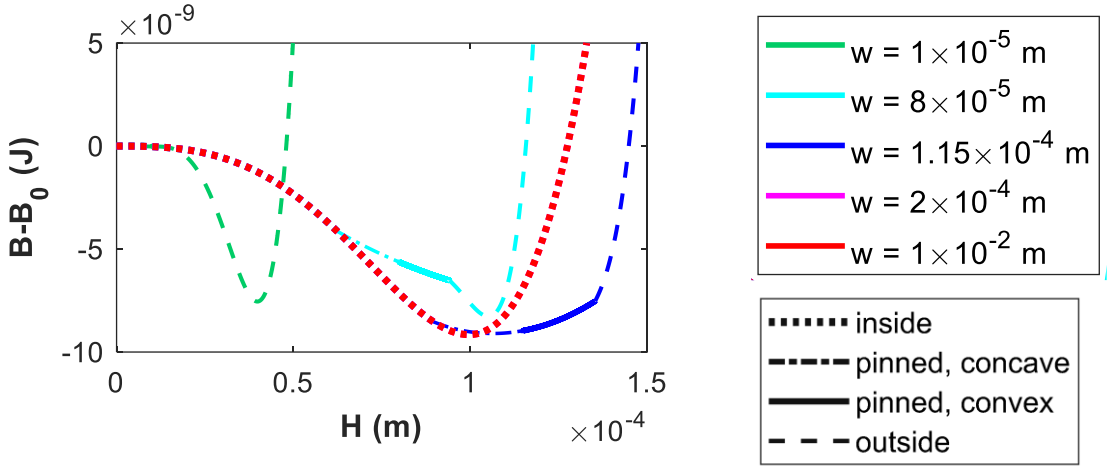

Figure 22. Effect of cone mouth radius, w, on equilibrium states of a bubble starting with a concave meniscus in a finite cone submerged in a liquid solution. The system is set to be at 25 ℃ and a liquid pressure of 1 atm, with the liquid initially containing 4.15×10^{-5} moles of water and 4.98×10^{-10} moles of nitrogen (initial degree of saturation of 1.089). The cone half apex angle, β, is 45°, and the contact angle, θ, is considered to be 160°. The status of the bubble (inside, pinned with a concave or pinned with a convex meniscus to the corner, or outside the cone) is shown with different line types.

As presented in Figure 22, increasing the cone mouth radius results in stable bubble formation changing from forming outside, to forming pinned, and ultimately forming inside the cone, with more stability. When the cone mouth radius is large enough that the bubble forms inside, further increase of the cone mouth radius does not have much effect on the energy level or height of the stable point, as presented by the overlapping curves for the two largest cone mouth radii in Figure 22. Therefore, for the infinite cone (with infinite cone mouth radius and cone height, while cone apex angle is kept fixed), the stable bubble starting with a concave meniscus forms inside the cone with the energy and height of the stable point almost the same as the value of minimum point of the pink or red curve (for w of 2×10^{-4} or 1×10^{-2} m) in Figure 22.

3.4.2.3. Effect of contact angle θ for a bubble starting with a concave meniscus

Figure 23 shows the effect of contact angle on the equilibrium states of a bubble starting with a concave meniscus inside the cone.

(a) $\beta = 30°$

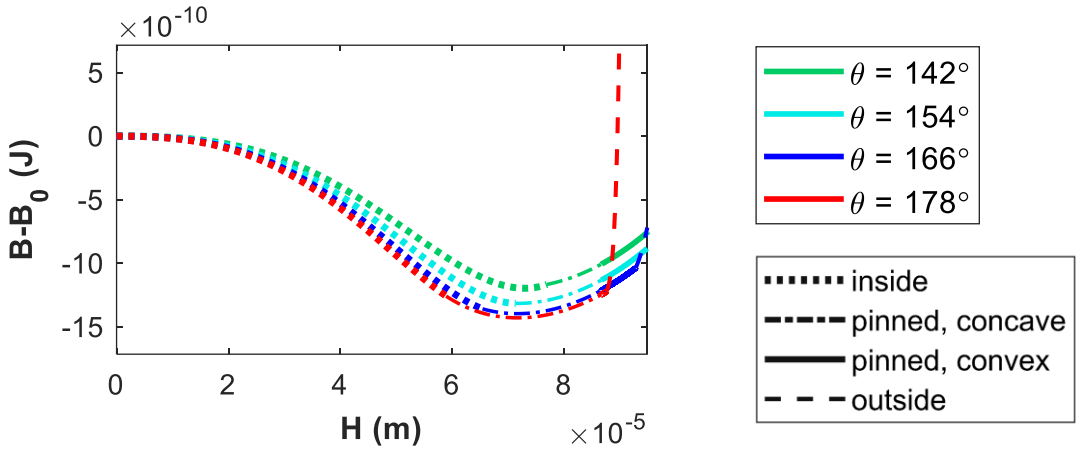

(b) $\beta = 50°$

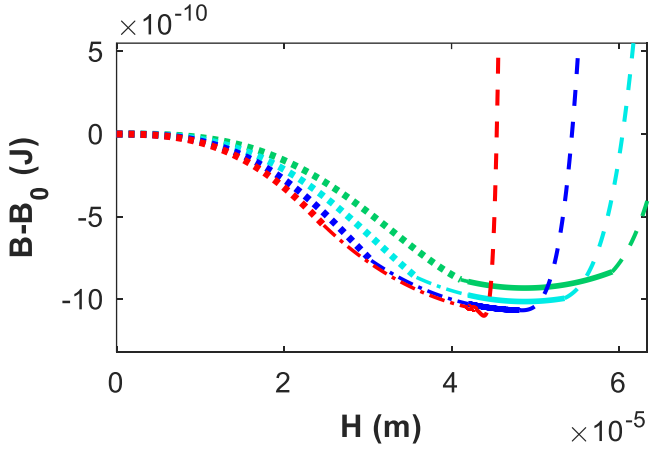

Figure 23. Effect of contact angle, θ, on the equilibrium states of a bubble starting with a concave meniscus in a finite cone submerged in a liquid solution. The system is set to be at 25 ℃ and a liquid pressure of 1 atm, with the liquid initially containing 4×10^{-6} moles of water and an initial degree of saturation of 1.1 (hence 4.85×10^{-11} moles of nitrogen). The cone half apex angle, β, is (a) 30° and (b) 50°, and the cone mouth radius, w, is 50 μm. The status of the bubble (inside, pinned with a concave or pinned with a convex meniscus to the corner, or outside the cone) is shown with different line types.

Increasing the contact angle (getting farther from the transition contact angle, θ_t) results in higher stability of the stable point. In Figure 23 (a), with β of 30°, the stable equilibrium forms inside the cone for smaller contact angles, and forms pinned to the corner with a concave meniscus for larger contact angles. For a cone with higher cone apex angle, such as

for β of 50° in Figure 23 (b), the stable equilibrium forms pinned with a convex meniscus for smaller contact angles, and forms outside the cone for larger contact angles. When investigating the effect of contact angle, it should be noted that θ must be in the range described in Equation (29) to maintain the case of the bubble starting with a concave meniscus.

3.4.2.4. Effect of total numbers of moles, with constant initial degree of saturation, for a bubble starting with a concave meniscus

Figure 24 presents the effect of total numbers of moles of component 1 and 2 on the stability of a bubble starting with a concave meniscus in a finite cone. n_1 and n_2 are changed such that the initial degree of saturation remains the same according to Equation (56).

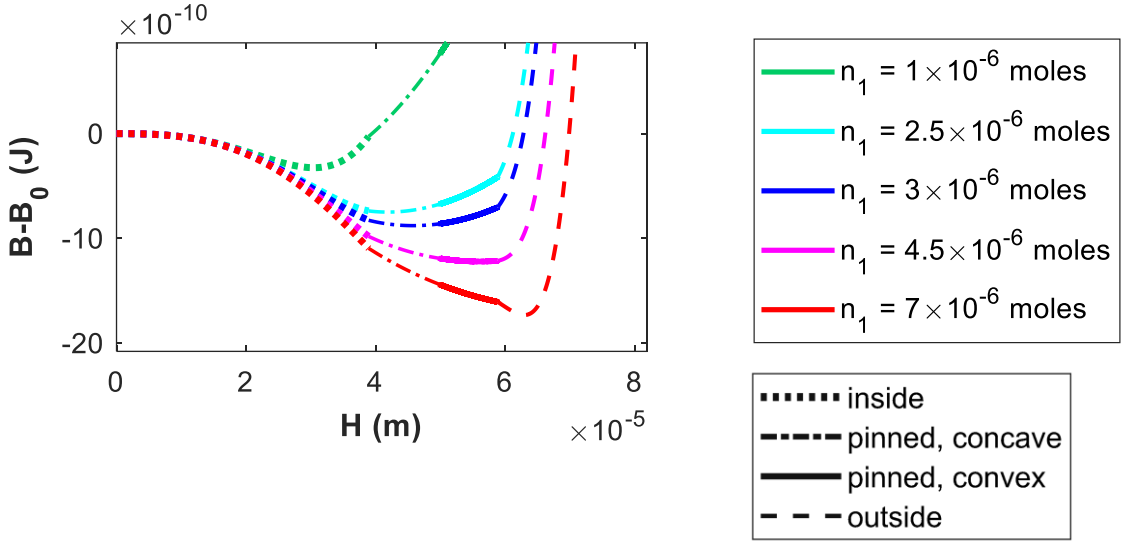

Figure 24. Effect of total numbers of moles, n_1 and n_2, on the stability of a bubble starting with a concave meniscus in a finite cone submerged in a liquid solution, while initial degree of saturation remains the same (1.1) for each set of n_1 and n_2. The cone mouth radius, w, is 50 μm, and the half cone apex angle, β, is 45°. The contact angle, θ, is considered to be 160°. The status of the bubble (inside, or pinned with a concave meniscus or pinned with a convex meniscus to the corner, or outside the cone) is shown with different line types.

Increasing the total numbers of moles of components 1 and 2, such that the initial degree of saturation remains the same, results in a stable equilibrium state with more stability and larger bubble height. In Figure 24, to maintain a constant initial degree of saturation of 1.1, as n_1 changes from 1×10^{-6} to 7×10^{-6} moles, n_2 changes from 1.21×10^{-11} to $8.48 \times$

10^{-11} moles, according to Equation (56). This trend happens for any values of initial degree of saturation down to f_{init} of zero, which is the case of a pure system of component 1 ($n_2 = 0$). For smaller values of initial degree of saturation, the system is less sensitive to the total numbers of moles. For pure bubble formation starting with a concave meniscus, the stable equilibrium is independent of the total number of moles (as will be discussed in more detail in the next section).

3.4.2.5. Effect of initial degree of saturation for a bubble starting with a concave meniscus

Figure 25 shows the effect of initial degree of saturation, f_{init}, on the stability of a bubble starting with a concave meniscus in a finite cone submerged in a liquid solution, while keeping the total number of moles of component 1 (solvent) constant.

(a)

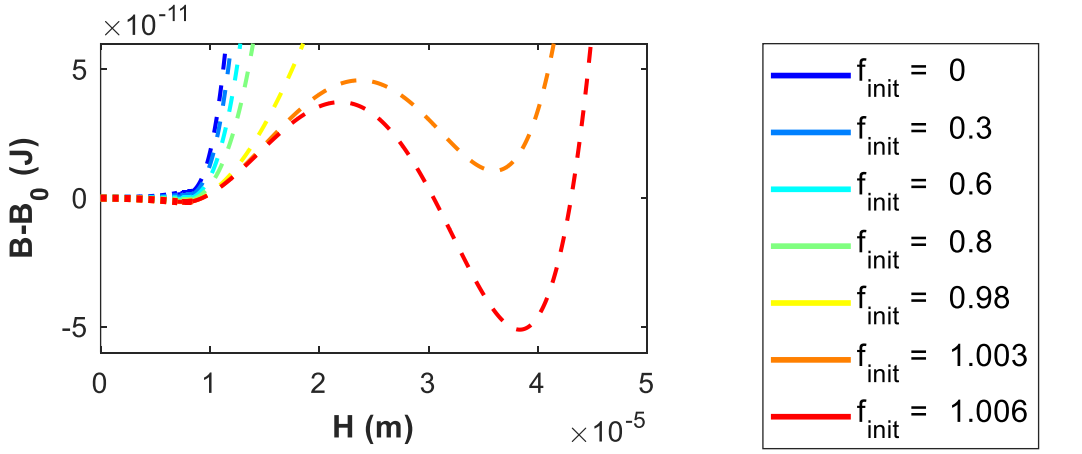
×10^-11
5
0
-5
B-B0 (J)
0
1
2
3
4
5
H (m)
×10^-5
finit = 0
finit = 0.3
finit = 0.6
finit = 0.8
finit = 0.98
finit = 1.003
finit = 1.006

(b)

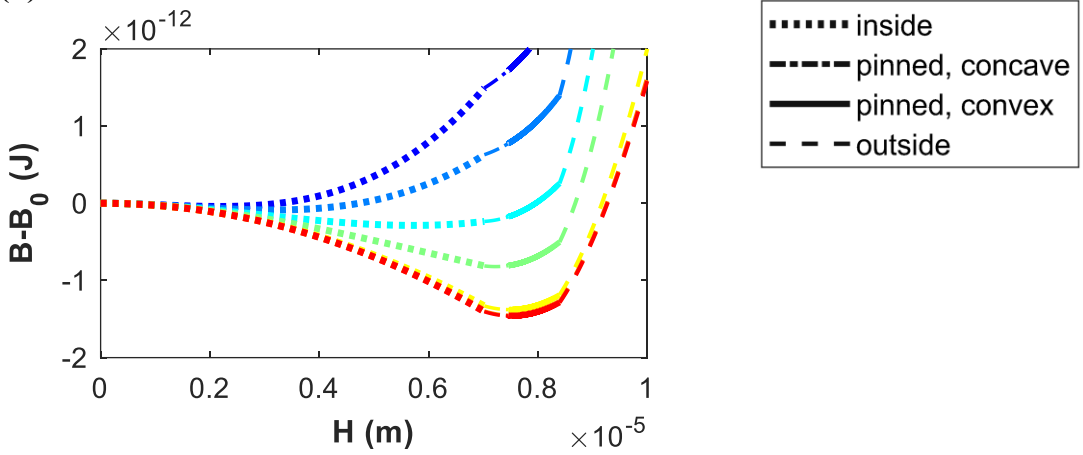
×10^-12
2
1
0
-1
-2
B-B0 (J)
0
0.2
0.4
0.6
0.8
1
H (m)
×10^-5
inside
pinned, concave
pinned, convex
outside

(c)

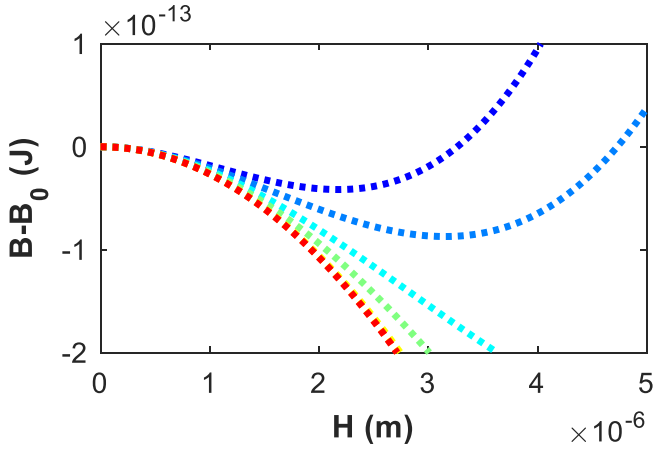
×10^-13
1
0
-1
-2
B-B0 (J)
0
1
2
3
4
5
H (m)
×10^-6

Figure 25. (a) Effect of initial degree of saturation, f_{init}, on the stability of a bubble starting with a concave meniscus in a finite cone submerged in a liquid solution, while the total number of moles of component 1, n_1, is constant (4×10^{-5} moles). The cone mouth radius, w, is 2×10^{-6} m, and the half cone apex angle, β, is 15°. The contact angle, θ, is considered to be 130°, (b) magnification to show the minimum points for the intermediate values of f_{init}, (c) magnification to show the minimum points for smaller values of f_{init} down to $f_{\text{init}} = 0$. The status of the bubble (inside, or pinned with a concave meniscus or pinned with a convex meniscus to the corner, or outside the cone) is shown with different line types.

Decreasing the initial degree of saturation, f_{init}, results in a stable equilibrium with less stability, as presented in Figure 25. As the initial degree of saturation changes from 1.006 to 0, while keeping n_1 constant at 4×10^{-5} moles, n_2 is changed from 4.43×10^{-10} moles to 0. For intermediate values of initial degree of saturation, Figure 25 (b) shows the stable bubble pinned to the corner with a concave meniscus. Unlike the case of a bubble starting with a convex meniscus, in this case of a bubble starting with a concave meniscus, a stable equilibrium forms from undersaturated solutions with smaller initial degree of saturation down to zero, as presented in Figure 25 (c). For pure solution ($f_{\text{init}} = 0$), the Kelvin radius becomes a constant value, independent of the total number of moles, as the general Kelvin equation (47) simplifies to Equation (53) when $n_2 = 0$. When liquid pressure is above the saturation pressure (such as for the cases in this work), the Kelvin radius calculated from Equation (47) or (53) has a negative value, which implies that the system has an equilibrium which can only form with a concave meniscus, inside or pinned to the corner. For example for the specifications of Figure 25 with $f_{\text{init}} = 0$, the stable equilibrium state forms at the Kelvin radius of -1.46×10^{-6} m. The results for the pure solution also agree with the results of our previous paper[73] for pure water, when $P^L > P_{1,\infty}$, where a stable equilibrium forms in the cone only with a concave meniscus (In our previous paper,[73] the sign of the Kelvin radius for a concave meniscus was positive as pressure difference was defined as $P^L - P^V$, rather than $P^V - P^L$ as in this study).

It should be noted that in Figure 25, for some of the values of initial degree of saturation, the system has three equilibrium states, a maximum indicating an unstable equilibrium, a local minimum indicating a metastable point, and a global minimum indicating

a stable point. When $f_{\text{init}} = 1.006$ the system of Figure 25 has a metastable equilibrium while pinned with a convex meniscus, and as the bubble grows outside the cone, after passing an energy barrier it reaches the stable equilibrium. For some other values of f_{init}, the system with three equilibrium states forms its stable equilibrium while pinned to the corner with a convex meniscus. For example for system with $f_{\text{init}} = 1.003$ the system of Figure 25 forms a stable equilibrium while pinned with a convex meniscus, followed by an unstable and a metastable equilibrium forming outside the cone.

We also investigated the effect of initial degree of saturation for a bubble starting with a concave meniscus, where instead of keeping n_1 constant and changing n_2, the initial degree of saturation was changed by keeping n_2 constant, and changing n_1. The trend of changes in the free energy of the stable point as a result of changes in the initial degree of saturation is the same, regardless of keeping n_1 or n_2 constant.

3.5. Chapter Conclusion

In this study, comprehensive thermodynamic stability analysis of two-component vapor formation from a two-component liquid solution at constant temperature and liquid pressure inside a finite cone was investigated. For a liquid–vapor interface inside a confined geometry, it is more useful to categorize the cases based on the concavity of the meniscus, rather than categorizing the solid into hydrophobic or hydrophilic based on a contact angle of 90°. Concavity of the meniscus (convex or concave) inside a confined geometry is judged based on the "transition contact angle".[72,73,85]

We explained the procedure of analyzing the thermodynamic stability and number of potential equilibrium states for vapor formation out of liquid solution inside a finite cone, starting with either a convex or a concave meniscus, as summarized in Table 3. The stability of the system was fully investigated not only for the bubble as it grows inside the cone, but also as the bubble gets pinned to the corners of the cone for further growth, and ultimately grows outside the cone. The concentration changes in both vapor and liquid phases as a result

of bubble growth were carefully accounted for. In the case of a bubble starting with a concave meniscus inside the cone, the meniscus changes from concave to convex while the bubble is pinned, so that the bubble can maintain the same contact angle with the solid as it grows outside the cone. Our investigation included the case of pure phases, and the infinite cone as the limiting extremes of this study, and for verification of the method with our previous studies.[72,73]

Table 3. Summary of thermodynamic stability analysis for vapor formation starting with a convex meniscus or a concave meniscus inside a finite cone, from a liquid solution at constant temperature and liquid pressure (above the saturation pressure of the solvent).

	Bubble starting with a convex meniscus, $\theta < \beta + 90°$	**Bubble starting with a concave meniscus , $\theta > \beta + 90°$**
Potential growth configuration	Figure 9 (a), (b), (c)	Figure 9 (d), (e), (f), (g)
Pure phases	No bubble formation	Always forms only 1 stable equilibrium state, with a concave meniscus (inside or pinned)
2-component phases	For $f_{init} > f_{critical}$ ---------- • Initial energy barrier • 2 equilibrium states (unstable → stable) • Stable equilibrium may form **convex,** inside / pinned / outside --- For $f_{init} < f_{critical}$ ---------- No bubble formation	For any $f_{init} > 0$ ---------- • No initial energy barrier • 1 equilibrium state (stable) OR 3 equilibrium states (metastable → unstable → stable or stable → unstable → metastable) • Stable equilibrium may form **concave** inside / **concave** pinned / **convex** pinned / **convex** outside

For a bubble starting with a convex meniscus ($\theta < \beta + 90°$) from a liquid solution (above the saturation pressure of the solvent) inside a cone at constant temperature and liquid pressure, stable bubble formation is only possible when the initial liquid is above a certain

concentration (which can be super- or under-saturated), depending on other specifications of the system. Formation of a stable bubble is only possible after passing an initial energy barrier. The stable equilibrium may form pinned to the corners of the cone such as the case reported by Ward and Levart,[21] but may form inside or outside the cone for systems with certain other specifications.

"Formation–disappearance fluctuation" of the bubble occurs when the size of the energy barrier of the unstable equilibrium becomes comparable to the size of the energy well for the stable equilibrium, and if the energy barrier is sufficiently small. It should be noted that for a bubble forming from a liquid solution (at pressure above the saturation pressure of the solvent) inside the cone, the "formation–disappearance fluctuation" may only happen for cases where the bubble starts with a convex meniscus, where there is an initial energy barrier. "Formation–disappearance fluctuation" of the bubble may happen from a solution that is initially supersaturated (such as in Figure 12) or undersaturated (such as in Figure 17), depending on other parameters of the system. This behavior is similar to the phenomena that has been observed[88] and explained[70,72,89–91] in the formation of capillary bridges in the gap between two solid surfaces, when the two solids that form the gap are at a critical distance.

For a bubble starting with a concave meniscus ($\theta > \beta + 90°$) from a liquid solution (above the saturation pressure of the solvent) inside a cone at constant temperature and liquid pressure, the system always forms a stable bubble, which is not necessarily inside the cone, unlike for the case mentioned by Jones *et al*.[33] Depending on the specifications of the system, the stable bubble may form inside the cone with a concave meniscus, pinned to the corners with a concave or convex meniscus, or outside the cone with a convex meniscus. No initial energy barrier exists for this case of a bubble starting with a concave meniscus from a liquid solution above the saturation pressure of the solvent, in a cone. Some systems have only one equilibrium state, which is stable. Some other systems have three equilibrium states: a local or global minimum in free energy while the bubble is pinned, followed by an energy barrier

(unstable equilibrium state), followed by another minimum point forming outside the cone, as shown in Figure 25 for initial degree of saturation of 1.006 and 1.003. The local minimum point is the metastable equilibrium, and the global minimum point is the stable equilibrium state.

For a pure liquid inside a cone ($f_{\text{init}} = 0$), and when liquid pressure is above the saturation pressure of the pure solvent, the Kelvin radius becomes a constant number with a sign that matches only to a bubble with a concave meniscus, either inside or pinned to the corners of the cone. Therefore, no bubble can form if the solid material is such that the bubble would form with a convex meniscus. In the extreme case of an infinite cone and pure phases, the results of this research match with the previous study of pure bubble formation from a pure liquid inside an infinite cone.[73]

For each of the cases of bubble formation from a liquid solution (above the saturation pressure of the solvent) inside a finite cone, starting with a concave or convex meniscus, we also investigated the effects of the key parameters: cone apex angle (2β), cone mouth radius (w), contact angle (θ), total numbers of moles (n_1 or n_2), and initial degree of saturation of the liquid solution (f_{init}), as summarized in Table 4.

Table 4. Summary of the effects of different key parameters on the potential equilibrium states of vapor formation starting with a convex or concave meniscus from a liquid solution at constant temperature and liquid pressure (above the saturation pressure of the solvent) inside a finite cone

	Bubble starting with a convex meniscus, $\theta < \beta + 90°$	**Bubble starting with a concave meniscus , $\theta > \beta + 90°$**
$\boldsymbol{\beta}$ ↑	Trend of changes in the stability of stable point depends on other parameters H_{stable} ↓	Stability of stable point decreases H_{stable} ↓
$\boldsymbol{w}$ ↑	Stability of stable point increases (larger negative ΔB_{stable}) Stable bubble shifts from forming outside, to pinned, to ultimately inside	Stability of stable point increases Stable bubble shifts from forming outside, to pinned, to ultimately inside
$\boldsymbol{\theta}$ ↑	(θ gets closer to θ_t) Stability of stable point increases Stable bubble shifts from forming inside, to pinned, to ultimately outside	(θ gets farther from θ_t) Stability of stable point increases Stable bubble shifts from forming inside, to pinned, to ultimately outside
$\boldsymbol{n_i}$ ↑ **(f_{init} = const.)** **OR** $\boldsymbol{f}_{\text{init}}$ ↑ **(n_1 or n_2 = const.)**	Stability of stable point increases H_{stable} ↑ Stable bubble shifts from forming inside, to pinned, to ultimately outside	Stability of stable point increases H_{stable} ↑ Stable bubble shifts from forming inside, to pinned, to ultimately outside

For bubble formation from a liquid solution inside a cone (at constant temperature and liquid pressure above the saturation pressure of the solvent), the stability of the stable point increases by increasing the cone mouth radius (w), the contact angle (θ), the total number of moles (n_i), or the initial degree of saturation of the liquid solution (f_{init}). This trend does not depend on the shape of the meniscus of the starting bubble ($\theta < \beta + 90°$ or $\theta > \beta + 90°$). The effect of the changes in cone apex angle (2β) on the stability of the stable point depends on the shape of the meniscus when the bubble starts to form. A summary of the details of the

effects of parameters on where the stable bubble forms (inside, pinned or outside the cone) can be found in Table 4.

A comprehensive investigation of bubble formation from a liquid solution inside a cone at constant temperature and constant liquid pressure (above the saturation pressure of the solvent) is presented in this work. The investigation includes some of the previous cases where the stable bubble forms pinned to the cone with a convex meniscus,[21] or forms inside the cone with a concave meniscus,[33] or a pure bubble forms with a concave meniscus inside an infinite cone.[73] However, these previous cases were only parts of the puzzle, and the present investigation adds the missing pieces to the puzzle. In the comprehensive picture, we show here that a bubble starting with a convex meniscus may form a stable equilibrium inside, pinned, or outside the cone depending on the system specifications. Also a bubble starting with a concave meniscus may form a stable equilibrium while it is inside or pinned with a concave meniscus, or pinned or outside with a convex meniscus. The "formation–disappearance fluctuation" of a bubble starting with a convex meniscus is observed when the system specifications are such that the energy barrier and the energy well are of comparable sizes, and the energy barrier is small enough for spontaneous fluctuations to overcome the energy barrier. The comprehensive picture presented here also includes the effects of different parameters (cone apex angle (2β), cone mouth radius (w), contact angle (θ), total numbers of moles (n_1 or n_2), and initial degree of saturation of the liquid solution (f_{init}) on the stability of the stable point.

4. Comparison of the osmotic virial equation with the Margules activity model for solid–liquid equilibrium

4.1. Chapter summary

The main goal of this chapter is to compare the general polynomial forms of the osmotic virial equation and the Margules model for the liquid activity coefficients in binary systems. The coefficients/parameters in each model can be calculated based on best fits to experimental phase equilibrium data. Here the activity coefficient models were combined with the equation of solid–liquid equilibrium. We obtain the coefficients/parameters for the osmotic virial equation and the one- and two-parameter Margules models, and compare the accuracy of each model for fitting the experimental data for five water/solute systems: water/glycerol, water/acetic acid, water/propanoic acid, water/mono-ethylene glycol and water/sulfonale. In obtaining the osmotic virial coefficients, we present a method to fit the equation to the entire range of data including both the ice-formation region and the solute-precipitation region. In expression of the concentration effect of the solute, we showed that the integration constant that arises from the Gibbs–Duhem equation is dependent on the osmotic virial coefficients. The osmotic virial equation is of great interest for its ability to empirically model a very wide range of aqueous solutions and as such is one of the most widely used solution models in biology.

4.2. Introduction

When two phases α and β are in equilibrium at constant temperature and pressure, the following equality is satisfied:[92]

$$\mu_i^{\alpha} = \mu_i^{\beta} \tag{72}$$

where μ_i^{α} and μ_i^{β} are the chemical potentials of component *i* in phases α and β respectively. The distribution of component i between the two phases at equilibrium can be obtained from equation (72). Solid–liquid equilibrium is among different types of phase equilibria, hence the condition for solid–liquid equilibrium comes from equation (72), where α and β represent solid and liquid phases. Solid–liquid equilibrium is widely observed in various phenomena and technologies such as ice–solution equilibrium during freezing/thawing processes in cryopreservation of cells and tissues, in freeze-drying techniques that are used in the pharmaceutical and food industries, and in solute crystallization, among many others.

To apply the fundamental equation of phase equilibrium, equation (72), it is necessary to describe the chemical potential of component *i* in solution, in terms of temperature, pressure and phase composition, and for this purpose some auxiliary functions such as activity have been introduced.[92] The chemical potential of component *i* in the liquid phase (superscript *L*) can be expressed as:[92]

$$\mu_i^L(T^L, P^L, x_i^L) = \mu_{i,\mathrm{ref}}^L(T_{\mathrm{ref}}, P_{\mathrm{ref}}) + \int_{P_{\mathrm{ref}}}^{P^L} v_{0,i}^L \mathrm{d}P - \int_{T_{\mathrm{ref}}}^{T^L} s_{0,i}^L \mathrm{d}T + RT^L \ln(x_i^L \gamma_i^L) \tag{73}$$

where T^L and P^L are temperature and pressure of the liquid phase, x_i^L is the mole fraction of component i in the liquid, $\mu_{i,\mathrm{ref}}^L$ is the chemical potential of pure liquid component *i* at a reference temperature T_{ref} and reference pressure P_{ref}, $v_{i,0}^L$ and $s_{i,0}^L$ are the molar volume and molar entropy of pure liquid component i, R is the universal gas constant, and γ_i^L is the activity coefficient of component i in the liquid phase mixture. Activity coefficient models are a way to describe the nonideal behavior of component i interacting with other components in a mixture.

As liquid is involved in solid–liquid equilibrium, an appropriate activity coefficient model is required in equation (73). We briefly review the most frequently used models for activity coefficients. The activity coefficient models can be divided into three groups:[92,93] (a) empirical models, (b) theoretical models based on solution theories, and (c) equations of state.

(a) Empirical models (based on some theory combined with physical intuition): Among empirical equations, the Margules and van Laar equations (which are special cases of the more general Wohl expansion[92]) give a good representation of even fairly nonideal binary mixtures, with the merit of mathematical simplicity. However, they have a drawback of requiring ternary data (along with binary data) for prediction of multicomponent mixtures.[94] Only when simplifying assumptions are made with the two-suffix Margules equation and the van Laar equation, can all constants for prediction of multicomponent mixtures be obtained from binary data alone. According to Prausnitz,[92] such simplifying assumptions may not work for liquid–liquid equilibrium, which is highly sensitive to the constants of the model.

(b) Theoretical models based on solution theories: There are various types of solution theories to describe the activity coefficients of components in the solution.

Local composition models such as Wilson, NRTL (Non-Random, Two-Liquid), and UNIQUAC (UNIversal QUAsi-Chemical) equations account for differences in molecular size and intermolecular forces. They are implicitly generalized for multicomponent systems, with the parameters from the constituent binary data.[92] The Wilson model is restricted to completely miscible mixtures,[92] and is therefore not applicable for activity coefficients in liquid–liquid equilibrium.[94] For aqueous solutions, the NRTL model is found to be the best model that works for both the vapor–liquid and liquid–liquid equilibrium of binary and multicomponent systems,[94] even for strongly nonideal systems.[92] The NRTL model is applicable to both partially miscible systems (unlike the Wilson model), and completely miscible systems. However, the NRTL model has the disadvantage of containing three parameters for each pair of components (compared to the two-parameter models of

UNIQUAC, Wilson, Margules and van Laar).[94] One of those parameters (α) was shown to be in the range of 0.20 to 0.47 for a large number of binary systems[92] (about 0.4 for aqueous organic mixtures[94]). Choosing a value for α, the NRTL model reduces to a two-parameter model.[92] The UNIQUAC model fits a binary system with only two adjustable parameters, along with pure component data. The model requires three pure-component molecular-structure constants (r, q, q') that depend on molecular size and external surface areas ($q = q'$ for fluids other than water or lower alcohols). The UNIQUAC model provides a satisfactory description for many nonelectrolyte mixtures containing polar or nonpolar fluids and water, for either completely or partially miscible systems (compared to the Wilson equation that only works for miscible mixtures).[92] Peres and Macedo[95] demonstrated good prediction of vapor–liquid and solid–liquid equilibrium data of ternary and quaternary highly nonideal mixtures of sugars (D-glucose, D-fructose, and sucrose) in water, using the modified UNIQUAC model (with linear temperature dependence parameters). For each constituent binary mixture, their model has four interaction parameters obtained from fitting to binary experimental data.[95]

Group contribution models are another category of theoretical models that evaluate properties of complex molecules based on the functional groups in the molecules. The functionality of each group is considered to be independent of the molecule in which it appears. Group–group interaction parameters are obtained from experimental data of binary systems. The most famous group contribution methods are: the ASOG (analytical solution of groups) model which is based on the Wilson model, and the UNIFAC (universal functional activity coefficient) model which is based on the UNIQUAC equation. Examples of vapor–liquid equilibrium prediction with the ASOG and UNIFAC models are available in literature.[96,97] For liquid–liquid equilibrium, UNIFAC correlations have been proposed, albeit with less accuracy than for vapor–liquid equilibrium.[92,94] Gmehling *et al.*[98] successfully predicted solid–liquid equilibrium data by the UNIFAC method, including solubility of solid in single and mixed solvents for nonelectrolyte systems, and eutectic temperature and composition of some binary systems. There are other activity coefficient models based on

solution theories such as the Debye–Huckel model for electrolyte solutions, and the Flory–Huggins extension of lattice theory for polymer solutions.[92]

(c) Equations of state for condensed phases: Fugacity coefficients (that can be translated into activity coefficients) can be obtained from pressure–volume–temperature (PVT) behavior of a mixture. The PVT behavior is modeled by equations of state, along with some mixing rules and combining rules to account for interaction of different components. The advantage of using equations of state (over solution theory models) is that the equations of state can predict activity coefficients over a wider range of temperature and pressure including at supercritical conditions. However, the problem is in developing appropriate mixing rules.[99] Different types of equations of state have been used to model activity coefficients based on type of mixtures, such as the Soave–Redlich–Kwong equation and the Peng–Robinson equation for vapor–liquid equilibrium of petrochemical mixtures,[100] and the osmotic virial equations of state for aqueous mixtures.[34–36,101–106]

Among the above-mentioned three types of activity coefficient models, the goal of this study is to compare the general polynomial form of the osmotic virial equation of state, and the empirical Margules model for obtaining activity coefficients. These models are of interest for their similar polynomial forms, mathematical simplicity, ability to describe nonideal solutions and applicability to solid–liquid equilibrium of aqueous solutions. Each of these models has coefficients/parameters that can be obtained from fitting to some equilibrium data. The osmotic virial equation is of great interest for its ability to empirically model a very wide range of aqueous solutions and as such is one of the most widely used solution models in biology. Until recently the use of the osmotic virial equation for solid–liquid equilibrium had not been explored. The osmotic virial equation has been fitted to solid–liquid equilibrium data of binary aqueous solutions in equilibrium with ice in the field of cryobiology by Elliott and co-workers.[34–36] However as the coefficients in that work were based on fitting to data only in the ice-formation region, the coefficients do not describe accurately solutions with higher

concentrations in equilibrium with solid solute precipitate. In the following section we explain both the osmotic virial equation and the Margules equation in detail. Next the governing equations for solid–liquid equilibrium, and the procedure for curve fitting to data are explained. Importantly we present a new method for fitting the osmotic virial equation to binary solid–liquid equilibrium data over the entire range of composition. Then the osmotic virial equation truncated to the first or second virial coefficient is applied to the solid–liquid equilibrium of the water/solute system. The osmotic virial equation fits are then compared to fits with the one- or two-parameter Margules model for five water/solute systems: water/glycerol, water/acetic acid, water/propanoic acid, water/mono-ethylene glycol and water/sulfonale. For reasons that will be presented here, the Margules model may be as equally simple and widely applicable as the osmotic virial equation, but may be preferred in some cases.

4.3. Osmotic viral equation versus Margules equation

4.3.1. Osmotic virial equation:

An advantage of the osmotic virial equation is that successful mixing rules have been proposed based on first principles.[34,35] McMillan and Mayer[101] developed a statistical mechanical expression for the natural logarithm of activity of solvent, $a_{solvent}$ (which is equal to $x_{solvent}\gamma_{solvent}$), in nonelectrolyte systems, in the form of a power series in molar concentration of solutes. Later Hill[102,103] developed analogous expansions in terms of molality or mole fraction of solutes. Any of these expressions is especially natural for osmotic systems, and they are all referred to as the osmotic viral equation (OVE).[102] In practice, the OVE is used in a truncated form of equation (74)[34] to express activity of solvent (component (1)), in terms of mole fraction of solute in a multicomponent system.

$$\ln(a_1) = \ln(x_1\gamma_1)$$

$$= -\left(\sum_{i=2} x_i + \sum_{i=2}\sum_{j=2} B^*_{ij}x_i x_j + \sum_{i=2}\sum_{j=2}\sum_{k=2} C^*_{ijk}x_i x_j x_k + \cdots\right) \quad (74)$$

where subscript 1 denotes the solvent, and indices i, j, or k start from 2 and denote solutes. B^*_{ij} and C^*_{ijk} are the second and the third osmotic viral coefficients, accounting for the interactions between dissolved particles of types i, j and k in the solution. The coefficients are not identical if the polynomial is expanded in terms of molality, *etc*. rather than mole fraction.[35] The virial coefficients are functions of temperature and weak functions of pressure.[102] However, when the osmotic virial equation is fit to phase equilibrium data that is a function of temperature, good fits are empirically obtained with constant osmotic virial coefficients.[34–36,105] The polynomial is usually truncated to second order, or third order for highly nonideal solutions (such as those with nondilute macromolecules[27]).

The activity of water (solvent) is expressed in the form of the osmotic viral equation in many articles: For an uncharged ternary aqueous solution of two incompatible polymers (or proteins) in liquid–liquid equilibrium, Edmond and Ogston[104], expressed chemical potential of each of the two solutes as algebraic expressions, which, along with the Gibbs–Duhem equation, resulted in an OVE equivalent equation for activity of water in a ternary system. (With two incompatible polymers, each phase is enriched in one polymer. It is worth mentioning that aqueous polymer–polymer extraction is a promising technique in biomolecule separation).[104] Gaube *et al.*[107] proposed a similar model, which is expressed in terms of concentration (g solute / ml solution), and they criticized Edmond and Ogston[104] for using molality (instead of mole fraction) in the Gibbs–Duhem equation. According to Haynes *et al.,*[108] to predict binary aqueous solution data at higher polymer concentrations, the OVE expansion should also include a third viral coefficient. Cabezas *et al.*[109] outlined a method, based on renormalization group theory, to account for the osmotic viral coefficient

dependence on polymer molecular weight and polydispersity. Other works have extended the application of the OVE to liquid–liquid equilibrium in a ternary polymer–salt aqueous solution; albeit dilute in salt.[110,111] Elliott and her co-workers[34–36] applied truncated (to second or third viral coefficient) OVEs to the data of binary aqueous solutions at equilibrium with ice (solid–liquid equilibrium), and obtained osmotic viral coefficients (B_{ii} and C_{iii} for use with molality, or B^*_{ii} and C^*_{iii} for use with mole fraction) for the various binary aqueous solutions of interest in cryobiology or biology, with solutes such as sodium chloride, potassium chloride, glycerol, propylene glycol, ethylene glycol, ethanol, methanol, mannitol, sucrose, dextrose, trehalose, hemoglobin, dimethyl sulfoxide, bovine serum albumin, ovalbumin,[35] and hydroxyethyl starch.[106]

According to previous works by Elliott and her co-workers,[34–36,105] for binary systems equation (74) reduces to the following equation:

$$\ln(a_1) = \ln(x_1\gamma_1) = -(x_2 + B^*_{22}x_2^2 + C^*_{222}x_2^3 + \cdots) \tag{75}$$

The activity of solute (component 2) in the binary system can then be obtained from activity of solvent and the Gibbs–Duhem equation. For a binary system, where $x_1 = 1 - x_2$, at constant temperature and pressure the Gibbs–Duhem equation can be simplified to the following equation:

$$\frac{\partial \mu_2}{\partial x_2} = -\frac{(1 - x_2)}{x_2}\frac{\partial \mu_1}{\partial x_2} \tag{76}$$

Substituting equation (75) into equation (73) at constant temperature and pressure, substituting that into equation (76), and integrating, the activity of component 2 is given by,[112]

$$\ln(x_2\gamma_2) = \left(\theta_2 + \ln(x_2) + [2B^*_{22} - 1]x_2 - B^*_{22}\,{x_2}^2 + C^*_{222}\left[\frac{3}{2} - x_2\right]{x_2}^2 + \cdots\right) \tag{77}$$

when the activity of component 1 is expressed as in equation (75).

Coefficients B_{22}^{*} and C_{222}^{*} are obtained from fitting to the experimental data (by minimizing the sum of squared errors). θ_2 is a concentration-independent integration constant that arises from integrating the Gibbs–Duhem equation for component 2, and can be obtained from the known properties of pure components by applying the condition for phase equilibrium (equation (72) or its equivalent forms) to the cases of pure components where $x_2 = 0$ or $x_2 = 1$. Therefore the integration constant (θ_2) is not independent of coefficients B_{22}^{*} and C_{222}^{*}, and so on. We will present an equation for obtaining θ_2 for the case of solid–liquid equilibrium in the next section, when we explain the governing equations for solid–liquid equilibrium. When the OVE is used to fit to the equilibrium data, we neglect the temperature and pressure dependence of B_{22}^{*} and C_{222}^{*} over the range of data. Therefore the temperature dependence of θ_2 is also neglected.

When $\ln(x_2)$ is eliminated from both sides of equation (77), a simplified relation is obtained for $\ln(\gamma_2)$ that can be examined at infinite dilution, where x_2 goes to zero, yielding:

$$\ln(\gamma_2^{\infty}) = \theta_2 \tag{78}$$

where γ_2^{∞} is the activity coefficient of component 2 at infinite dilution ($x_2 \to 0$).

4.3.2. Margules equation

According to the general Margules equation, the activity coefficients of the two components of a binary system are:

$$\ln(\gamma_1) = b_1 {x_2}^2 + c_1 {x_2}^3 + \cdots \tag{79}$$

$$\ln(\gamma_2) = b_2 {x_1}^2 + c_2 {x_1}^3 + \cdots \tag{80}$$

where coefficients b_2, c_2, ... are not independent, and are related to b_1, c_1, … through the Gibbs–Duhem equation at constant temperature and pressure. Considering the dependency of the coefficients (through the Gibbs–Duhem equation), and truncating the polynomial to the third-order term results in the two-parameter Margules equation:[92]

$$\ln(\gamma_1) = [A_{12} + 2(A_{21} - A_{12})x_1]{x_2}^2 \quad (81)$$

$$\ln(\gamma_2) = [A_{21} + 2(A_{12} - A_{21})x_2]{x_1}^2 \quad (82)$$

The two-parameter Margules equation is a 3-suffix type of Margules equation, as $\ln(\gamma_i)$ is explained in terms of x_2^3 when simplified. Parameters A_{12} and A_{21} are obtained from fitting.

When the molecules of the two components are similar in size, shape, and chemical nature, A_{12} and A_{21} are (almost) equal, and the model reduces to the one-parameter Margules equation (two-suffix as the polynomials of equations (81) and (82) will be of power 2 with equal A_{12} and A_{21}).[92]

4.3.3. Comparison of osmotic virial and Margules models

The expression of $\ln(x_1\gamma_1)$ in a binary system using the Margules equation is almost equivalent to that using the virial equation (75). To prove that, consider the Taylor series expansion of $\ln(x_1)$:

$$\ln(x_1) = (x_1 - 1) - \frac{(x_1 - 1)^2}{2} + \frac{(x_1 - 1)^3}{3} - \cdots \quad (83)$$

From equations (81) and (83), and the fact that $x_2 = 1 - x_1$ in a binary system, the following equation is obtained:

$$\ln(x_1\gamma_1) = -\left(x_2 + \left(\frac{1}{2} - 2A_{21} + A_{12}\right){x_2}^2 + \left(\frac{1}{3} + 2A_{21} - 2A_{12}\right){x_2}^3 + \cdots\right) \quad (84)$$

Equation (84) is similar to the binary osmotic virial equation (75). With the Margules equation however, only $\ln(\gamma_1)$ is truncated, and $\ln(x_1)$ is explicitly present in the calculations. Prausnitz[92] has also mentioned this analogy in a subtle way: The Margules equation is a specific case (with binary components having almost equal molecular size) of Wohl's equation, where interaction parameters are important. The "physical significance" of interaction parameters "is in a rough way similar to that of virial coefficients".[92]

4.4. Solid–liquid equilibrium governing equations and the fitting procedure to obtain the coefficients for the activity model

In many cases of solid–liquid equilibrium, usually a pure solid phase is formed due to the differences in molecular size and/or molecular structure.[113] At equilibrium conditions, from equality of chemical potentials of component i that is present in both the liquid and the solid phases, according to equation (72), we can get:[94,113]

$$x_i^L \gamma_i^L = \exp\left[\frac{\Delta H_i^{\text{fus}}}{RT_{m,i}}\left(1-\frac{T_{m,i}}{T}\right) + \frac{1}{RT}\left(T\int_{Tm,i}^{T}\frac{\left(C_{P,i}^L - C_{P,i}^S\right)}{T}\mathrm{d}T - \int_{Tm,i}^{T}\left(C_{P,i}^L - C_{P,i}^S\right)\mathrm{d}T\right) - \frac{\left(v_{0,i}^S - v_{0,i}^L\right)}{RT}\left(P_{\text{ref}} - P\right)\right] \quad (85)$$

where component i is the component that is in equilibrium between the solid and liquid phases, T is the equilibrium temperature of the system, and $T_{m,i}$ is the melting point of component i. ΔH_i^{fus} is the enthalpy of fusion of pure component i at the melting point of that component. $C_{P,i}^L - C_{P,i}^S$ is the difference in the heat capacities of component i in the liquid and solid phases at constant pressure. $v_{0,i}^S$ and $v_{0,i}^L$ are the specific molar volumes of pure liquid and solid component i. P is the equilibrium pressure of the system, and P_{ref} is the reference pressure (1 bar). Since the solid–liquid interface radius of curvature is larger than hundreds of nanometers, liquid pressure and solid pressure are equal to each other ($P^L = P^S = P$).

At low to moderate pressure, the pressure difference term contributes little to the calculated solubility, hence it can be neglected.[94,113] The temperature dependence of $C_{P,i}^L - C_{P,i}^S$ can also be neglected. At modest displacement from the melting point, the contribution of the heat-capacity term is minor. Under these conditions, temperature can be expressed

explicitly in terms of composition and activity coefficient of the component that has its solid in equilibrium with the solution:[114]

$$T = \frac{\Delta H_i^{\text{fus}}}{\frac{\Delta H_i^{\text{fus}}}{T_{m,i}} - R\ln(x_i^L \gamma_i^L)} \tag{86}$$

In the case of a binary solution of water (component 1) and solute (component 2), depending on the concentration of the solution the solution may be in equilibrium with ice ($i = 1$ in equation (86)), or in equilibrium with solidified solute ($i = 2$ in equation (86)).

When using the osmotic virial equation, the integration constant (θ_2) in equation (77) can be obtained from the fact that equation (86) is valid over the range of concentration, including when $x_2 = 1$, and the pure liquid solute is in equilibrium with pure solid solute at the melting point of the pure solute, *i.e.*, $T = T_{m,2}$. For equation (86) to give the melting point of component 2, equation (77) should be zero at $x_2 = 1$. Therefore we derived equation (87) for the relationship between θ_2 and the osmotic virial coefficients:

$$\theta_2 = 1 - B_{22}^* - \frac{C_{222}^*}{2} - \cdots \tag{87}$$

With the appropriate equation for the equilibrium condition (equation (86)), the unknown constants in the activity coefficient model of interest can be obtained by fitting the model to the experimental data and minimizing the sum of squared errors.[115] We used MATLAB R2017b (fminsearch command) to find the coefficient/parameter values that minimize the sum of squared errors of the fitted model compared to the experimental data points. We also tried the minimization of the sum of squared errors with the "solver" in Excel, and the results were the same as the results from MATLAB.

The goodness of the fits is judged based on the percent average relative deviation (d_{s}) and percent maximum relative deviation (d_{max}). The lower the percent average relative deviation, the better is the fit.

4.5. Results and discussion of the osmotic virial and Margules equations applied to water/solute solid–liquid equilibrium data

Figure 26 illustrates the Margules and osmotic virial equation fits to experimental solid–liquid equilibrium data of binary mixtures of solvent water (component 1) with solute (component 2) for five different solutes: glycerol,[116] acetic acid,[117] propionic acid (also called propionic acid),[118] mono-ethylene glycol[119] (ethane-1,2 diol) and sulfonale (tetrahydrothiophene 1,1-dioxide).[117,120] For all of these systems, the possibility of instability of a single liquid and the formation of liquid–liquid equilibrium is ruled out based on the experimental data. Any unexpected shape in the graph therefore solely shows a poor fit of the truncated model, and must not be interpreted as physical behavior of the system. The enthalpies of fusion for each component are obtained from the CRC handbook of Chemistry and Physics.[87] It should be noted that Elliott and co-workers[34–36] optimized osmotic virial equation coefficients based on fitting to only the ice-formation region (left liquidus in Figure 26). Such coefficients cannot precisely predict the solute precipitating region (right liquidus). To accurately fit both liquidi, coefficients must be fitted to the available data over the full range of concentration (from $x_2 = 0$ to $x_2 = 1$).[92]

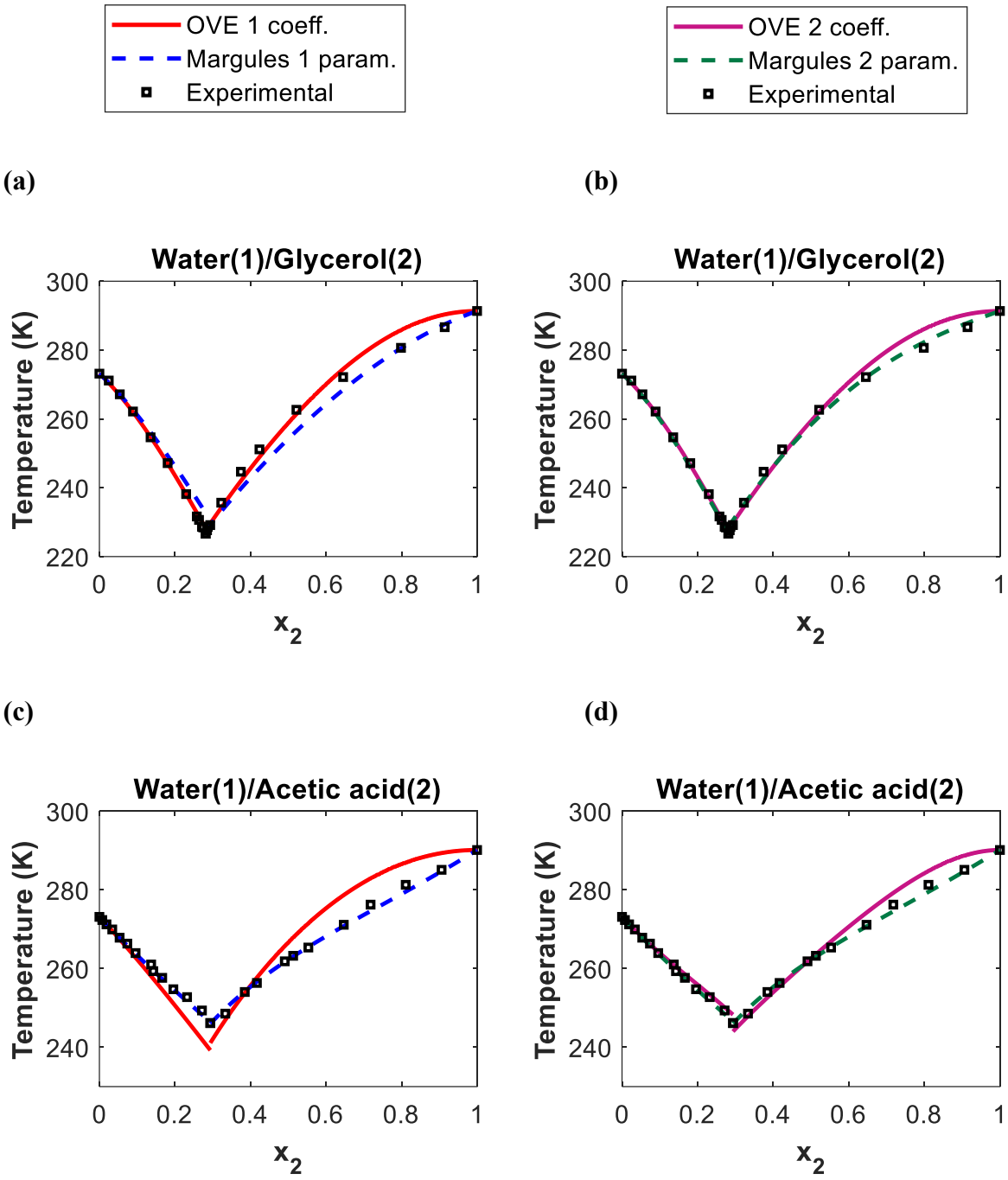
OVE 1 coeff.
Margules 1 param.
Experimental
OVE 2 coeff.
Margules 2 param.
Experimental
(a)
(b)
Water(1)/Glycerol(2)
Water(1)/Glycerol(2)
Temperature (K)
300
280
260
240
220
0
0.2
0.4
0.6
0.8
1
x2
(c)
(d)
Water(1)/Acetic acid(2)
Water(1)/Acetic acid(2)

(e)

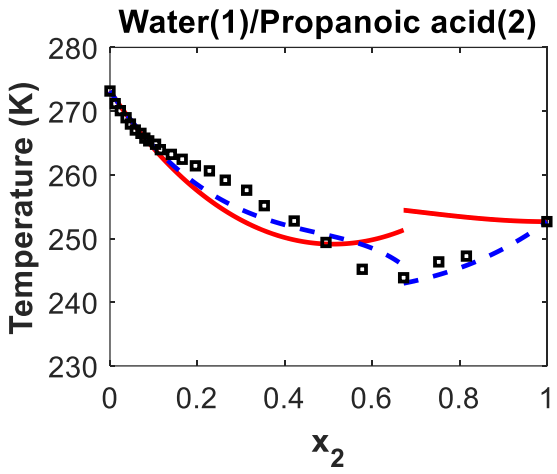
Water(1)/Propanoic acid(2)
Temperature (K)
280
270
260
250
240
230
0
0.2
0.4
0.6
0.8
1
x2

(f)

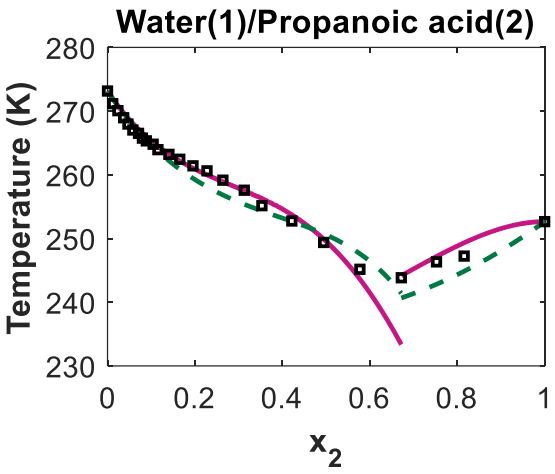
Water(1)/Propanoic acid(2)
Temperature (K)
280
270
260
250
240
230
0
0.2
0.4
0.6
0.8
1
x2

(g)

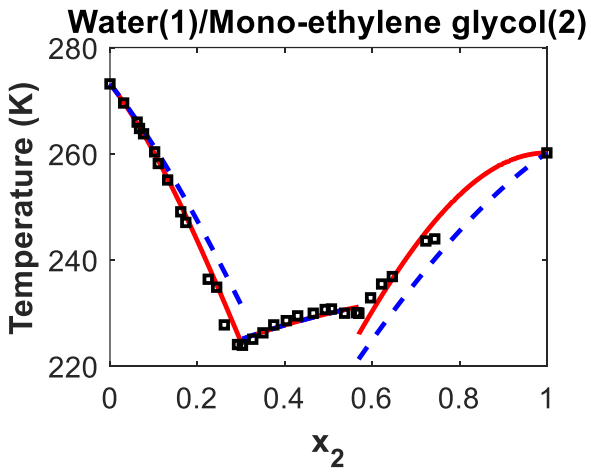
Water(1)/Mono-ethylene glycol(2)
Temperature (K)
280
260
240
220
0
0.2
0.4
0.6
0.8
1
x2

(h)

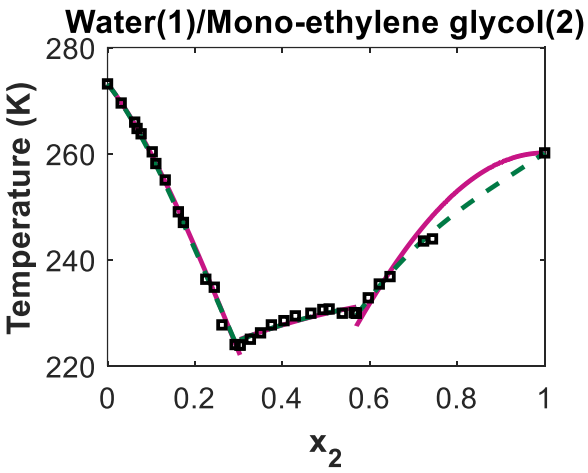
Water(1)/Mono-ethylene glycol(2)
Temperature (K)
280
260
240
220
0
0.2
0.4
0.6
0.8
1
x2

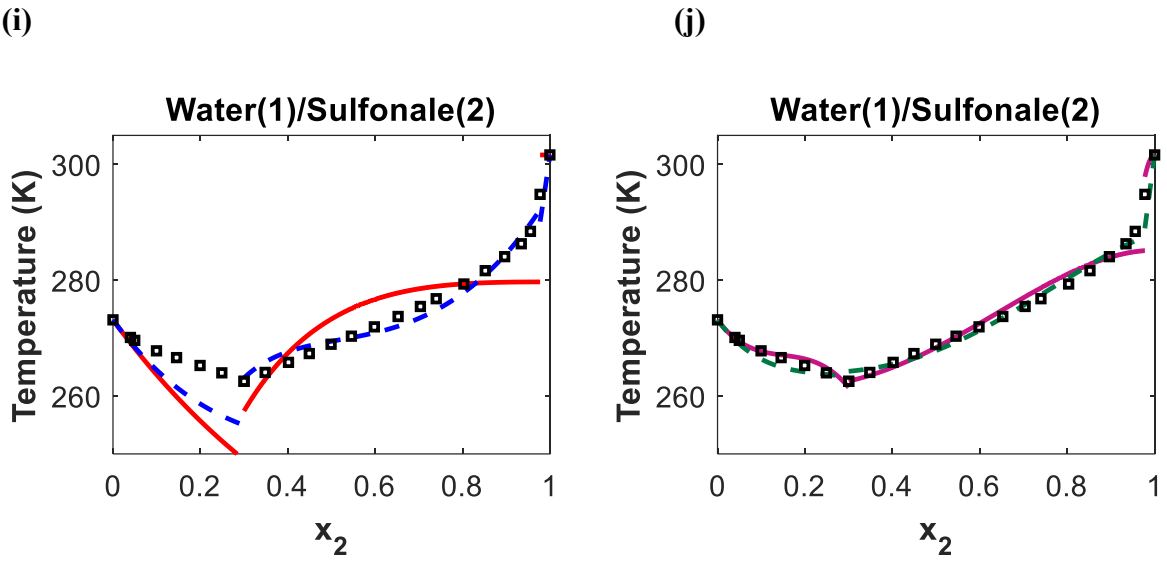

Figure 26. Solid–liquid phase diagram for binary aqueous solutions: water(1)/solute(2) for five different solutes: glycerol,[116] acetic acid,[117] propionic acid,[118] mono-ethylene glycol[119] (ethane-1,2 diol) and sulfonale (tetrahydrothiophene 1,1-dioxide)[117,120] Fits are: the one-parameter Margules equation and osmotic virial equation truncated to the second order term for panels (a),(c), (e), (g), and (i), and the two-parameter Margules equation and the osmotic virial equation truncated to the third order term for panels (b),(d), (f), (h), and (j). The results for the two-parameter Margules equation for the water/glycerol system were previously presented in Liu *et al.*[121]

For the water/propanoic acid system, none of the experimental data points was the eutectic point. For the other systems, the eutectic point was considered once as a point on the left liquidus, and once on the right liquidus.

For water/mono-ethylene glycol the system has two eutectic points, one with solid mono-ethylene glycol at lower temperature, and the other one with hydrated solid at higher temperature. For systems with more than one eutectic point, there are obviously multiple solid phases. A detailed approach would require knowledge of the different solid phases. Here we take an empirical approach that has the benefit of not needing to identify the nature or stoichiometry of the solid phase. For the middle section of the solid–liquid phase diagram of the water/mono-ethylene glycol system, a pseudo enthalpy of fusion ($\Delta H^{\text{fus}}_{\text{pseudo}}$) and a pseudo melting temperature ($T_{m,\text{pseudo}}$) were considered as extra fitting parameters. Hence for the middle section, in equation (86) while i is component 2, $\Delta H^{\text{fus}}_{\text{pseudo}}$ and $T_{m,\text{pseudo}}$, are obtained

from fitting to experimental data, along with coefficients of the model for non-ideality of liquid (OVE or Margules).

For the water/sulfonale system, there is a bend in the graph at 288.6 Kelvin,[117,120] which is considered to be due to a solid–solid transition of the sulfonale. Considering the pseudo enthalpy of fusion ($\Delta H^{\text{fus}}_{\text{pseudo}}$) and pseudo melting temperature ($T_{m,\text{pseudo}}$) as extra fitting parameters for the data points of the middle section (before the transition point), the experimental data can be fit with the two parameter Margules model or the OVE with two coefficients, as presented in Figure 26, panel (h).

Values of the parameters from fitting each model to experimental data and the percent average relative deviation and percent maximum relative deviation for each model are presented in Table 5.

Table 5. Values of the parameters and the percent average relative deviation and percent maximum relative deviation for Margules and osmotic viral equations (mole-fraction based) fitted to the experimental data of the water/solute systems. The best fit for each system is identified by green shading.

Solute and number of experimental data points (n)	Model	% average relative deviation[1] (d_s)	% max relative deviation[2] (d_{max})	Parameters	
Glycerol $n = 24$	Margules, one-param.	1.05	2.65	$A_{12} = A_{21}$	–1.65
	OVE with B_{22}^*	0.47	1.84	B_{22}^*	3.03
	Margules, two-param.	0.36	0.84	A_{12}	–1.09
				A_{21}	–2.16
	OVE with B_{22}^* and C_{222}^*	0.41	1.93	B_{22}^*	3.25
				C_{222}^*	–0.30
Acetic acid $n = 26$	Margules, one-param.	0.17	0.62	$A_{12} = A_{21}$	0.70
	OVE with B_{22}^*	1.21	2.96	B_{22}^*	0.94
	Margules, two-param.	0.17	0.63	A_{12}	0.70
				A_{21}	0.72
	OVE with B_{22}^* and C_{222}^*	0.41	1.27	B_{22}^*	–1.00
				C_{222}^*	2.27
Propanoic acid $n = 25$	Margules, one-param.	0.53	1.58	$A_{12} = A_{21}$	1.81
	OVE with B_{22}^*	1.01	4.35	B_{22}^*	–0.98
	Margules, two-param.	0.48	1.42	A_{12}	1.47
				A_{21}	1.82
	OVE with B_{22}^* and C_{222}^*	0.25	0.84	B_{22}^*	–2.48
				C_{222}^*	2.97

[1] $d_s = 100 \times \frac{1}{n} \sum \frac{|y_a - \hat{y}_a|}{y_a}$

where y_a is the value of the experimental point, $\hat{y}_a$ is the calculated value from the model, and n is number of experimental data points.

[2] $d_{max} = 100 \times \max\left(\frac{|y_a - \hat{y}_a|}{y_a}\right)$

Solute and number of experimental data points (n)	**Model**	**% average relative deviation (d_s)**	**% max relative deviation (d_{max})**	**Parameters**	
Mono-ethylene glycol n = 34	Margules, one-param.	1.31	4.40	$A_{12} = A_{21}$	–1.32
				ΔH^{fus}_{pseudo}	73287
				$T_{m,pseudo}$	236.18
	OVE with B^*_{22}	0.48	1.86	B^*_{22}	3.04
				ΔH^{fus}_{pseudo}	90663
				$T_{m,pseudo}$	234.61
	Margules, two-param.	0.28	1.12	A_{12}	–0.49
				A_{21}	–2.03
				ΔH^{fus}_{pseudo}	77527
				$T_{m,pseudo}$	234.67
	OVE with B^*_{22} and C^*_{222}	0.40	1.78	B^*_{22}	3.51
				C^*_{222}	–0.63
				ΔH^{fus}_{pseudo}	91925
				$T_{m,pseudo}$	234.37

Solute and number of experimental data points (n)	**Model**	**% average relative deviation (d_s)**	**% max relative deviation (d_{max})**	**Parameters**	
Sulfonale $n = 25$	Margules, one-param.	0.81	2.88	$A_{12} = A_{21}$	1.86
				ΔH^{fus}_{pseudo}	5907.5
				$T_{m,pseudo}$	294.82
	OVE with B^*_{22}	1.63	5.15	B^*_{22}	–0.48
				ΔH^{fus}_{pseudo}	7182.7
				$T_{m,pseudo}$	279.7
	Margules, two-param.	0.35	1.99	A_{12}	–0.43
				A_{21}	1.91
				ΔH^{fus}_{pseudo}	25249
				$T_{m,pseudo}$	288.18
	OVE with B^*_{22} and C^*_{222}	0.34	1.22	B^*_{22}	–5.93
				C^*_{222}	13.05
				ΔH^{fus}_{pseudo}	74715
				$T_{m,pseudo}$	285.16

In Table 5, the best fit for each system is highlighted by green. Comparing the results for the five different solution systems considering non-ideality of the solution as presented in Table 5, shows that both the two-parameter Margules model and the OVE with two coefficients give reasonably good fits. In most cases the two-parameter Margules model results in a slightly better fit and we anticipate that to be the result of $\ln(x_i)$ having infinite terms in the Margules model, whereas in the OVE model $\ln(x_i\gamma_i)$ gets truncated after some terms. To obtain the correspondence of the Margules model and the OVE model, a Taylor series expansion of $\ln(x_1)$ about $x_1 = 1$ is made in equation (83). Truncation therefore has the least deviation from the ln expansion when x_1 is close to 1 (hence x_2 is close to 0).

There are two systems, water/acetic acid and water/propanoic acid, where the goodness of the fit for the one-parameter Margules model is very similar to that for the two-parameter Margules model or the OVE with two coefficients. A closer look at the two-parameter Margules model of these two systems (water/acetic acid and water/propanoic acid) shows that they are a special case where A_{12} is almost equal to A_{21}. Hence the one-parameter Margules model only gives a good fit when the parameters of the two-parameter Margules model are almost equal, in which case the two-parameter Margules model can be simplified to the one-parameter Margules model. The OVE with one coefficient fits reasonably well to two of the systems, water/glycerol and water/mono-ethylene glycol, with one less parameter compared to the two-parameter Margules and the OVE with two coefficients. On the other hand, for the water/propanoic acid and water/sulfonale systems, the OVE with one coefficient does not result in a good fit, whereas the OVE with two coefficients gives a reasonably good fit. For the water/sulfonale system, the OVE with two coefficients fits poorly compared to the Margules model with two parameters near the transition point; however, the OVE with two coefficients gives better results at dilute solute concentrations.

For comparison of the two models for nonideality of the solution, OVE and the Margules model, with the ideal model (where $\gamma_i = 1$), in Table 6 the percent average relative deviation and percent maximum relative deviation of the ideal model predictions from the experimental data for each system are presented.

Table 6. Percent average relative deviation and percent maximum relative deviation of ideal solution predictions ($\gamma_i = 1$) from the experimental data for the water/solute systems.

Solution system	**% average relative deviation (d_s)**	**% max relative deviation (d_{max})**
Water / Glycerol	4.28	10.07
Water / Acetic acid	1.65	5.85
Water / Propionic acid	3.40	15.94
Water / Mono-ethylene glycol $\Delta H^{fus}_{pseudo} = 44673$ $T_{m,pseudo} = 236.91$	1.50	7.85
Water / Sulfonale $\Delta H^{fus}_{pseudo} = 28588$ $T_{m,pseudo} = 285.56$	1.47	8.31

The infinite dilution activity coefficients are also calculated based on each model, for different systems of interest, and the results are presented in Table 7.

Table 7. Infinite dilution activity coefficients based on the Margules model and the osmotic virial equation, for different systems of interest.

Solution system	Margules Model		Osmotic virial equation	
	$\gamma_1^\infty = \exp(A_{12})$	$\gamma_2^\infty = \exp(A_{21})$	$\gamma_1^\infty = \exp(-B - C + \frac{1}{2} + \frac{1}{3})$	$\gamma_2^\infty = \exp(1 - B_{22}^* - \frac{C_{222}^*}{2})$
Water (1) / Glycerol (2)	0.34	0.12	0.12	0.12
Water (1) / Acetic acid (2)	2.01	2.05	0.65	2.38
Water (1) / Propionic acid (2)	4.35	6.17	1.41	7.35
Water (1) / Mono-ethylene glycol (2)	0.61	0.13	0.13	0.11
Water (1) / Sulfonale (2)	0.65	6.75	0.002	1.50

The results of the infinite dilution activity coefficients from the two models, the Margules model and the OVE, are less similar for γ_1^∞. The analogy between the two models was explained based on the Taylor series expansion of $\ln(x_1)$ about $x_1 = 1$ in equation (83). Truncation of the polynomial in OVE gives more deviation from the ln expansion when x_1 is farther from 1, such as at infinite dilution of component 1, that is the case for γ_1^∞.

The infinite dilution activity coefficients in Table 7 cannot be directly compared with literature values of infinite dilution activity coefficients from experiments[122–125] or infinite dilution activity coefficients that have been obtained by fitting phase equilibrium data[124,126] at a single temperature. The values of infinite dilution activity coefficients in Table 7 have been obtained from fits to phase equilibrium where temperature and composition vary simultaneously. Therefore, they have a different meaning and are necessarily obtained at a different temperature. Fitting the liquidus is different than fitting compositional phase diagrams at fixed temperature.

4.6. Chapter Conclusion

The osmotic virial equation (OVE) has recently been used to model activity coefficients in areas such as biological aqueous solutions where the solution is in solid–liquid equilibrium with pure solid ice.[34–36] In this paper we explained the general form of the osmotic virial equation for a binary system and compared it with the empirical Margules equation that a has similar polynomial form. To further compare the two activity coefficient models, they were combined with the solid–liquid equilibrium equation to fit experimental water/solute solid–liquid equilibrium data for five water/solute systems: water/glycerol, water/acetic acid, water/propanoic acid, water/mono-ethylene glycol and water/sulfonale. The constant parameters in the activity coefficient models are obtained from best fits with minimum sum of squared errors for the two models of the OVE (truncated to one or two virial coefficients) and the one- or two-parameter Margules equations. Both the OVE and Margules models show good fits to the experimental data for the water/solute systems based on the percent average relative deviation and percent maximum relative deviation. In this work, we show that the integration constant that arises when the solute chemical potential equation is found from the OVE by integrating the Gibbs–Duhem equation is not independently assignable, but rather is related to the osmotic virial coefficients. In doing so we provide a method for fitting the osmotic virial equation to solid–liquid phase equilibrium data across the complete concentration range including both the water freezing liquidus and solute precipitating liquidus.

5. Conclusion

This thesis presents a study of the behavior of certain multiphase multicomponent systems at equilibrium with a Gibbsian composite-system thermodynamic[1] approach. Phases that are involved in each system are considered to be non-pure, for better correspondence with application cases. Three different systems are studied: (i) nanobubbles on flat solid surfaces submerged in a liquid solution in Chapter 2, (ii) nucleation of a bubble starting with a convex or a concave meniscus inside a finite cone submerged in a liquid solution in Chapter 3, and (iii) the comparison of two models for the effect of concentration on chemical potential of the liquid phase: the osmotic virial equation and the Margules model, and their performance in fitting to solid–liquid equilibrium with a flat interface, in Chapter 4. The surface effects exist and are accounted for in the first two systems (Chapters 2 and 3) due to the existence of curved liquid–vapor interfaces.

In Chapter 2, thermodynamic stability of surface nanobubbles on a flat solid exposed to a two-component liquid solution, at constant temperature and liquid pressure is examined. Surface nanobubbles are shaped as a spherical cap with height up to tens of nanometers and an anomalously high contact angle. It is assumed that each surface nanobubble is not in diffusive contact with the gas phase outside the system (above the liquid phase) or with other nanobubbles on the time scale of the experiments. Both the liquid and vapor phases are considered to be binary. The changes in the properties of the bulk liquid phase are taken into account over the growth path of the surface nanobubble. Conditions for equilibrium, as well as the free energy of this system are presented. Similarly to previous work on different multiphase systems,[18,21,71–73] the free energy of the system is not any of the common free energies such as Gibbs free energy; it is rather the combination of the Gibbs free energy of the bulk liquid phase and the Helmholtz free energy of the vapor phase plus the interfaces, and

one other extra term. The analysis shows that stable surface nanobubbles (corresponding to global minima in the free energy curves) can only form from a liquid supersaturated with a dissolved gas, and only with an anomalously high contact angle. From an undersaturated liquid solution, stable bubbles can form only with macroscopic height. As the number of surface bubbles present in the system decreases (or analogously the total available moles per bubble of the two components in the system increases), while the degree of saturation of the initial liquid and other parameters are kept the same, the stable point forms with a lower energy (more stability) and a larger size.

In Chapter 3, the stability of a bubble inside a finite cone submerged in a two-component liquid solution, at constant temperature and liquid pressure is investigated. Depending on the cone apex angle and contact angle (defined by solid–liquid interaction), the bubble may start with a convex, or a concave meniscus inside the cone. The conditions for equilibrium and the appropriate free energy of the system are presented. The free energy of the system is the same as that in Chapter 2, because the phases and components in the system are the same, and only the geometry of the system is different. The stability of the system is fully studied over the growth path of the bubble, as the bubble forms inside, gets pinned, and grows outside the cone. Changes in the concentration of both the liquid and vapor phases as a result of changes in bubble size are considered.

(I) For systems where the bubble starts with a convex meniscus inside the cone, a stable equilibrium can only form when the degree of saturation in the initial liquid is above a certain value, and only after passing an energy barrier. Depending on the parameters of the system, the stable equilibrium state (when it exists) may form inside, pinned, or outside the cone; hence the stable bubble is not necessarily pinned to the corner as in the case investigated by Ward *et al.*[18] There are cases for a bubble starting with a convex meniscus where the size of the energy barrier is comparable to the size of the energy well of the stable point, and the energy barrier is small enough, that the system will fluctuate between bubble formation and

disappearance. We call this phenomena "formation–disappearance fluctuation", which causes the density of the relevant section inside the cone to fluctuate between the density of the liquid and the vapor, as mentioned by Elliott and Voitcu.[70] For systems where the bubble starts with a convex meniscus inside the cone, if the fluid phases are pure, then no equilibrium state exists.

(II) For systems where the bubble starts with a concave meniscus inside the cone, there is always at least one equilibrium state, which is a stable state. Even when the system is pure, a stable equilibrium state forms without passing an energy barrier (unstable equilibrium), with a concave meniscus, inside or pinned to the corners. Over the growth path of the bubble, first the radius of curvature of the liquid–vapor interface of a pinned bubble with a concave meniscus increases until the meniscus becomes flat. Then the concavity of the pinned bubble changes to convex by reducing the radius of curvature, in order for the bubble to reach the same contact angle with the solid outside the cone. The growth path for a bubble starting with a concave meniscus is therefore: inside with a concave meniscus, pinned with a concave meniscus, pinned with a convex meniscus, and outside with a convex meniscus. In the case of a system with a bubble starting with a concave meniscus, the system may have one equilibrium state, or three equilibrium states (unstable, metastable, and stable), and the stable point may form inside or pinned with a concave meniscus, or pinned or outside with a convex meniscus. It should be noted that the stable equilibrium bubble is not necessarily inside the cone, even in the case discussed by Jones *et al.*[33]

To present a big picture of the phenomena for the two cases—a bubble starting with a convex or a concave meniscus inside a cone—the effects of different parameters on the stability of each case are studied: The stability of the stable point (if any) increases by increasing the cone mouth radius (w), the contact angle (θ), the total number of moles (n_i), or initial degree of saturation (f_{init}), regardless of whether the bubble starts with a convex or a concave meniscus. The effect of cone apex angle (2β) depends on the shape of the starting

bubble (concave or convex meniscus). A summary of the effects of these parameters on the stability of the system can be found in Table 4. This study adds the missing pieces to the puzzle of bubble formation inside a finite cone from a liquid solution at constant temperature and liquid pressure, along with the effects of different parameters.

In Chapter 4, the polynomial expressions of the osmotic viral equation and the Margules model for a two-component system are compared. Each of these models are then combined with the theoretical equation expressing solid–liquid equilibrium, and fitted to the experimental data for different water/solute systems. The parameters of the two models, the osmotic virial equation (truncated to one or two virial coefficients) and the one- or two-parameter Margules equations, are found based on the best fit with the minimum sum of squared errors. In contrast to previous studies[34–36] where the osmotic virial equation was only fitted to the ice-formation region, here each model is fitted over the entire range of concentration, both the ice-formation liquidus and the solute-precipitating region, with the appropriate equation for each region. For the osmotic virial equation, when deriving the appropriate equation for the chemical potential of the solute, the integration constant that arises from using the Gibbs–Duhem equation along with the osmotic virial equation for the solvent is found to be a dependant parameter, related to the osmotic virial coefficients, and the appropriate equation for that is presented. In comparing the osmotic viral equation and the Margules model in fitting to experimental solid–liquid equilibrium data for water/solute systems, both of the models showed good fits with reasonably low percent average relative deviation and percent maximum relative deviation.

This thesis presents studies of three different multicomponent multiphase systems, with the effect of different relevant parameters on each system. The big picture obtained from this comparative study provides a better understanding of the phenomena, and can help in future optimal design of devices, or better use or control of natural phenomena.

References

(1) Gibbs, J. W. On the Equilibrium of Heterogeneous Substances. *Trans. Conn. Acad. 2* **1878**, 343−524.

(2) Lohse, D.; Zhang, X. Surface Nanobubbles and Nanodroplets. *Rev. Mod. Phys.* **2015**, *87* (3), 981–1035.

(3) Faghihnejad, A.; Zeng, H. Interaction Mechanism between Hydrophobic and Hydrophilic Surfaces: Using Polystyrene and Mica as a Model System. *Langmuir* **2013**, *29* (40), 12443–12451.

(4) Stöckelhuber, K. W.; Radoev, B.; Wenger, A.; Schulze, H. J. Rupture of Wetting Films Caused by Nanobubbles. *Langmuir* **2004**, *20* (1), 164–168.

(5) Karakashev, S. I.; Nguyen, A. V. Do Liquid Films Rupture Due to the So-Called Hydrophobic Force or Migration of Dissolved Gases? *Langmuir* **2009**, *25* (6), 3363–3368.

(6) Hampton, M. A.; Nguyen, A. V. Accumulation of Dissolved Gases at Hydrophobic Surfaces in Water and Sodium Chloride Solutions: Implications for Coal Flotation. *Miner. Eng.* **2009**, *22* (9–10), 786–792.

(7) Fan, M.; Tao, D.; Honaker, R.; Luo, Z. Nanobubble Generation and Its Application in Froth Flotation (Part I): Nanobubble Generation and Its Effects on Properties of Microbubble and Millimeter Scale Bubble Solutions. *Min. Sci. Technol.* **2010**, *20* (1), 1–19.

(8) Seo, H.; Yoo, M.; Jeon, S. Influence of Nanobubbles on the Adsorption of Nanoparticles. *Langmuir* **2007**, *23* (4), 1623–1625.

(9) Liu, G.; Wu, Z.; Craig, V. S. J. Cleaning of Protein-Coated Surfaces Using Nanobubbles: An Investigation Using a Quartz Crystal Microbalance. *J. Phys. Chem. C*

2008, *112* (43), 16748–16753.

(10) Wang, Y.; Bhushan, B. Boundary Slip and Nanobubble Study in Micro/Nanofluidics Using Atomic Force Microscopy. *Soft Matter* **2010**, *6* (1), 29–66.

(11) Lee, T.; Charrault, E.; Neto, C. Interfacial Slip on Rough, Patterned and Soft Surfaces: A Review of Experiments and Simulations. *Adv. Colloid Interface Sci.* **2014**, *210*, 21–38.

(12) Huang, C.; Jiang, J.; Lu, M.; Sun, L.; Meletis, E. I.; Hao, Y. Capturing Electrochemically Evolved Nanobubbles by Electroless Deposition. A Facile Route to the Synthesis of Hollow Nanoparticles. *Nano Lett.* **2009**, *9* (12), 4297–4301.

(13) Hui, F.; Li, B.; He, P.; Hu, J.; Fang, Y. Electrochemical Fabrication of Nanoporous Polypyrrole Film on HOPG Using Nanobubbles as Templates. *Electrochem. commun.* **2009**, *11* (3), 639–642.

(14) Craig, V. S. J. Very Small Bubbles at Surfaces—the Nanobubble Puzzle. *Soft Matter* **2011**, *7*, 40.

(15) Hampton, M. A.; Nguyen, A. V. Nanobubbles and the Nanobubble Bridging Capillary Force. *Adv. Colloid Interface Sci.* **2010**, *154* (1–2), 30–55.

(16) Seddon, J. R. T.; Lohse, D. Nanobubbles and Micropancakes: Gaseous Domains on Immersed Substrates. *J. Phys. Condens. Matter* **2011**, *23* (13), 133001.

(17) Wasai, K.; Kaptay, G.; Mukai, K.; Shinozaki, N. Modified Classical Homogeneous Nucleation Theory and a New Minimum in Free Energy Change. *Fluid Phase Equilib.* **2007**, *254* (1–2), 67–74.

(18) Ward, C. A.; Tikuisis, P.; Venter, R. D. Stability of Bubbles in a Closed Volume of Liquid-Gas Solution. *J. Appl. Phys.* **1982**, *53* (9), 6076–6084.

(19) Colaço, R.; Serro, A. P.; Saramago, B. On the Stability of Bubbles Trapped at a Solid–liquid Interface: A Thermodynamical Approach. *Surf. Sci.* **2009**, *603* (18), 2870–2873.

(20) Yarom, M.; Marmur, A. Stabilization of Boiling Nuclei by Insoluble Gas: Can a

Nanobubble Cloud Exist? *Langmuir* **2015**, *31* (28), 7792–7798.

(21) Ward, C. A.; Levart, E. Conditions for Stability of Bubble Nuclei in Solid Surfaces Contacting a Liquid-Gas Solution. *J. Appl. Phys.* **1984**, *56* (2), 491–500.

(22) McHale, G.; Shirtcliffe, N. J.; Evans, C. R.; Newton, M. I. Terminal Velocity and Drag Reduction Measurements on Superhydrophobic Spheres. *Cit. Appl. Phys. Lett* **2009**, *94* (064104).

(23) Lee, C.; Kim, C. J. Underwater Restoration and Retention of Gases on Superhydrophobic Surfaces for Drag Reduction. *Phys. Rev. Lett.* **2011**, *106* (1).

(24) Patankar, N. A. Supernucleating Surfaces for Nucleate Boiling and Dropwise Condensation Heat Transfer. *Soft Matter* **2010**, *6* (8), 1613.

(25) Betz, A. R.; Jenkins, J.; Kim, C.-J.; Attinger, D. Boiling Heat Transfer on Superhydrophilic, Superhydrophobic, and Superbiphilic Surfaces. *Int. J. Heat Mass Transf.* **2013**, *57*, 733–741.

(26) Scardino, A. J.; Zhang, H.; Cookson, D. J.; Lamb, R. N.; De Nys, R. The Role of Nano-Roughness in Antifouling. *J. Bioadhesion Biofilm Res. J.* **2009**, *ISSN homepage*, 892–7014.

(27) Chen, H.; Mao, H.; Wu, L.; Zhang, J.; Dong, Y.; Wu, Z.; Hu, J. Defouling and Cleaning Using Nanobubbles on Stainless Steel. *Biofouling* **2009**, *25* (4), 353–357.

(28) Ward, C. A.; Forest, T. W. On the Relation between Platelet Adhesion and the Roughness of a Synthetic Biomaterial. *Ann. Biomed. Eng.* **1976**, *4* (2), 184–207.

(29) Ward, C. A.; Johnson, W. R.; Venter, R. D.; Ho, S.; Forest, T. W.; Fraser, W. D. Heterogeneous Bubble Nucleation and Conditions for Growth in a Liquid–gas System of Constant Mass and Volume. *J. Appl. Phys.* **1983**, *54* (4), 1833–1843.

(30) Jones, P. R.; Hao, X.; Cruz-Chu, E. R.; Rykaczewski, K.; Nandy, K.; Schutzius, T. M.; Varanasi, K. K.; Megaridis, C. M.; Walther, J. H.; Koumoutsakos, P.; et al. Sustaining Dry Surfaces under Water. *Nat. Publ. Gr.* **2015**.

(31) Patankar, N. A. Vapor Stabilizing Substrates for Superhydrophobicity and Superslip. *Langmuir* **2010**, *26* (11), 8783–8786.

(32) Vakarelski, I. U.; Patankar, N. A.; Marston, J. O.; Chan, D. Y. C.; Thoroddsen, S. T. Stabilization of Leidenfrost Vapour Layer by Textured Superhydrophobic Surfaces. *Nature* **2012**, *489* (7415), 274–277.

(33) Jones, P. R.; Kirn, A. T.; Ma, Y. D.; Rich, D. T.; Patankar, N. A. The Thermodynamics of Restoring Underwater Superhydrophobicity. *Langmuir* **2017**, *33* (11), 2911–2919.

(34) Elliott, J. A. W.; Prickett, R. C.; Elmoazzen, H. Y.; K. R. Porter, A.; McGann, L. E. A Multisolute Osmotic Virial Equation for Solutions of Interest in Biology. *J. Phys. Chem. B* **2007**, *111* (7), 1775–1785.

(35) Zielinski, M. W.; McGann, L. E.; Nychka, J. A.; Elliott, J. A. W. Comparison of Non-Ideal Solution Theories for Multi-Solute Solutions in Cryobiology and Tabulation of Required Coefficients. *Cryobiology* **2014**, *69* (2), 305–317.

(36) Prickett, R. C.; Elliott, J. A. W.; McGann, L. E. Application of the Multisolute Osmotic Virial Equation to Solutions Containing Electrolytes. *J. Phys. Chem. B* **2011**, *115* (49), 14531–14543.

(37) Lou, S.-T.; Ouyang, Z.-Q.; Zhang, Y.; Li, X.-J.; Hu, J.; Li, M.-Q.; Yang, F.-J. Nanobubbles on Solid Surface Imaged by Atomic Force Microscopy. *J. Vac. Sci. Technol. B Microelectron. Nanom. Struct.* **2000**, *18* (5), 2573.

(38) Zhang, X. H.; Maeda, N.; Craig, V. S. J. Physical Properties of Nanobubbles on Hydrophobic Surfaces in Water and Aqueous Solutions. *Langmuir* **2006**, *22* (11), 5025–5035.

(39) Ljunggren, S.; Eriksson, J. C. The Lifetime of a Colloid-Sized Gas Bubble in Water and the Cause of the Hydrophobic Attraction. *Colloids Surfaces A Physicochem. Eng. Asp.* **1997**, *129–130*, 151–155.

(40) Epstein, P. S.; Plesset, M. S. On the Stability of Gas Bubbles in Liquid-Gas Solutions. *J. Chem. Phys.* **2004**, *18* (11), 1505–1509.

(41) Zhang, X.; Chan, D. Y. C.; Wang, D.; Maeda, N. Stability of Interfacial Nanobubbles. *Langmuir* **2013**, *29* (4), 1017–1023.

(42) Parker ', J. L.; Claesson, P. M.; Attard, P. Bubbles, Cavities, and the Long-Ranged Attraction between Hydrophobic Surfaces. *J. Phys. Chem* **1994**, *98*, 8468–8480.

(43) Ishida, N.; Inoue, T.; Miyahara, M.; Higashitani, K. Nano Bubbles on a Hydrophobic Surface in Water Observed by Tapping-Mode Atomic Force Microscopy. *Langmuir* **2000**, *16* (16), 6377–6380.

(44) Letters, P. R.; Letters, P. R.; Zhang, X. H.; Zhang, X. H.; Khan, A.; Khan, A.; Ducker, W. a; Ducker, W. a. A Nanoscale Gas State. *October* **2007**, *136101* (March), 1–4.

(45) Zhang, X. H.; Quinn, A.; Ducker, W. a. Nanobubbles at the Interface between Water and a Hydrophobic Solid. *Langmuir* **2008**, *24* (9), 4756–4764.

(46) Seddon, J. R. T.; Kooij, E. S.; Poelsema, B.; Zandvliet, H. J. W.; Lohse, D. Surface Bubble Nucleation Stability. *Phys. Rev. Lett.* **2011**, *106* (5), 56101.

(47) Weijs, J. H.; Snoeijer, J. H.; Lohse, D. Formation of Surface Nanobubbles and the Universality of Their Contact Angles: A Molecular Dynamics Approach. *Phys. Rev. Lett.* **2012**, *108* (10), 1–5.

(48) Yang, J.; Duan, J.; Fornasiero, D.; Ralston, J. Very Small Bubble Formation at the Solid−Water Interface. *J. Phys. Chem. B* **2003**, *107* (25), 6139–6147.

(49) Xu, C.; G; Peng, S.; Qiao, G. G.; Gutowski, V.; Lohse, D.; Zhang, X.; Gennes, P. G. de; Hampton, M. A.; Nguyen, A. V.; et al. Nanobubble Formation on a Warmer Substrate. *Soft Matter* **2014**, *10* (39), 7857–7864.

(50) Rangharajan, K. K.; Kwak, K. J.; Conlisk, A. T.; Wu, Y.; Prakash, S. Effect of Surface Modification on Interfacial Nanobubble Morphology and Contact Line Tension. *Soft Matter* **2015**, *11* (26), 5214–5223.

(51) An, H.; Liu, G.; Craig, V. S. J. Wetting of Nanophases: Nanobubbles, Nanodroplets and Micropancakes on Hydrophobic Surfaces. *Adv. Colloid Interface Sci.* **2015**, *222*, 9–

17.

(52) Brenner, M. P.; Lohse, D. Dynamic Equilibrium Mechanism for Surface Nanobubble Stabilization. *Phys. Rev. Lett.* **2008**, *101* (21), 1–4.

(53) Ducker, W. A. Contact Angle and Stability of Interfacial Nanobubbles. *Langmuir* **2009**, *25* (16), 8907–8910.

(54) Das, S.; Snoeijer, J. H.; Lohse, D. Effect of Impurities in Description of Surface Nanobubbles. *Phys. Rev. E* **2010**, *82* (5), 056310.

(55) Zhang, X.; Uddin, M. H.; Yang, H.; Toikka, G.; Ducker, W.; Maeda, N. Effects of Surfactants on the Formation and the Stability of Interfacial Nanobubbles. *Langmuir* **2012**, *28*, 10471–10477.

(56) German, S. R.; Wu, X.; An, H.; Craig, V. S. J.; Mega, T. L.; Zhang, X. Interfacial Nanobubbles Are Leaky: Permeability of the Gas/Water Interface. *ACS Nano* **2014**, *8* (6), 6193–6201.

(57) Borkent, B. M.; de Beer, S.; Mugele, F.; Lohse, D. On the Shape of Surface Nanobubbles. *Langmuir* **2010**, *26* (1), 260–268.

(58) Liu, Y.; Zhang, X. A Unified Mechanism for the Stability of Surface Nanobubbles: Contact Line Pinning and Supersaturation. *J. Chem. Phys.* **2014**, *141* (13), 134702.

(59) Lohse, D.; Zhang, X. Pinning and Gas Oversaturation Imply Stable Single Surface Nanobubbles. *Phys. Rev. E* **2015**, *91* (3), 1–5.

(60) van Limbeek, M. A. J.; Seddon, J. R. T. Surface Nanobubbles as a Function of Gas Type. *Langmuir* **2011**, *27* (14), 8694–8699.

(61) Steitz, R.; Gutberlet, T.; Hauss, T.; Klösgen, B.; Krastev, R.; Schemmel, S.; Simonsen, A. C.; Findenegg, G. H. Nanobubbles and Their Precursor Layer at the Interface of Water Against a Hydrophobic Substrate. *Langmuir* **2003**, *19* (6), 2409–2418.

(62) Lu, Y.-H.; Yang, C.-W.; Hwang, I.-S. Molecular Layer of Gaslike Domains at a Hydrophobic-Water Interface Observed by Frequency-Modulation Atomic Force

Microscopy. *Langmuir* **2012**, *28* (35), 12691–12695.

(63) Peng, H.; Hampton, M. A.; Nguyen, A. V. Nanobubbles Do Not Sit Alone at the Solid-Liquid Interface. *Langmuir* **2013**, *29* (20), 6123–6130.

(64) Jensen, T. R.; Østergaard Jensen, M.; Reitzel, N.; Balashev, K.; Peters, G. H.; Kjaer, K.; Bjørnholm, T. Water in Contact with Extended Hydrophobic Surfaces: Direct Evidence of Weak Dewetting. *Phys. Rev. Lett.* **2003**, *90* (8), 086101.

(65) Pal, S.; Roccatano, D.; Weiss, H.; Keller, H.; Müller-Plathe, F. Molecular Dynamics Simulation of Water near Nanostructured Hydrophobic Surfaces: Interfacial Energies. *Chemphyschem* **2005**, *6* (8), 1641–1649.

(66) Peng, H.; Birkett, G. R.; Nguyen, A. V. Origin of Interfacial Nanoscopic Gaseous Domains and Formation of Dense Gas Layer at Hydrophobic Solid-Water Interface. *Langmuir* **2013**, *29* (49), 15266–15274.

(67) Weijs, J. H.; Seddon, J. R. T.; Lohse, D. Diffusive Shielding Stabilizes Bulk Nanobubble Clusters. *ChemPhysChem* **2012**, *13* (8), 2197–2204.

(68) Seddon, J. R. T.; Zandvliet, H. J. W. Comment on: "On the Stability of Bubbles Trapped at a Solid–liquid Interface: A Thermodynamical Approach." *Surface Science*. 2010, pp 476–477.

(69) Colaço, R.; Serro, A. P.; Saramago, B. Response to "Comment on: On the Stability of Bubbles Trapped at a Solid–liquid Interface: A Thermodynamical Approach" by J. Seddon and H. Zandvliet. *Surface Science*. 2010, pp 478–479.

(70) Elliott, J. A. W.; Voitcu, O. On the Thermodynamic Stability of Liquid Capillary Bridges. *Can. J. Chem. Eng.* **2008**, *85* (5), 692–700.

(71) Eslami, F.; Elliott, J. A. W. Thermodynamic Investigation of the Barrier for Heterogeneous Nucleation on a Fluid Surface in Comparison with a Rigid Surface. *J. Phys. Chem. B* **2011**, *115* (36), 10646–10653.

(72) Zargarzadeh, L.; Elliott, J. A. W. Comparative Surface Thermodynamic Analysis of

New Fluid Phase Formation between a Sphere and a Flat Plate. *Langmuir* **2013**, *29* (11), 3610–3627.

(73) Zargarzadeh, L.; Elliott, J. A. W. Surface Thermodynamic Analysis of Fluid Confined in a Cone and Comparison with the Sphere-Plate and Plate-Plate Geometries. *Langmuir* **2013**, *29* (42), 12950–12958.

(74) Eslami, F.; Elliott, J. A. W. Stability Analysis of Microdrops during Concentrating Processes. *J. Phys. Chem. B* **2014**, *118* (13), 3630–3641.

(75) Eslami, F.; Elliott, J. A. W. Role of Precipitating Solute Curvature on Microdrops and Nanodrops during Concentrating Processes: The Nonideal Ostwald-Freundlich Equation. *J. Phys. Chem. B* **2014**, *118* (50), 14675–14686.

(76) Sander, R. Compilation of Henry's Law Constants (Version 4.0) for Water as Solvent. *Atmos. Chem. Phys.* **2015**, *15* (8), 4399–4981.

(77) Massoudi, R.; King, A. D. Effect of Pressure on the Surface Tension of Water. Adsorption of Low Molecular Weight Gases on Water at 25.Deg. *J. Phys. Chem.* **1974**, *78* (22), 2262–2266.

(78) Koch, B. M. L.; Amirfazli, A.; Elliott, J. A. W. Modeling and Measurement of Contact Angle Hysteresis on Textured High-Contact-Angle Surfaces. *J. Phys. Chem. C* **2014**, *118* (32), 18554–18563.

(79) Koch, B. M. L.; Elliott, J. A. W.; Amirfazli, A. Study of Model Superoleophobic Surfaces Fabricated with a Modified Bosch Etch Method. *Langmuir* **2014**, *30* (46), 14039–14047.

(80) Koch, B. M. L.; Amirfazli, A.; Elliott, J. A. W. Wetting of Rough Surfaces by a Low Surface Tension Liquid. *J. Phys. Chem. C* **2014**, *118* (41), 23777–23782.

(81) Ward, C. A.; Wu, J. Effect of Adsorption on the Surface Tensions of Solid-Fluid Interfaces. *J. Phys. Chem. B* **2007**, *111* (14), 3685–3694.

(82) Wu, C.; Zandavi, S. H.; Ward, C. A. Prediction of the Wetting Condition from the Zeta

Adsorption Isotherm. *Phys. Chem. Chem. Phys.* **2014**, *16* (46), 25564–25572.

(83) Berg, J. K.; Weber, C. M.; Riegler, H. Impact of Negative Line Tension on the Shape of Nanometer-Size Sessile Droplets. *Phys. Rev. Lett.* **2010**, *105* (7), 076103.

(84) Zargarzadeh, L.; Elliott, J. A. W. Thermodynamics of Surface Nanobubbles. *Langmuir* **2016**, *32* (43).

(85) Zargarzadeh, L. Comparative Surface Thermodynamic Analysis of New Fluid Phase Formation in Various Confining Geometries. **2012**.

(86) Callen, H. B. *Thermodynamics and an Introduction to Thermostatistics, 2nd Ed.*; Wiley, 1985.

(87) Rumble, J. R. *CRC Handbook of Chemistry and Physics*, 98th ed.; CRC Press/Taylor & Francis: Boca Raton, FL, 2017.

(88) Maeda, N.; Israelachvili, J. N. Nanoscale Mechanisms of Evaporation, Condensation and Nucleation in Confined Geometries. *J. Phys. Chem. B* **2002**, *106* (14), 3534–3537.

(89) Stroud, W. J.; Curry, J. E.; Cushman, J. H. Capillary Condensation and Snap-off in Nanoscale Contacts. **2000**.

(90) Jang, J.; Schatz, G. C.; Ratner, M. A. Liquid Meniscus Condensation in Dip-Pen Nanolithography. *J. Chem. Phys.* **2002**, *116* (9), 3875–3886.

(91) Maeda, N.; Israelachvili, J. N.; Kohonen, M. M. Evaporation and Instabilities of Microscopic Capillary Bridges. *Proc. Natl. Acad. Sci.* **2003**, *100* (3), 803–808.

(92) Prausnitz, J. M.; Lichtenthaler, R. N.; Azevedo, E. G. d. *Molecular Thermodynamics of Fluid-Phase Equilibria*, 3rd ed.; Pearson Education, 1998.

(93) Sereno, A. .; Hubinger, M. .; Comesaña, J. .; Correa, A. Prediction of Water Activity of Osmotic Solutions. *J. Food Eng.* **2001**, *49* (2), 103–114.

(94) Walas, S. M. *Phase Equilibria in Chemical Engineering*; Butterworth: Boston, 1985.

(95) Peres, A. M.; Macedo, E. A. Thermodynamic Properties of Sugars in Aqueous

Solutions: Correlation and Prediction Using a Modified UNIQUAC Model. *Fluid Phase Equilib.* **1996**, *123* (1–2), 71–95.

(96) Rodríguez, A.; Canosa, J.; Domínguez, A.; Tojo, J. Vapour–liquid Equilibria of Dimethyl Carbonate with Linear Alcohols and Estimation of Interaction Parameters for the UNIFAC and ASOG Method. *Fluid Phase Equilib.* **2002**, *201* (1), 187–201.

(97) Fredenslund, A.; GGmehling, J.; Rasmussen, P. Chapter 6 – Prediction of Vapor-Liquid Equilibria in Binary Systems. In *Vapor-liquid Equilibria Using Unifac*; 1977; pp 86–133.

(98) Gmehling, J. G.; Anderson, T. F.; Prausnitz, J. M. Solid-Liquid Equilibria Using UNIFAC. *Ind. Eng. Chem. Fundam.* **1978**, *17* (4), 269–273.

(99) Wong, D. S. H.; Orbey, H.; Sandler, S. I. Equation of State Mixing Rule for Nonideal Mixtures Using Available Activity Coefficient Model Parameters and That Allows Extrapolation over Large Ranges of Temperature and Pressure. *Ind. Eng. Chem. Res.* **1992**, *31* (8), 2033–2039.

(100) Oliveira, M. B.; Ribeiro, V.; Queimada, A. J.; Coutinho, J. A. P. Modeling Phase Equilibria Relevant to Biodiesel Production: A Comparison of g^E Models, Cubic EoS, EoS− g^E and Association EoS. *Ind. Eng. Chem. Res.* **2011**, *50* (4), 2348–2358.

(101) McMillan, W. G.; Mayer, J. E. The Statistical Thermodynamics of Multicomponent Systems. *J. Chem. Phys.* **1945**, *13* (7), 276–305.

(102) Hill, T. L. Theory of Solutions. *J. Chem. Phys.* **1957**, *26* (4), 955–956.

(103) Hill, T. L. Theory of Solutions. II. Osmotic Pressure Virial Expansion and Light Scattering in Two Component Solutions. *J. Chem. Phys.* **1959**, *30* (1), 93–97.

(104) Edmond, E.; Ogston, A. G. An Approach to the Study of Phase Separation in Ternary Aqueous Systems. *Biochem. J.* **1968**, *109* (4), 569–576.

(105) Zielinski, M. W.; McGann, L. E.; Nychka, J. A.; Elliott, J. A. W. Comment on "Determination of the Quaternary Phase Diagram of the Water–ethylene Glycol–

sucrose–NaCl System and a Comparison between Two Theoretical Methods for Synthetic Phase Diagrams" Cryobiology 61 (2010) 52–57. *Cryobiology* **2015**, *70* (3), 287–292.

(106) Cheng, J.; Gier, M.; Ross-Rodriguez, L. U.; Prasad, V.; Elliott, J. A. W.; Sputtek, A. Osmotic Virial Coefficients of Hydroxyethyl Starch from Aqueous Hydroxyethyl Starch–Sodium Chloride Vapor Pressure Osmometry. *J. Phys. Chem. B* **2013**, *117* (35), 10231–10240.

(107) Gaube, J.; Pfennig, A.; Stumpf, M. Thermodynamics of Aqueous Poly(Ethylene Glycol)-Dextran Two-Phase Systems Using the Consistent Osmotic Virial Equation. *Fluid Phase Equilib.* **1993**, *83*, 365–373.

(108) Haynes, C. A.; Beynon, R. A.; King, R. S.; Blanch, H. W.; Prausnitz, J. M. Thermodynamic Properties of Aqueous Polymer Solutions: Poly(Ethylene Glycol)/Dextran. *J. Phys. Chem.* **1989**, *93* (14), 5612–5617.

(109) Cabezas, H.; Evans, J. D.; Szlag, D. C. A Statistical Mechanical Model of Aqueous Two-Phase Systems. *Fluid Phase Equilib.* **1989**, *53* (C), 453–462.

(110) Haynes, C. A.; Blanch, H. W.; Prausnitz, J. M. Separation of Protein Mixtures by Extraction: Thermodynamic Properties of Aqueous Two-Phase Polymer Systems Containing Salts and Proteins. *Fluid Phase Equilib.* **1989**, *53*, 463–474.

(111) Zafarani-Moattar, M. T.; Sadeghi, R. Liquid–liquid Equilibria of Aqueous Two-Phase Systems Containing Polyethylene Glycol and Sodium Dihydrogen Phosphate or Disodium Hydrogen Phosphate: Experiment and Correlation. *Fluid Phase Equilib.* **2001**, *181* (1), 95–112.

(112) Zielinski, M. W.; McGann, L. E.; Nychka, J. A.; Elliott, J. A. W. Non-Ideal Solute Chemical Potential Equation and the Validity of the Grouped Solute Approach for Intracellular Solution Thermodynamics. *J. Phys. Chem. B* **2017**, *121* (46), 10443–10456.

(113) Seiler, M.; Groß, J.; Bungert, B.; Sadowski, G.; Arlt, W. Modeling of Solid/Fluid Phase

Equilibria in Multicomponent Systems at High Pressure. *Chem. Eng. Technol.* **2001**, *24* (6), 607–612.

(114) Elliott, J. R.; Lira, C. T. *Introductory Chemical Engineering Thermodynamics*; Prentice Hall, 2012.

(115) Draper, N. R.; Smith, H. *Applied Regression Analysis*; Wiley, 1998.

(116) Lane, L. B. Freezing Points of Glycerol and Its Aqueous Solutions. *Ind. Eng. Chem.* **1925**, *17* (9), 924–924.

(117) Solid-Liquid Equilibrium Data of 30 Important Components from Dortmund Data Bank http://www.ddbst.com/en/EED/SLE/SLEindex.php (accessed Dec 5, 2017).

(118) Htira, T.; Cogne, C.; Gagniè, E.; Mangin, D. Determination of the Solid−Liquid Phase Diagram of the Binary System Propionic Acid/Water. *J. Chem. Eng. Data* **2016**, *61* (2), 806–812.

(119) Cordray, D. R.; Kaplan, L. R.; Woyciesjes, P. M.; Kozak, T. F. Solid - Liquid Phase Diagram for Ethylene Glycol + Water. *Fluid Phase Equilib.* **1996**, *117* (1–2), 146–152.

(120) Jens Ahlers; Jürgen Lohmann, A.; Gmehling, J. Binary Solid−Liquid Equilibria of Organic Systems Containing Different Amides and Sulfolane. *J. Chem. Eng. Data* **1999**, *44* (4), 727–730.

(121) Liu, F.; Zargarzadeh, L.; Chung, H.-J. H.-J.; Elliott, J. A. W. J. A. W. Thermodynamic Investigation of the Effect of Interface Curvature on Solid–Liquid Equilibrium, and Eutectic Point of Binary Mixtures. *J. Phys. Chem. B* **2017**, *121* (40), 9452–9462.

(122) Activity Coefficients at Infinite Dilution of 30 Important Components from Dortmund Data Bank http://www.ddbst.com/en/EED/ACT/ACTindex.php (accessed Apr 17, 2018).

(123) Kojima, K.; Zhang, S.; Hiaki, T. Measuring Methods of Infinite Dilution Activity Coefficients and a Database for Systems Including Water. *Fluid Phase Equilib.* **1997**, *131*, 145–179.

(124) Suleiman, D.; Eckert, C. A. Limiting Activity Coefficients of Diols in Water by a Dew Point Technique. *J. Chem. Eng. Data* **1994**, *39*, 692–696.

(125) Rafflenbeul, L.; Hartmann, H. *Eine Methode Zur Auswahl von Lösungsmitteln Für Die Extraktiv-Destillation - Lothar Rafflenbeul - Google Books*; 1979.

(126) Hansen, R. S.; Miller, F. A.; Christian, S. D. Activity Coefficients of Components in the Systems Water–Acetic Acid, Water–Propionic Acid and Water–n-Butyric Acid at 25°. *J. Phys. Chem.* **1955**, *59* (5), 391–395.

6. Appendices

(A-1) Changes in the radius of curvature of the pinned interface as a function of rotation angle for a bubble starting with a convex meniscus inside a finite cone

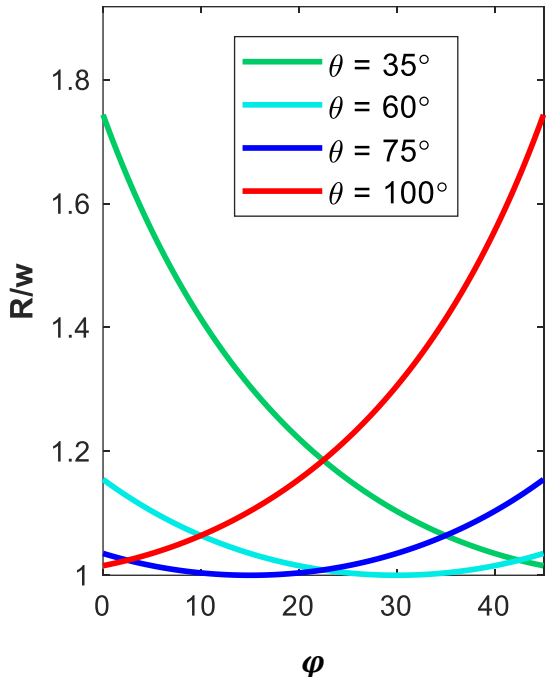

Figure A-1 Changes in the radius of curvature as a function of rotation angle, φ, that happen during pinning for different values of contact angle for a bubble starting with a convex meniscus. The cone half apex angle, β, is considered to be set at 45°. The cone mouth radius, w, is set to be constant. Pinning starts with rotation angle, φ, of $\frac{\pi}{2} - \beta$ with R/w equal to $\sin(\theta + \frac{\pi}{2} - \beta)$, and ends at φ of zero with R/w equal to $\sin(\theta)$.

As presented in Figure A-1, for some sets of β and θ, different rotation angles may lead to the same radius of curvature of the liquid–vapor interface. The graphs are purely geometric relations and no equilibrium equation is involved.

(A-2) Appropriate selection of pinning rotation angle during concavity switch from concave to convex, for a bubble starting with a concave meniscus

There are some cases where the equilibrium state happens while the bubble is pinned and the rotation angle, φ, is close to $\pi - \theta$ where concavity switches from concave to convex, as mentioned in section 3.3.4. At the rotation angle of $\pi - \theta$, the meniscus becomes flat with infinite radius. It is important that the range is chosen such that the rotation angle gets adequately close to $\pi - \theta$ to capture any potential equilibrium state around that point. In Matlab programming, the range for the pinning rotation angle is set as: $\frac{\pi}{2} - \beta \geq \varphi \geq \pi - \theta - \varepsilon$ for states pinned with a concave meniscus, and $\pi - \theta + \varepsilon \geq \varphi \geq 0$ for states pinned with a convex meniscus, with adequately small values of ε. An example of the results for an inappropriate selection of ε is presented in Figure A-2.

(a)

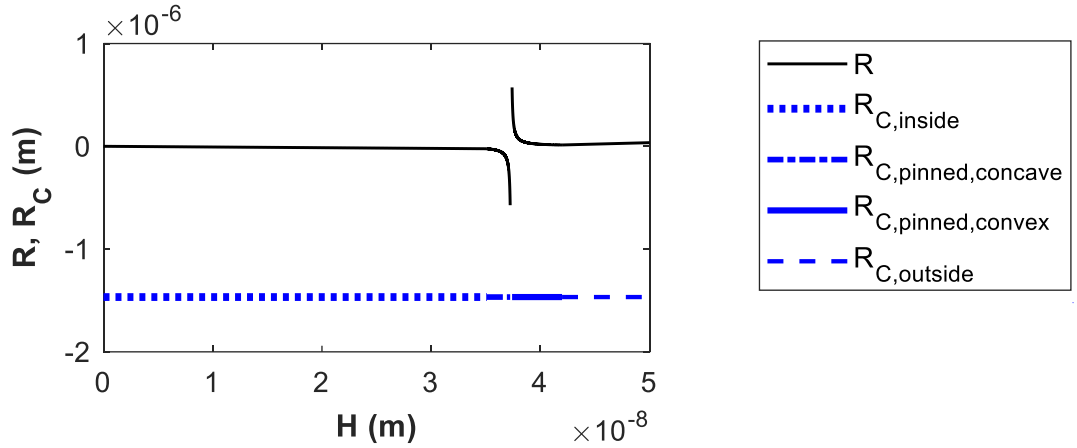

(b)

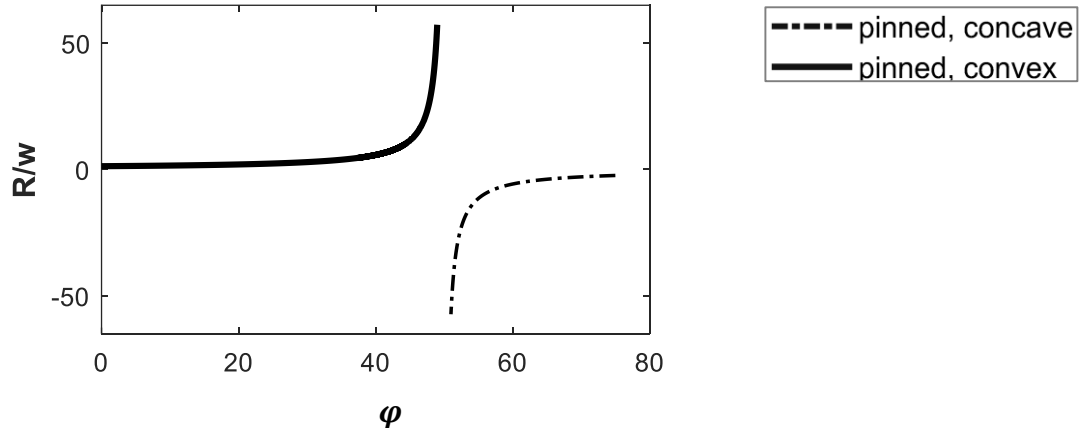

Figure A-2 (a) Geometry radius and the Kelvin radius versus height of the bubble starting with a concave meniscus in a finite cone submerged in a liquid solution with $f_{init} = 0$ (pure) and very small cone mouth radius, w, of 1×10^{-8} m. With $\varepsilon = 1°$, the rotation angle, φ, does not get close enough to $\pi - \theta$ to show the intersection of the geometry radius, R (black solid line) with the equilibrium radius, R_C. The half cone apex angle, β, is 15°, and the contact angle, θ, is considered to be 130°. (b) trend of changes of the ratio of geometry radius to cone mouth width as the rotation angle changes, while the bubble is pinned to the corners. Negative values of R are for the concave case, and positive values are for the convex case. The status of the bubble (inside, or pinned with a concave meniscus or pinned with a convex meniscus to the corner, or outside the cone) is shown with different line types.

Figure A-2 is for the system with $f_{init} = 0$ (hence pure) and the same specifications as for Figure 25, except for a cone mouth radius of 1×10^{-8} m. If ε is set as 1°, the geometry radius R cannot grow big enough to intersect the Kelvin equilibrium radius, because of not getting close enough to rotation angle of $\pi - \theta$, as shown in Figure A-2 (a). Only when ε is set to some samller value such as 0.3° does R grow large enough to reach the intersection point with R_C. In the case of pure liquid, the Kelvin radius is constant over the range of bubble

size (-1.47×10^{-6} m at the temperature and pressure of Figure A-2), and negative, denoting that the equilibrium point occurs when the bubble has a concave meniscus. Figure A-2 (a) has an asymptote at $H = h_{\text{cone}}$, the case where the concave meniscus gets flat before switching to a convex meniscus. Figure A-2 (b) shows the changes in the ratio of the geometry radius to cone mouth radius as the rotation angle changes while the bubble is pinned to the corners. This graph has an asymptote around the rotation angle of $\varphi = \pi - \theta$, where the meniscus switches from concave to convex.

(A-3) Options for plotting the free energy versus size of the vapor phase

As explained in section 3.3.5, free energy is to be plotted versus size of the bubble. The size of the system can be shown by the height from the cone apex to the center of the liquid–vapor interface (H), or the radius of curvature of the liquid–vapor interface (R) or the volume of the vapor (V^V). To better explain why plotting free energy versus height of the liquid–vapor interface was chosen, other options of plotting free energy versus radius of curvature of the liquid–vapor interface or versus volume of the bubble for different cone apex angles are presented here for the cases shown in Figure 13 (a).

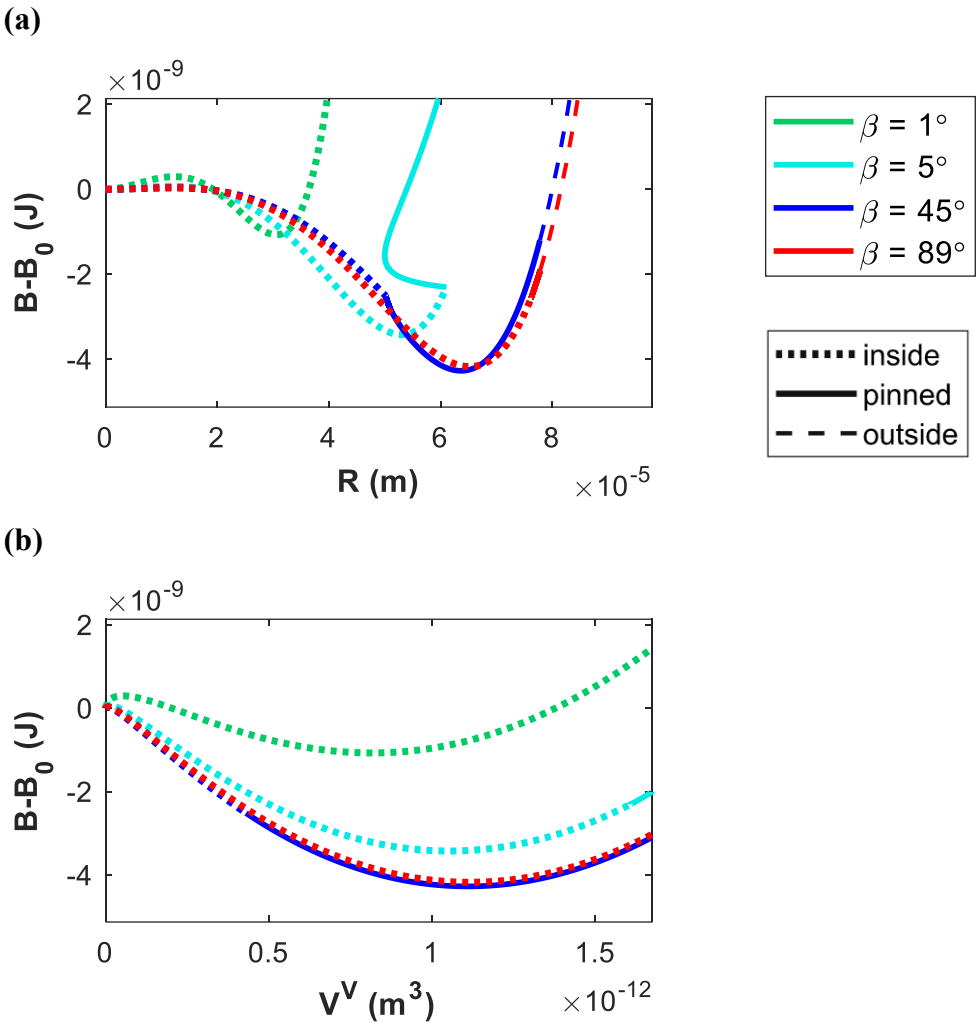

Figure A-3 Plot of free energy (a) versus R and (b) versus V^V for the cases of a bubble starting with a convex meniscus inside a finite cone, investigated in Figure 13 (a) for different half cone apex angles (β). The system is set to be at 25 ℃ and a liquid pressure of 1 atm, with the liquid initially containing 4.15×10^{-5} moles of water and 4.98×10^{-10} moles of nitrogen (initial degree of saturation of 1.089). The cone mouth radius, w, is 50 μm, and the cone contact angle, θ, is 40°. The status of the bubble (inside, pinned to the corner, or outside the cone) is shown with different line types.

As the bubble gets pinned, the radius of the liquid–vapor interface may decrease as explained in Figure A-1, and as happens in Figure A-3 (a) for $\beta = 5°$. Therefore plotting free energy versus R may cause confusion for some cases. Moreover, in case of a bubble starting with a concave meniscus, the sign of the radius of curvature changes as the meniscus changes from concave to convex over the growth path. Therefore, plotting free energy versus radius of curvature, R, is not a convenient option.